



Terbium nanoparticle biofunctionalization for extracellular biosensing

Vjona Çifliku

► To cite this version:

Vjona Çifliku. Terbium nanoparticle biofunctionalization for extracellular biosensing. Inorganic chemistry. Université Paris-Saclay, 2020. English. NNT : 2020UPASS075 . tel-02938737

HAL Id: tel-02938737

<https://theses.hal.science/tel-02938737>

Submitted on 15 Sep 2020

HAL is a multi-disciplinary open access archive for the deposit and dissemination of scientific research documents, whether they are published or not. The documents may come from teaching and research institutions in France or abroad, or from public or private research centers.

L'archive ouverte pluridisciplinaire **HAL**, est destinée au dépôt et à la diffusion de documents scientifiques de niveau recherche, publiés ou non, émanant des établissements d'enseignement et de recherche français ou étrangers, des laboratoires publics ou privés.

Terbium nanoparticle biofunctionalization for extracellular biosensing

Thèse de doctorat de l'université Paris-Saclay

École doctorale n°575:
Electrical, optical, bio: physics and engineering (EOBE)

Spécialité de doctorat: Physique
(Electronique et Optoélectronique, Nano et Microtechnologies)

Unité de recherche : Université Paris-Saclay, CEA, CNRS, Institute for Integrative
Biology of the Cell (I2BC), 91198, Gif-sur-Yvette, France

Référent : Faculté des sciences

Thèse présentée et soutenue à Orsay, le 9 Juin 2020, par

Vjona Çifliku

Composition du Jury

Sandrine LACOMBE

Professeure, Université Paris Saclay

Présidente

Alexandra FRAGOLA

Maîtresse de Conférence, Sorbonne Université

Rapporteur & Examinatrice

Peter REISS

Chercheur, CEA Grenoble

Rapporteur & Examineur

Loïc CHARBONNIÈRE

Chercheur, CNRS Strasbourg

Examineur

Niko HILDEBRANDT

Professeur, Université Paris Saclay

Directeur de thèse

Titre : Bio fonctionnalisation des nanoparticules de terbium pour la bio détection extracellulaire

Mots clés : Nanoparticules de lanthanides, détection à résolution temporelle, microscopie à luminescence, EGFR, bioconjugaison

Résumé : Les nanoparticules dopées au lanthanide (LnNPs) sont devenues une classe importante de fluorochromes pour la biodétection et la bioimagerie avancées. Cependant, le développement de LnNP brillants, stables et bioconjugués reste un défi important pour leur traduction en applications bioanalytiques fonctionnelles. Ici, nous présentons la détection in situ de la liaison ligand-récepteur sur les cellules a été accompli avec des conjugués TbNP-anticorps (Matuzumab) qui pourraient se lier spécifiquement aux récepteurs transmembranaires du facteur de croissance épidermique (EGFR). Une spécificité et une sensibilité élevées ont été démontrées par l'imagerie temporelle de l'EGFR sur

des lignées cellulaires exprimant fortement (A431) et faiblement (HeLa et Cos7) l'EGFR, alors que les lignées cellulaires non exprimantes (NIH3T3) et les cellules A431 passives de l'EGFR n'ont montré aucun signal. Malgré la taille relativement importante des conjugués TbNP-anticorps, ils ont pu être internalisés par les cellules A431 lors de leur liaison à l'EGFR extracellulaire, qui a montré leur potentiel en tant que marqueurs de luminescence brillants et stables pour la signalisation. Des tests de stabilité des TbNP sur une gamme de valeurs de pH, de tampons différents, dans le temps, et d'effet de sonication sur ces NPs ont été effectués en utilisant la DLS et la ZP.

Title : Terbium nanoparticle biofunctionalization for extracellular biosensing

Keywords : Lanthanide nanoparticles, time-resolved detection, luminescence microscopy, EGFR, bioconjugation

Abstract: Lanthanide-doped nanoparticles (LnNPs) have become an important class of fluorophores for advanced biosensing and bioimaging. However, developing bright, stable, and bioconjugated LnNPs remains an important challenge for their translation into functional bioanalytical applications. Here, we present in-situ detection of ligand-receptor binding on cells, which was accomplished with TbNP-antibody (Matuzumab) conjugates that could specifically bind to transmembrane epidermal growth factor receptors (EGFR). High specificity and sensitivity were shown by time-gated imaging of EGFR on both strongly (A431) and weakly

(HeLa and Cos7) EGFR-expressing cell lines, whereas non-expressing cells did not show any signals. Despite the relatively large size of TbNP-antibody conjugates, they could be internalized by A431 cells upon binding to extracellular EGFR, which showed their potential as bright and stable luminescence markers for intracellular signaling. Stability tests of TbNPs over a range of pH values, different buffers, over time, and sonication effect on these NPs were performed by using dynamic light scattering (DLS) and zeta potential (ZP) measurements.

Acknowledgment

In the first place, I wish to thank a lot from the bottom of heart my supervisor Prof. Dr. Niko Hildebrandt for his fundamental role and support in my doctoral work. I am very grateful for his trust in my abilities to carry on with the project with total freedom! He gave me the opportunity to follow my professional dreams and supported me in every step. I also would like to thank him for the great German beer and Italian coffee.

I thank a lot MCF Alexandra Fragola and Dr. Peter Reiss for being the reviewers of my Ph.D. thesis. I appreciate a lot their time spent reading my thesis.

I also wish to thank our collaborators Loïc Charbonniere, Cyrille Charpentier, Peter Reiss, and Davina Moodelly for their kindness, availability and scientific discussions we had during NEUTRINO's meetings. I wish also to thank the group of Philippe Minard (Modélisation et Ingénieur des protéines) for their support and hospitality in the last couple of months of my thesis.

Many thanks to all former members who I encountered and current members of the NanoBioPhotonics group for their encouragement, moral and professional support. My special thanks to Dr. Thomas Plénat and Dr. Marcelina Cardoso Dos Santos, for their continuous guidance, patience and valuable time devoted to sharing their technical and scientific knowledge with me. I look up to them as I admire them as great people and great scientists. I would like to thank Dr. Shashi Bhuckory, Dr. Xue Qiu and Dr. Akram Yahia-Ammar for taking care of me when I first arrived at the lab.

Special thanks to Mme. Meryem Sennad for her positive attitude towards life, and her friendship! I want to express my gratitude to Misses Jingyue Xu, Mimoza Reçi, and Kleni Mulliri for their unconditional friendships.

I gratefully acknowledge the funding sources of my Ph.D. study, National Research Agency (**ANR**).

Finally yet importantly, I am very much indebted to my family and my partner in crime Thomas Plénat, who supported me in every possible way to see the completion of this work. They are my rock!

Publications and Communications

Publications

1. Ultrabright terbium nanoparticles for FRET biosensing and in-situ imaging of epidermal growth factor receptors. Vjona Cifliku,^{b‡} Cyrille Charpentier,^{a‡} Joan Goetz,^{a,c} Aline Nonat,^a Marcelina Cardoso Dos Santos,^b Laura Francès Soriano,^b Ka-Leung Wong,^c Niko Hildebrandt,^{b,*} and Loïc J. Charbonnière,^{a*} (Chemistry 2020 Jun 5)
2. Single-Nanoparticle cell Barcoding by Tunable FRET from Lanthanides to Quantum Dots. C. Chen, L. Ao, Y.-T. Wu, V. Cifliku, et al., *Angew. Chem. Int. Ed.* **2018**, 57, 13686.

Patent

N. Hildebrandt, L.J Charbonnière, V. Cifliku, M. Cardoso Dos Santos, C. Charpentier, J. Goetz, A. Nonat, K.-L. Wong. Ultrabright luminescent lanthanide nanoparticles comprising terbium, with longer excited states. EP 18305890. **07/2018**.

Oral communications

1. Advanced Courses on Functional Imaging of Nuclear Organization & Signalling (FEBS) at Van Leeuwenhoek Centre for Advanced Microscopy (LCAM) at Amsterdam/Netherlands, Terbium nanoparticle biofunctionalization and characterization for extracellular biosensing **[9-15 June 2019]**

Poster communications

1. 9th International Conference on Nanoscience with Nanocrystals (NaNaX 9) at University of Hamburg/Germany, Terbium nanoparticle biofunctionalization and characterization for extracellular biosensing **[16-20 September 2019]**
2. Centre National de le Recherche School on Functional Microscopy in Biology (MiFoBio) Seignosse/France, Ultrabright Terbium Nanoparticles for Biosensing **[5-12 October 2018]**
3. Journée scientifique du département B3S de l'I2BC at auditorium IMAGIF Campus of Centre National de le Recherche at Gif-sur-Yvette/France Ultrabright Terbium Nanoparticles for Biosensing **[18 December 2017]**

Contents

| | |
|--|-----------|
| 1. Introduction | 1 |
| 2. Background | 6 |
| 2.1 Biomarkers | 6 |
| 2.2 Lanthanides | 12 |
| 2.2.1 Introduction | 12 |
| 2.2.2 Luminescence of lanthanide ions | 14 |
| 2.2.3 Applications of lanthanides | 26 |
| 2.3 Time-Resolved Fluorescence Microscopy | 32 |
| 2.4 The EGFR family of receptor tyrosine kinases..... | 33 |
| 2.4.1 Structure and molecular mechanisms of EGF receptors..... | 33 |
| 3. Stability tests of Terbium Nanoparticles..... | 38 |
| 3.1 Introduction | 38 |
| 3.2 Materials and Methods..... | 40 |
| 3.2.1 Materials..... | 40 |
| 3.2.2 Chemical synthesis of Terbium Nanoparticles | 40 |
| 3.2.3 Sample preparation for zeta potential measurements | 41 |
| 3.2.4 Sample preparation for dynamic light scattering measurements | 42 |
| 3.2.5 Instrumentation in DLS measurements | 42 |
| 3.2.6 Instrumentation in ZP measurements | 43 |
| 3.3 Results and Discussion..... | 45 |
| 3.3.1 Influence of time and media on the size of bare TbNPs | 45 |
| 3.3.2 pH influence on the size of TbNPs in diH ₂ O | 52 |
| 3.3.3 Effect of sonication on bare TbNPs as a function of time..... | 53 |
| 3.4 Conclusion | 55 |
| 4. Terbium nanoparticle biofunctionalization for extracellular biosensing | 57 |
| 4.1 Introduction | 57 |
| 4.2 Materials and methods..... | 59 |
| 4.2.1 Materials..... | 59 |

| | |
|--|------------|
| 4.2.2 Characterization of bare TbNPs by transmission electron microscopy | 60 |
| 4.2.3 Labeling of Matuzumab antibody with L ₂ * maleimide ligand..... | 60 |
| 4.2.4 Labeling of L2-Ab conjugate with Terbium Nanoparticles | 61 |
| 4.2.5 Cell Culture | 61 |
| 4.2.6 Cell incubation with TbNP-AB conjugates | 62 |
| 4.2.7 Co-staining TbNP-AB with MeM Bright-640 (MB-640) | 62 |
| 4.2.8 Time-gated PL microscopy | 62 |
| 4.2.9 Z-stacking microscopy | 63 |
| 4.3 Results and Discussion..... | 64 |
| 4.3.1 Characterization of TbNPs | 64 |
| 4.3.2 Fluorescence microscopy imaging of EGFR | 66 |
| 4.4 Conclusion | 83 |
| 5. Summary and Outlook | 84 |
| 5.1 Summary | 84 |
| 5.2 Outlook | 85 |
| References..... | 87 |
| 6. Appendix | 95 |
| 6.1 Abbreviations | 95 |
| 6.2 Principles of Dynamic Light Scattering and Zeta Potential | 98 |
| 6.2.1 Principles of Dynamic Light Scattering (DLS) | 98 |
| 6.2.2 Principles of Zeta Potential (ZP)..... | 99 |
| Synthèse en français..... | 102 |

To my past, present, and future...

1. Introduction

« You never fail until you stop trying »

Albert Einstein

From failures, we rise and every time we rise stronger. Failure is a feeling that is often encountered in scientific research when the first experiment failed, the second one and so on... However, we should never stop trying to find new solutions, new routes to solve the problems. Determination is a feature that should always accompany the human being in order to succeed in their journey and this thesis is a proof of it.

We are living in the *era* of nanoscience and nanotechnology, the scale at which the biological molecules and structures inside living cells operate. By manipulating at the same molecular level in the near future, we will be able to detect faster the biochemical reactions with the appropriate analytical devices thereby improving the specificity of the drug delivery and as well propose a personalized medicine. One of the main reasons that nanoparticles are so attractive for medical applications is their surface/volume ratio that becomes large when size decreases. This peculiarity is leveraged for suitable chemical interactions with biomolecules. To probe inside the infinitely small biological world is necessary of using nano-bio sensors with high specificity and sensitivity. A biosensor is an analytical device that includes a combination of biological detecting elements like a sensor system and a transducer. The transducer, which in our case are the fluorescent nanoparticles, are used to convert the biochemical signal into measurable and quantifiable signal, **Figure 1.1**[1]. Transducers can be optical, thermal, electrochemical, piezoelectric and micromechanical. In my thesis, I used fluorescence-based optical transducers. For medical imaging, the ultimate role of nano-bio sensors is diagnosing disease as early as possible at the single-cell level without any invasive painful procedure and monitoring the therapy effectiveness. One of the leading causes of mortality around the globe is cancer with 9.6 million deaths in 2018. Therefore early

cancer diagnosis is extremely important in order to increase the chances of survival, to provide treatment with fewer side-effects as compared to the harsh treatment of chemotherapy and to have the most suitable treatment for final eradication in the human body[2].

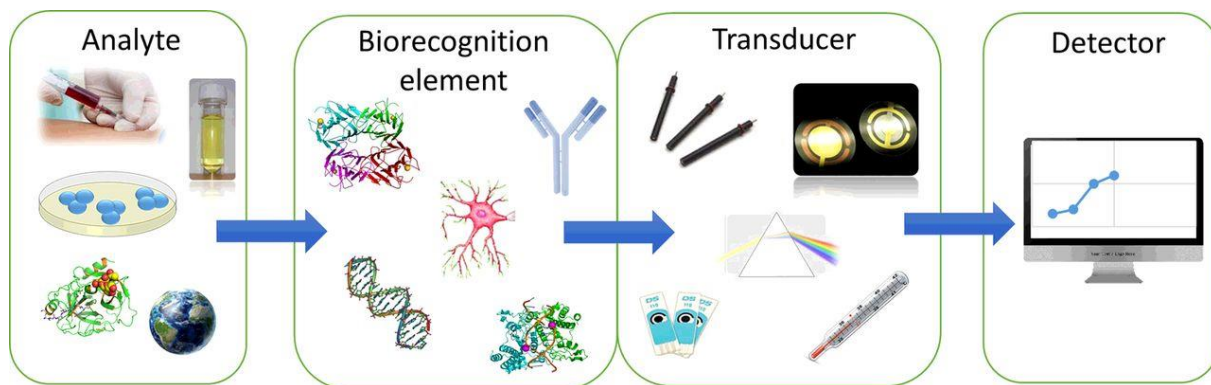


Figure 1.1: Diagram of a biosensor that consists of two components: a bioreceptor and a transducer. (Reproduced from reference Š. Belický et al, Copyright Essays in Biochemistry 2016)

Biomarkers for cancer diagnosis can be found in serum or tissue [3–5]. The emergence of EGFR-targeted (epidermal growth factor receptors) monoclonal antibodies is a milestone in the history of cancer treatment. The combination of immunotherapy with chemotherapy has improved the patient's overall survival. Once the EGFR signaling pathways are activated it will promote tumor growth and progression, including angiogenesis, invasion, metastasis, proliferation, and inhibition of apoptosis. That is why it is of major importance to target and understand better those pathways[6, 7].

This thesis is focused on the detection of EGFR-protein overexpression by using TbNPs on a model human cell line (A431 cells) established from an epidermoid carcinoma in the skin (epidermis)[8]. EGFR is overexpressed in many solid tumors and has been the topic of many investigations in science[9].

The reason for choosing the A431 cell line as a model for our investigation is its uncontrolled overexpression of EGFR[8, 9]. The study presented here used one of the most classical approaches to detect EGFR at the extracellular domain with a monoclonal antibody (mAb). The signal observation was performed by using a time-gated (TG)

imaging microscope that allows for efficient suppression of autofluorescence coming from the endogenous fluorophores that reside within the cells and collect only the emitting photons from our compound, **Figure 1.2**.

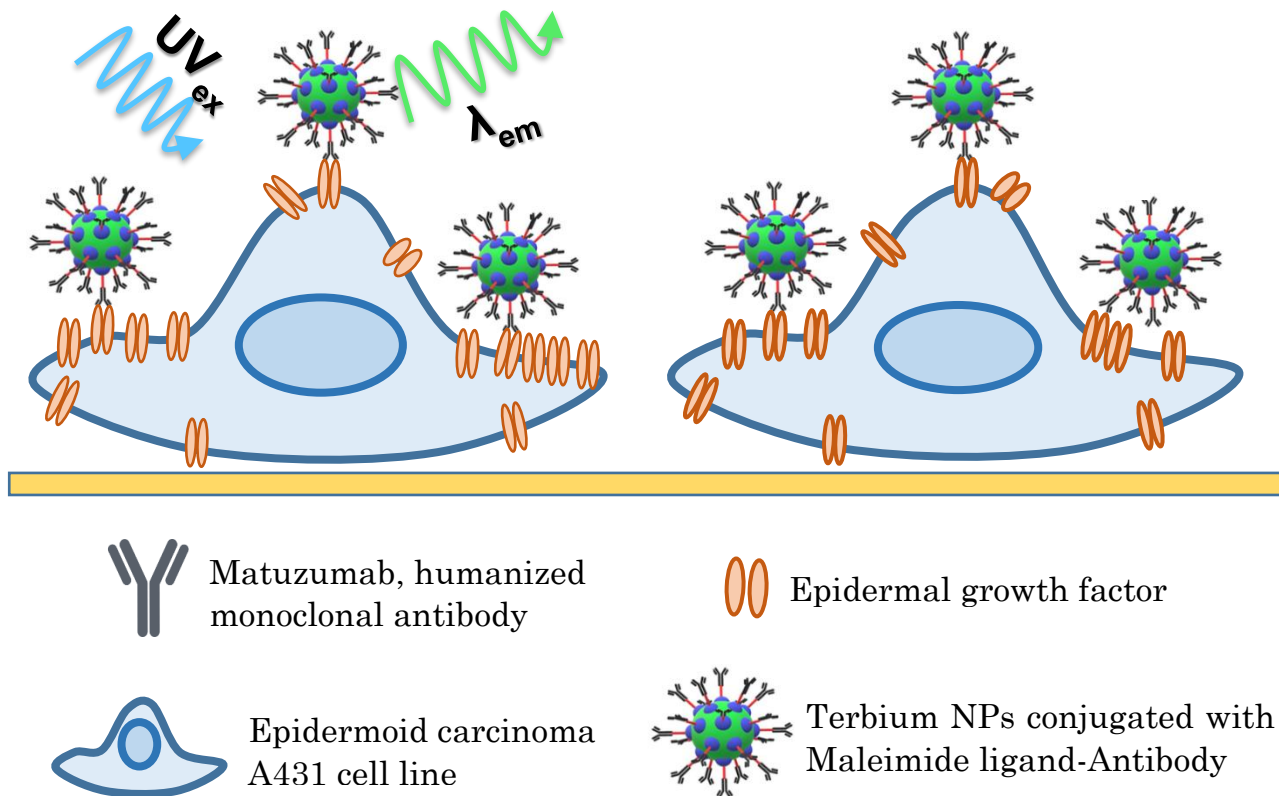


Figure 1.2: Experimental scheme representing immunostaining of epitopes of the EGFR with TbNPs- L_2^ maleimide ligand functionalized with matuzumab antibody on the cell membrane of epidermoid carcinoma A431 cell line.*

The detection is performed based on the luminescence signal of a fluorophore, in this case, terbium nanoparticles (TbNPs). Terbium belongs to the lanthanide (Ln) family, and due to the forbidden intraconfigurational f–f transitions of the central lanthanide ions (common form of Ln^{3+}), the lanthanide complexes provide distinguished photophysical properties, compared to other fluorophores, such as the multiple, characteristic narrow emission bands, and extremely long excited-state lifetimes, which can extend up to several milliseconds[12]. The main drawback of the Ln-based probes is their limited brightness due to the extremely low absorption cross-sections of Ln ions.

This can only partly be overcome by the design of supramolecular Ln-complexes with antenna ligands or the doping of many Ln ions into NPs[13].

To overcome this hurdle our collaborators in Strasbourg (SynPA team) synthesized and characterized two new acid-based ligands hydroxyisophthalates and ultra-bright nanoparticles based on lanthanide ions. The hydroxyisophthalates ligands must have a function that effectively photosensitizes NPs, and possess a spacer connected to an active function. The active function will have the role of reacting with a biological vector, in order to make the NPs target-specific. The covering of the NPs by chromophore ligands allows, thanks to the antenna effect, to reach brightnesses of the order of $10^6 \text{ M}^{-1}\text{cm}^{-1}$ for the $\text{La}_{0.9}\text{Tb}_{0.1}\text{F}_3$ nanoparticles.

In **chapter 3** I present the results obtained from the characterization and stability tests that were performed for the solution of bare TbNPs by dynamic light scattering (DLS) and zeta potential (ZP). We observed the influence of time and different media, followed by the investigation of pH influence as well as we wanted to observe the effect of sonication as a function of time in the most performant buffer.

My main objective is the biofunctionalization and in-situ detection of ligand-receptor binding on cells realized by optimized preparation of TbNP-antibody (Matuzumab) conjugates that could specifically bind to transmembrane EGFR. High specificity and sensitivity are demonstrated by time-gated imaging of EGFR on both overexpressing (A431) and weakly expressing cell lines (HeLa and COS-7). This immunostaining approach serves as a demonstrator for cell membrane biomarker recognition. To demonstrate their specificity, control experiments were performed with antibody saturation (pre-incubation) of the cell membrane in the A431 cell line and using an NIH/3T3 cell line that lacks EGFR, responsible for antibody recognition (**Chapter 4**). A detailed spectroscopic characterization of the Ab-ligand conjugates was performed using stationary ultraviolet/visible (UV/Vis) absorption spectroscopy to estimate the number of antibodies per ligand.

Wide-field photoluminescence (PL) TG imaging was performed using an inverted microscope coupled with a pulsed UV laser for excitation and an intensified charge

coupled device (CCD) camera for time-gated detection[8, 16]. To further localize the TbNP-AB conjugates on the cell envelope the plasma membrane was stained with a dye called MEM-Bright-640 (a kind gift from Dr. Andrey Klymchenko)[15].

These two studies were performed in parallel.

After this introduction, theoretical background on biomarkers, EGFR family, lanthanides, fluorescence microscopy and principles of DLS and ZP will be presented. The experimental studies will follow in a paper-style with an introduction, materials and methods, results and discussion, and a conclusion. A summary addressing the results obtained from the experimental studies will be discussed and an outlook on future research. Bibliography and an appendix follows at the end of the thesis.

2. Background

2.1 Biomarkers

The broad sense of the term ‘biomarker’ includes almost any measurements reflecting an interaction between a biological system and a potential hazard, which may be physical, chemical or biological. The interaction of biological systems with chemicals has been analyzed in tissues and body fluids for chemicals, metabolites of chemicals, enzymes and other biochemical substances. Measurements of these substances are referred to as biomarkers. Biomarkers may be used in hazard identification at the cellular level or at molecular interaction [16]. The National Institutes of Health Biomarkers Definitions Working Group in 1998 have defined the biomarkers or biological markers as “a characteristic that is objectively measured and evaluated as an indicator of normal biological processes, pathogenic processes, or pharmacological responses to a therapeutic intervention”[19, 20]. In order to perform the best accuracy in the assessment of the risk to individuals, the selection of appropriate biomarkers is of critical importance. The role that biomarkers play in predicting the cause of the disease, diagnosis, progression or regression or outcome of disease treatments is very vital. Biomarkers cover this whole spectrum of a disease from its early to the terminal stage, therefore efforts put in creating the best suitable biomarkers for a certain disease are endless. For a better understanding of the biomarkers, they are classified into several categories: I) predisposition, II) diagnostic, III) prognostic and IV) predictive biomarkers. Susceptibility or predisposition biomarkers determine the risk or probability of developing a health disorder based on someone’s genetic family history. Diagnostic biomarkers are used to detect or confirm the presence of a disease or condition of interest. The limitations of a diagnostic biomarker test are related to the clinical sensitivity and specificity of the biomarker. Prognostic biomarkers are used to identify a disease recurrence or progression in patients who have the medical condition of interest, so it will indicate how a health disorder will evolve after primary diagnosis and treatment of the disease. On the other hand, predictive biomarkers are used to identify individuals who are more likely to experience a favorable or unfavorable effect from exposure to a medical product or environmental agent [19]. Examples of

biomarkers include everything from the simplest tests like blood pressure and urine analysis, electrocardiogram, imaging test, to more difficult and slightly risky like biopsy (particularly of neural tissue) to the collection of cerebrospinal fluid [20].

Cancer is one of the lead causes of millions of person's death. Cancer is a pathology characterized by the presence of one (or more) malignant tumor formed from the transformation by mutations or genetic instability (cytogenetic abnormalities) of an initially normal cell. Tumor cell transformation results, in particular, in a loss of control of the cell cycle, an insensitivity to apoptosis, and abnormalities in DNA repair. Cancers are then classified according to the type of cell in which the first transformation occurred (lymphomas, carcinomas, sarcomas); this first malignant cell then having divided, forming the primary tumor made up of clonal cells, **Figure 2.1.1**.

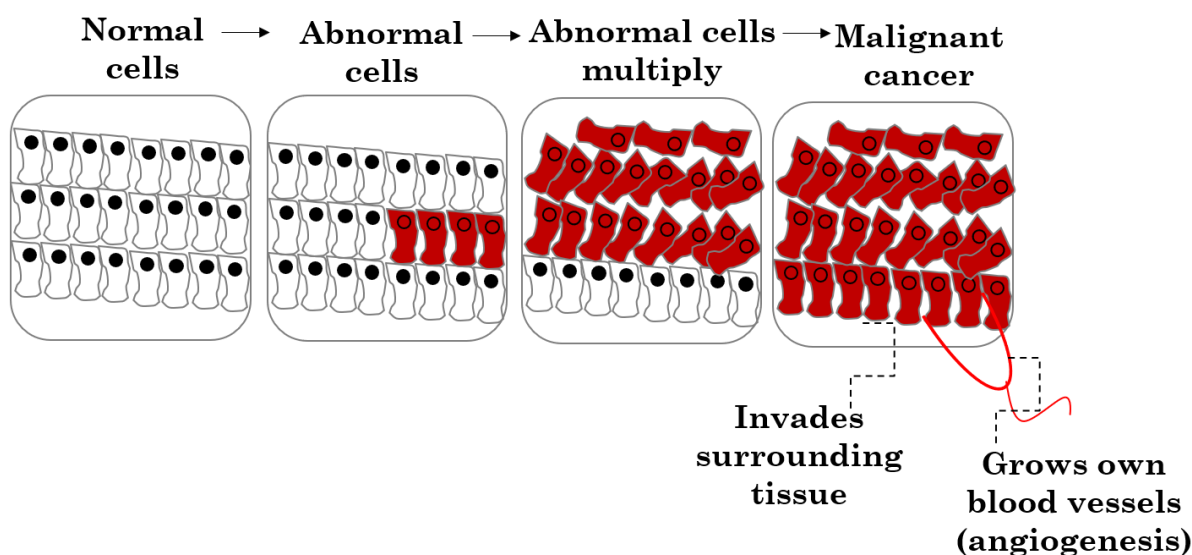


Figure 2.1.1: Representation of malignant cancer propagation. The tumors grow by creating their own blood vessels to get the necessary supply to keep them from surviving and getting bigger. Metastasis occurs when the cancer cells spread through the bloodstream or lymphatic system to other parts of the body-forming tumor somewhere else.

Therefore, early detection of cancer can reduce significantly the rate mortality and will offer a high probability of successful treatment hence endless efforts are made in order to obtain the most sensitive, precise and suitable biomarker. Cancer biomarkers include a large variety of biochemical entities, such as proteins, nucleic acids, micro-RNA,

sugars, small metabolites, enzymes, cytogenetic¹ and cytokinetic² parameters, cell surface receptors as well as tumor cells found in the body fluids. The use of nanoparticles and especially of lanthanide nanoparticles for the detection of cancer biomarkers and cancer cells has rapidly increased since it gives a robust signal amplification and background signal suppression[21]. The potent role that EGFR expression plays in cancer detection has made it one of the most significant predictive biomarkers. The high level of EGFR-protein expression on different cancer cells has been demonstrated to be associated with a high metastatic rate, poor prognosis, and advanced disease progression **Table 2.1.1** [22].

Table 2.1.1

Percentage of different tumor types expressing EGFR

| Tumor type | Levels of EGFR (%) overexpression on tumors |
|---------------------|---|
| Head and Neck | 90-95 |
| Breast | 82-90 |
| Renal carcinoma | 76-89 |
| Cervix/uterus | 90 |
| Esophageal | 43-89 |
| Pancreatic | 30-89 |
| Non-small-cell lung | 40-80 |
| Prostate | 40-80 |
| Colon | 25-77 |
| Ovarian | 35-70 |
| Glioma | 40-63 |
| Bladder | 31-48 |

Antibodies are glycoproteins belonging to the immunoglobulins (Igs), which constitute

¹ The branch of genetics that deals with the cellular components, particularly chromosomes, that are associated with heredity.

² Division of the cytoplasm of a cell following the division of the nucleus.

the humoral branch of the immune system. Igs are produced by B-lymphocytes and form approximately 20% of the plasma proteins in humans. Antibodies are host proteins produced in response to foreign molecules or other agents in the body. The molecular weight of an Ig molecule in monomeric form is approximately 150 kDa. Antibodies exist as one or more copies of a Y-shaped molecule. In higher mammals, exist five classes of immunoglobulins (IgG, IgM, IgA, IgD, and IgE) which differ in size, charge, amino acid composition, and carbohydrate content, **Figure 2.1.2.**

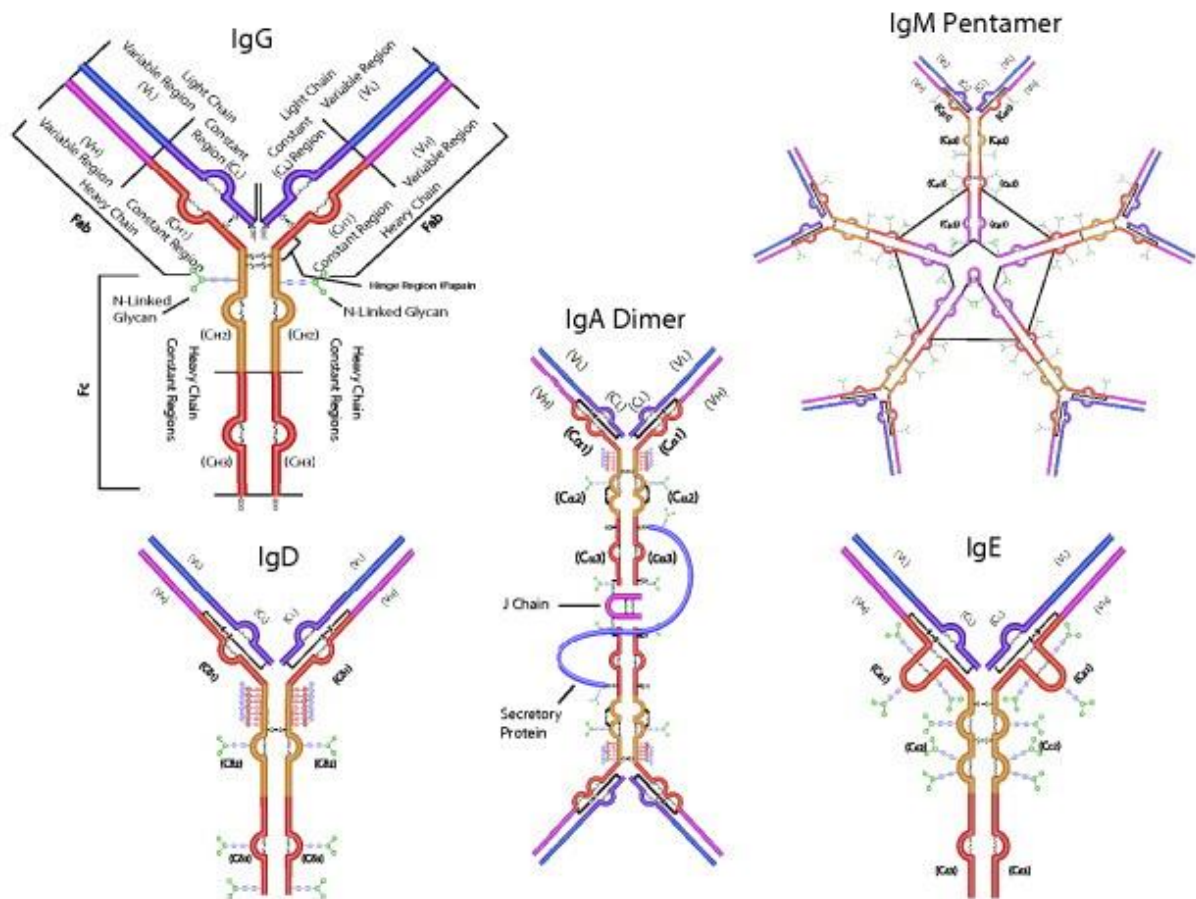


Figure 2.1.2: Structure of the 5 classes of antibodies based on the number of Y units and type of heavy chain [www.sigma-aldrich.com].

Based on the specificity and functionality of a given antibody they can be polyclonal (binding to several sites, epitopes, of a specific antigen) or monoclonal (specifically binding to only one epitope). The common structure of immunoglobulins, independent

of their specificity is composed of four-polypeptide chains: two identical heavy (H) chains, each carrying covalently attached oligosaccharide groups; and two identical, non-glycosylated light (L) chains. The heavy chain and the light chain are joint together by disulphide bonds. These disulphide bonds are located in a flexible region of the heavy chain known as the *hinge* and this region is usually exposed to chemical or enzymatic cleavage. Each globular region formed by the folding of the polypeptide chains because of the disulphide bonding is termed a *domain*. The light chain has two domains namely variable (V_L) and constant (C_L) regions, found at the amino and carboxyl-terminal portions, respectively. The heavy chain is composed of four domains, which consist of one variable (V_H) and three constant (C_{H1} , C_{H2} , and C_{H3}). The Y-shaped unit of the antibody can be divided into three fragments: two identical fragments that contain the antigen-binding activity Fab fragments and an Fc fragment short for fragment crystallizable that contains no antigen-binding activity, **Figure 2.1.3** [23–25].

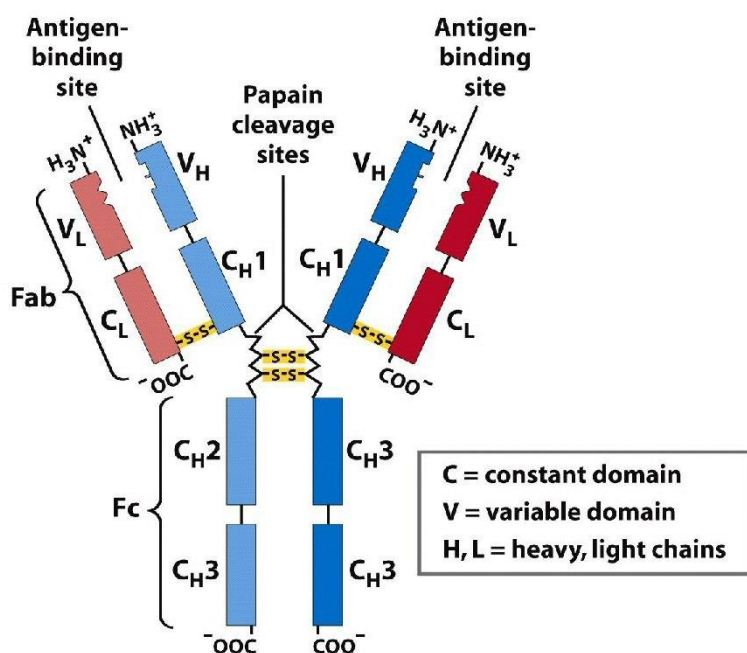


Figure 2.1.3: Human IgG antibody basic structure — the monoclonal IgG antibody (mAb) consists of two identical heavy chains (Hc) and two identical light chains (Lc) subunits. Each heavy chain has four domains (one variable V_H and three constant C_{H1} , C_{H2} , and C_{H3}); each light chain has two domains (one variable V_L , and one constant C_L). Reprinted from Lehninger Principles of Biochemistry, Fifth Edition, Copyright 2008 W.H. Freeman and Company.

In this thesis study, I used the matuzumab antibody to target the EGFR. I must emphasize that EGFR is constitutively expressed in many healthy epithelial tissues, including hair follicles and skin but it is overexpressed or upregulated in a variety of tumor entities. Therefore, EGFR and all other members of this family have been the targets for cancer therapy. Murphy *et al*, in 1987 targeted EGFR with murine mAb 425 generated by immunization of mice. The experiments did not go as predicted since immune reactions were manifested in patients by developing human anti-mouse antibodies³. It was reported that patients were experiencing skin toxicity, including acneiform rash. To overcome the issues of murine or chimeric mAbs the humanization of the murine mAb 425 was carried out. Matuzumab is a humanized recombinant monoclonal antibody of the immunoglobulin G₁ subclass (IgG₁). Kollmannsberger *et al*, in 2006 showed promising activity of humanized mAb matuzumab in-phase I study in the treatment of different tumor entities[26]. The advantages of using matuzumab humanized antibody are its prolonged half-life of 6 to 8 days, binds selectively to EGFR, inhibits ligand-mediated activation and does not induce auto-antibodies⁴ that is a problem with chimeric or murine antibodies[26, 27]. Several years later, on February 18, 2008, due to disappointing studies results Takeda and Merck Serono announced the suspension of the development of matuzumab as a drug for cancer treatment[28]. On the other hand, it may be useful for diagnostic purposes, for which we have used in our studies.

³ HAMA response is when the patients react to the mouse antibodies as if they were a foreign substance, and created a new set of antibodies to the mouse antibodies.

⁴ Antibody that reacts with the cells, tissues, or native proteins of the individual in which it is produced. Many autoantibodies are useful biomarkers of disease.

2.2 Lanthanides

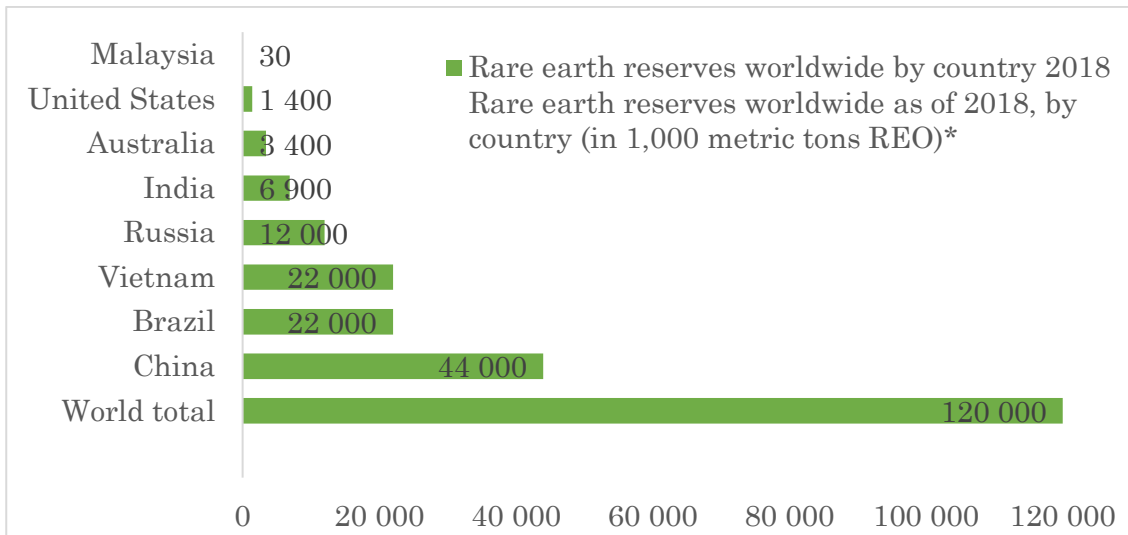
2.2.1 Introduction

Lanthanides (Ln) or 4f-elements are a series of 15-elements from lanthanum (Z=57) to lutetium (Z=71). They are also called “rare earth” elements due to the difficulties in purifying them and this name was given when yttrium (Z=39) and scandium (Z=21) were added as shown in **Figure 2.2.1**[29].

| | | | | | | | | | | | | | | | |
|-------------|--------------------|----|----|----|----|----|----|----|----|----|----|----|----|----|----|
| | <u>Rare Earths</u> | | | | | | | | | | | | | | |
| III B | | | | | | | | | | | | | | | |
| 21 | Sc | | | | | | | | | | | | | | |
| 39 | Y | | | | | | | | | | | | | | |
| Lanthanides | La | Ce | Pr | Nd | Pm | Sm | Eu | Gd | Tb | Dy | Ho | Er | Tm | Yb | Lu |
| | 57 | 58 | 59 | 60 | 61 | 62 | 63 | 64 | 65 | 66 | 67 | 68 | 69 | 70 | 71 |

Figure 2.2.1: Periodic table of the lanthanides series, their atomic numbers, and chemical symbols. (Reprinted from reference [29], Copyright 1983 by D. Reidel Publishing Company right)

Despite this classification, these minerals are quite abundant, being even more abundant than platinum and silver in the earth’s crust. One of the 30 most abundant elements is yttrium together with thulium and lutetium, 100 times more abundant than gold in the earth’s crust. The U.S. Geological Survey estimated that the worldwide reserves of rare earth are approximately 120 million metric tons. According to these estimates, most of these reserves are located within China (44 million metric tons), with the main production in Inner Mongolia[30]. The graph below is a representation of the countries with the highest production according to the analysis done by Statista 2019.



Source: US Geological survey @ Statista 2019

The discovery of rare earth elements did not follow a regular pattern and did not merge in order of atomic number. The atomic number (Z) is derived from nuclear physics and X-ray spectra with the first experimental evidence showed by Henry Moseley and the atomic weight is determined by mass spectrometry[31]. Rare earth elements were originally discovered in 1787 in a quarry in the village of Ytterby, Sweden, a mineral called Ytterbite after the name of the village. At that time, these minerals were found in small quantities and scientists were facing difficulties in purifying them. A few years later, in 1794 the Finnish chemist Johan Gadolin studied the Ytterbite mineral and found that it contained an oxide (Y_2O_3) that he named yttria. The Swedish chemist Carl Gustaf Mosander discovered terbium in 1843 in Stockholm. For separation and characterization of the other non-radioactive rare earth elements, it needed a little bit more than 100 years of history. This chapter in history was closed when the last element ($Z= 61$), promethium, was synthesized and characterized in 1947, completing the lanthanide series[32].

2.2.2 Luminescence of lanthanide ions

2.2.2.1 Quantum numbers, atomic orbitals, and electronic configuration

A simple explanation from a general point of view on how electrons are arranged in an atom is given and more details about the lanthanide family will follow. The location and energy of every electron in an atom is determined by a set of four quantum numbers that describe different atomic orbitals. An orbital is a region of probability where an electron can be found and there are s, p, d and f orbitals with different shapes. These shapes are not electrons, just regions in space where electrons can be found and each can hold up to two electrons. The more electrons an atom has the more of these orbitals will be needed to accommodate them all. The first quantum number is the principal quantum number n , which can have any positive integer value ($n = 1, 2, 3, \dots$). In the Bohr model, it represents the energy level of the electron. Each orbital will have an n value and the larger the value of n the further away from the nucleus. The next quantum number is the angular momentum quantum number ℓ . ℓ can have any value from zero to $n - 1$ ($\ell = 0, 1, 2, \dots (n - 1)$). For example, if an electron has an n value of three ($n = 3$), it can have a ℓ value either 0, 1, or 2 because 2 is $n - 1$. $\ell = 0, 1, 2, \dots (n - 1)$ and $n = 3 \rightarrow \ell = 0, 1, 2$. The ℓ value describes the shape of the orbital. When ($\ell = 0$) we are describing 's' orbitals which have a spherical shape, there is only one orbital per energy level. When ($\ell = 1$) we are describing 'p' orbitals which are lobes that extend outwards on three axes (xyz). There are three of these orbitals per energy level. When ($\ell = 2$) we are describing 'd' orbitals, there are five of these orbitals per energy level. When ($\ell = 3$) we get 'f' orbitals and there are seven orbitals per energy level. Next, we have the magnetic quantum number m_ℓ ($m_\ell = -\ell \dots \ell$). m_ℓ can have a value from negative ℓ to positive ℓ . So if ($\ell = 2$) $\rightarrow m_\ell = -2, -1, 0, 1, 2$. This quantum number determines how many orbitals there are of a type per energy level and therefore describes a specific orbital amongst a particular set. When ($\ell = 0$) $\rightarrow m_\ell = 0$ and that is why there is only one 's' orbital per energy level. When ($\ell = 1$) $\rightarrow m_\ell = -1, 0, 1$ can have three values. That is why there are three 'p' orbitals per energy level. ($\ell = 2$) $\rightarrow m_\ell = -2, -1, 0, 1, 2$ gives us five values and five 'd' orbitals and ($\ell = 3$) gives us the seven orbitals. The last quantum number is the spin quantum number m_s ($m_s = +1/2$ or $-1/2$). Every electron in an atom has a unique set of quantum numbers, no two electrons in an atom can have precisely the same four

quantum numbers as stated by the Pauli exclusion principle[33]. This is because any orbital can only hold up to two electrons and even the two electrons in the same exact orbital will have opposite spin values ($\uparrow\downarrow$). All electrons in an electronic shell will have the same quantum number n . Electrons with the same n and ℓ number will be located in the sub-shells and therefore they will have $(2\ell + 1)$ orbitals which may contain a maximum of $(4\ell + 2)$ electrons. For instance when $(n = 1 \rightarrow \ell = 0 \rightarrow m_\ell = 0)$, we are describing the 1s orbital, it can accommodate two electrons which will have spins ($m_s = +1/2$ and $-1/2$) respectively. This is the lowest energy orbital so any atom on the periodic table will fill this orbital first. The Aufbau principle tells us the order in which an atom will fill up its orbitals. This is determined by their relative energies. Orbitals that are further away from the nucleus have higher potential energy, so it will be 1s first then 2s, 2p, 3s, 3p and so forth. In this way, we determine the electronic configuration of an atom as depicted in **Figure 2.2.2.1**.

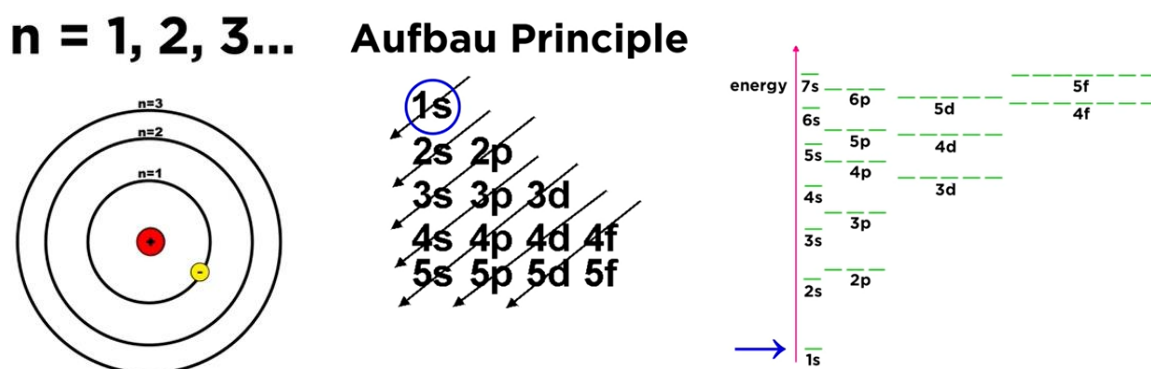


Figure 2.2.2.1: The left side is a representation of the Bohr model, it represents the energy level of the electron and the right side is the representation of the Aufbau principle.

Hund's rule says that for electrons of the same energy you put one electron in each orbital first before doubling them up. So for the electronic configuration of lanthanides, we follow the above-mentioned rules. Since lanthanides have similarities in chemical properties, particularly in the oxidation states it took many years in discovering them, as mentioned in the brief introduction above. This is explained by the electronic configuration in the ground state of the atoms that exist mainly in trivalent state Ln^{III} ($[\text{Xe}]4f^n$, $n = 0-14$) in aqueous solutions[34]. Lanthanides share the electronic

configuration of xenon with 54 electrons ($1s^2 2s^2 2p^6 3s^2 3p^6 4s^2 3d^{10} 4p^6 5s^2 4d^{10} 5p^6$), abbreviated as [Xe] and they are characterized by the progressive filling of 4f orbitals. The large radial expansion of $5s^2 5p^6$ subshells make the valence of 4f orbitals “inner orbitals” and this is crucial to the chemical and spectroscopic properties with parity-forbidden 4f–4f transitions having very low molar extinction coefficients (generally $< 3 \text{ M}^{-1}\text{cm}^{-1}$) and very narrow lines in emission spectra[34]. Coulombic interaction (conventionally called electrostatic force) and the spin-orbit coupling between f-electrons will determine the energy levels of free Ln^{3+} ions in 4f orbitals. The mutual repulsion of the electrons is represented by the Coulombic interaction and will generate the total orbital angular momentum (L) and total spin angular momentum (S), with the spin-orbit coupling defining the total angular momentum (J) of the f-electrons. The specific distribution of electrons within the 4f-shell will be determined from the quantum numbers L, S, and J that define a particular energy level. The electronic levels generated by the $4f^n$ configuration and characterized by the aforementioned quantum numbers S, L and J, can further be split by weak ligand field effects as depicted in **Figure 2.2.2.2** [35].

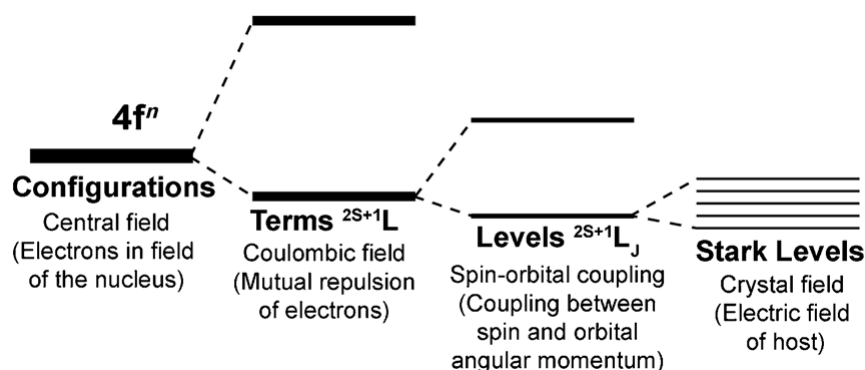


Figure 2.2.2.2: Simplified representation of the effect of Coulombic field, spin-orbit coupling, and crystal field interaction on the $[\text{Xe}]4f^n$ configuration. (Reprinted from reference [35], Copyright 2014 Wiley-VCH Verlag GmbH & Co. KGaA, Weinheim).

The movements of the electrons are coupled and their strength of interaction increases with the atomic number. In order to simplify the treatment of this interaction, Russell-Saunders propose to consider the coupling of the electrons at the level of the overall angular momenta and not for each individual interaction. So according to the Russell-

Saunders notation, we can derive the energy level of the free ions using the term symbols of $(^{2S+1})L_J$, where $2S+1$ represents the total spin multiplicity and $L = 0, 1, 2, 3, 4, 5, 6, 7, 8$ designated in spectroscopy by the letters S, P, D, F, G, H, I, K, L respectively [36]. **Figure 2.2.2.3** represents the ground and excited-state energy levels of the Ln^{3+} ions. The central metal ions (Sm-Dy) have large energy gaps between adjacent levels, between which the radiative transition mainly occurs. The change in spin multiplicity is responsible for the long lifetime of the excited states (microseconds to milliseconds). The metal ions on the periphery (Ce-Pm, Ho-Yb) possess relatively small energy gaps between adjacent levels that give rise mainly to nonradiative transition and make them weakly emissive ions[37].

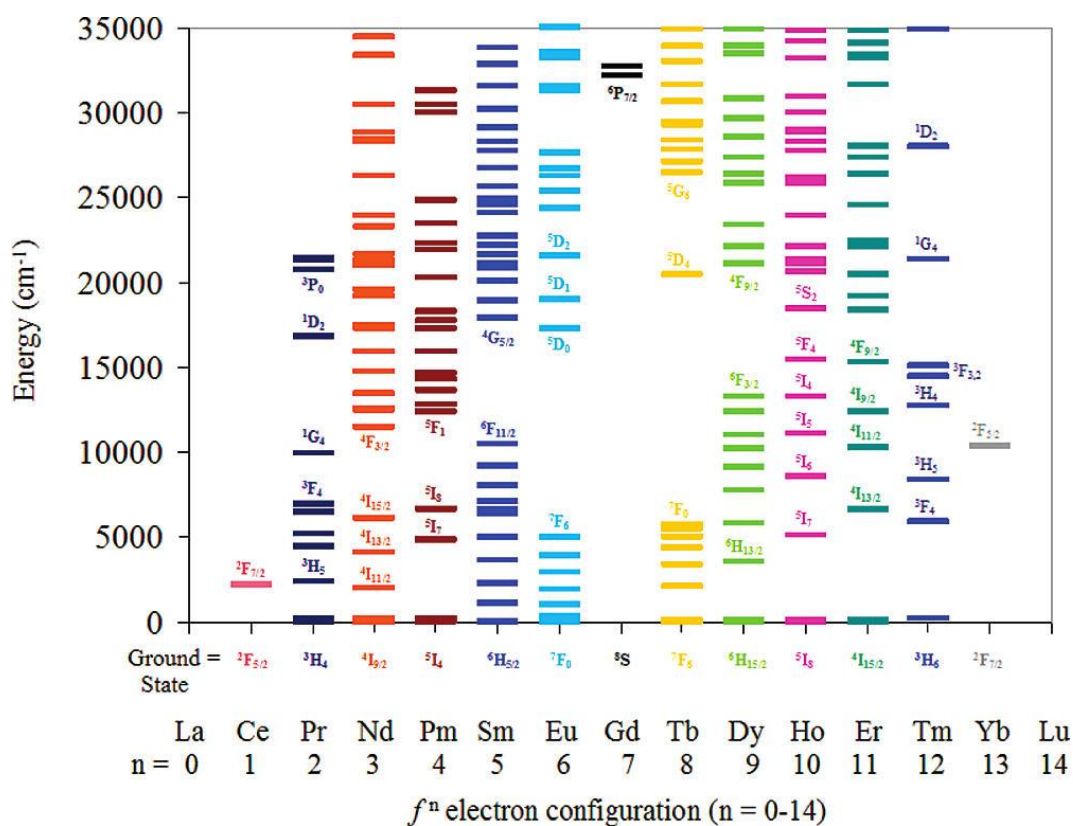


Figure 2.2.2.3: A summary of electronic excited-state energy levels for the Ln (III) series. (Reprinted from reference [9], copyright 2009 American Chemical Society)

The electron transition within $4f^n$ configuration gives rise to the luminescence of the lanthanides. This configuration has enormously complex energy levels owing to the spin-orbit coupling and crystal field interaction. In principle, the f-f transitions are parity-forbidden in a free ion by the parity rule for electronic dipole transitions.

However, transitions within the f-shell are responsible for the crystal spectra. In a crystal or glass, forced luminescence transitions will become allowed by mixing of opposite-parity configurations that can lead to the breakdown of the selection rules where electric dipole transitions are weakly allowed. The probability of the electric dipole transitions is greatly increased when the crystal field is asymmetric. So in order to obtain higher luminescence emission intensity, we could lower symmetry around the lanthanides by tailoring the crystal structure[35, 38, 39]. According to Pearson's classification, lanthanide (III) ions are hard cations and are essentially involved in ionic or ion-dipole bonding with little covalency. The nature of Ln ions with ligands is more electrostatic rather than covalent. The coordination of ligands to a central Ln^{3+} ion will depend on the strength of electrostatic interaction between Ln^{3+} ions and the ligand as well on the steric properties of the ligand. Moreover, according to Pauling's electronegativity, Ln^{3+} ions are highly electropositive with values between 1.10 and 1.27. One of the particularities of rare earth is the fame of being the longest series of elements with remarkable homogeneity of chemical properties. The only parameter significantly varying monotonically along the series is the ionic radius. The ionic radii of Ln (III) ions are large and depend on both the ion and the coordination number. From the beginning to the end of the lanthanides series, the ionic radius decreases steadily while hydration enthalpies increase almost linearly. This phenomenon is called lanthanide contraction and is due to the increase in the nuclear charge. When the 4f valence layer is gradually filled from lanthanum to lutetium, the action of the nuclear charge increases on the charges of the peripheral electrons, thereby leading to a decrease in the ionic radius as presented in **Figure 2.2.2.4**[37].

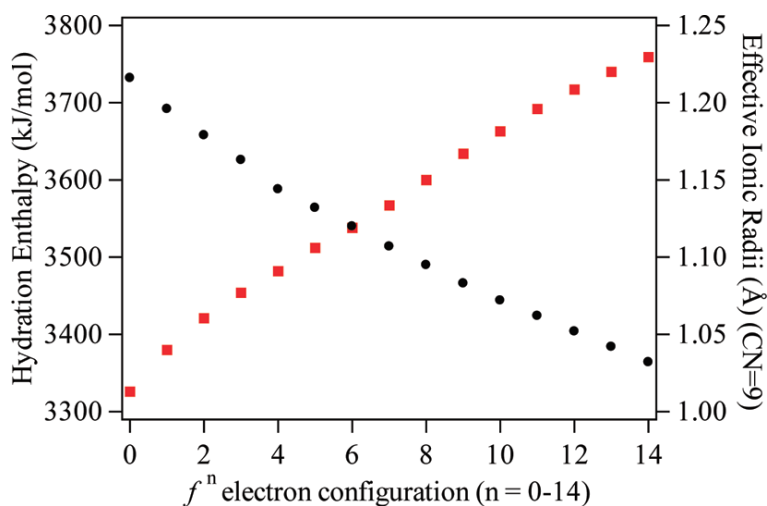


Figure 2.2.2.4: Observed increase in hydration enthalpy (left axis, red squares) and decrease in ionic radii (right axis, black circles) for the trivalent Ln (III) series. (Reprinted from reference[37], Copyright 2009 American Chemical Society)

Hence, is the presence of the 4f-electrons, even in the core, which separates one lanthanide metal from the next lanthanide. We talk mainly of the trivalent state of lanthanide ions because this is the principal state that lanthanides are found in aqueous solutions due to the balance between the sum of the first three ionization energies and hydration enthalpy[37]. In aqueous solution, the coordination number is usually in the range of 8 to 10 depending on their ionic radii[1, 10]. The fluorescence that we observe from terbium ions arises from the electronic transitions between f-orbitals. These f-orbitals are shielded from the solvent by higher filled orbitals. Due to this shielding, the lanthanides will display long decay times and since they have a small extinction coefficient they will have low emission rates. What we call an emission spectrum of a fluorophore is, in fact, a luminescence spectrum. The emission spectrum that we observe for one compound depends on two important characteristics: the chemical structure of the fluorophore and the solvent in which this fluorophore is dissolved[41].

2.2.2.2 Antenna effect on lanthanide complexes

Molar absorption or extinction coefficients (ϵ) of trivalent lanthanide ions are small because of the forbidden f–f transitions that suffer from weak intrinsic luminescence and as a consequence of this, we cannot excite efficiently into the f–f transitions. To overcome this limitation, in 1942, S.I. Weissman discovered that if we “surround” the lanthanide complexes with an organic ligand we would be able to observe the light emission of lanthanides when the excitation is performed into the ligand electronic levels. Energy is then channeled into the lanthanide ion excited states by intramolecular energy transfer. This has been termed as the antenna effect or luminescence sensitization. This discovery has been very essential in the utilization and application of lanthanides since now the brightness or luminosity ($L = \epsilon \times Q$, with luminescence quantum yield Q) can easily reach $10^4 - 10^5 \text{ M}^{-1}\text{cm}^{-1}$ determined by the molar absorption coefficients of the surrounding ligands. A simplified Jablonski diagram for the antenna effect of energy transfer processes occurring in a luminescent lanthanide ion is presented in **Figure 2.2.2.1A**. The energy transfer from ligand to lanthanide ions is explained as a three-step process: first, the ligand that surrounds the ion will absorb the light and reach an excited state that is often the singlet state ($S_0 \rightarrow S_1$) in compounds with organic ligands. In the second step, intersystem crossing occurs to longer-lived triplet excited state ($S_1 \rightarrow T_1$). In the third step, the energy transfer from the T_1 state of the antenna to the lowest excited state of the lanthanide ions occurs. Electronic transitions from excited state to the ground state of the lanthanide happens and photons are emitted with characteristics bands in the visible for Eu(III) and Tb(III) and near-IR for Dy(III) and Sm(III) wavelengths. Nevertheless, energy transfer can also occur from the S_1 state of the antenna to the lowest excited state of the lanthanide ions but energy transfer from the T_1 state is more often accepted as the mechanism due to its long lifetime.

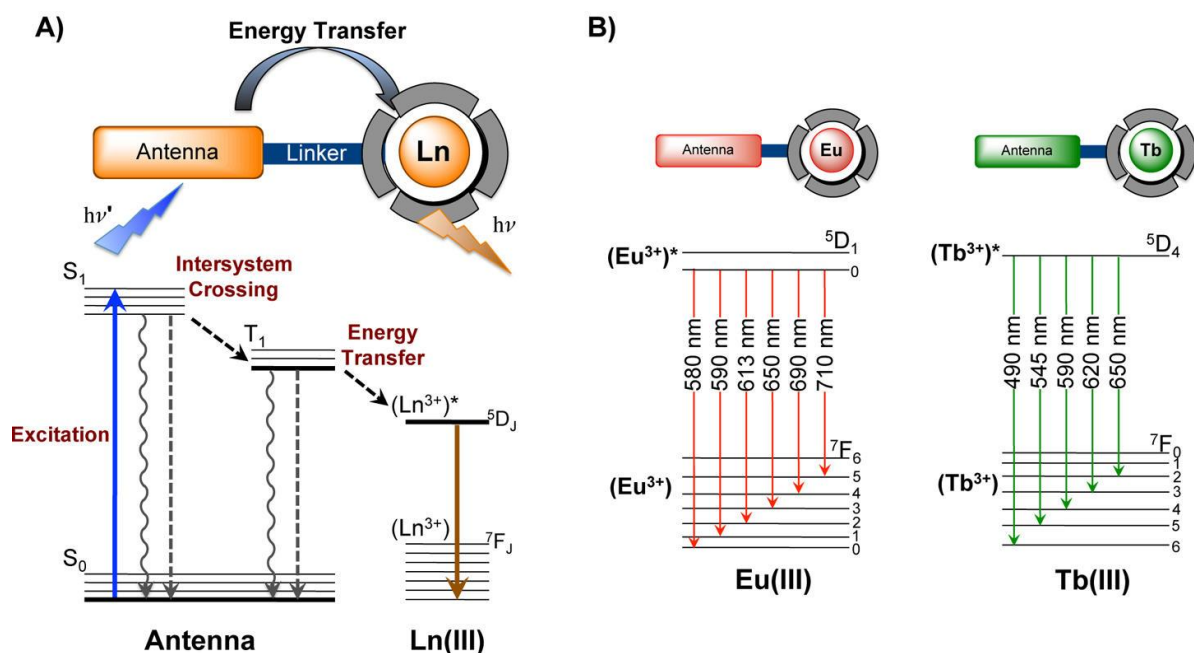


Figure 2.2.2.1: (A) The antenna effect. The general architecture of emissive lanthanide complexes consists of the metal center surrounded by a chelate and equipped with a sensitizer or antenna. The chelate serves to prevent the release of free lanthanides into the biological systems and to protect the lanthanide from quenching from vibrational energy dissipation by oscillators like O–H of water. The antenna harvests energy through high molar absorption to the singlet excited state. After undergoing intersystem crossing to the triplet state, the antenna transfers energy to the excited state of the lanthanide. The radiative transition of electrons from the excited state to the ground states results in luminescent emission from the lanthanide ion. (B) Luminescent 4f–4f transitions of europium and terbium complexes and commonly observed emission wavelengths to emit red and green light, respectively. (Reprinted from reference [42], Copyright 2013 American Chemical Society).

In **Figure 2.2.2.1B** are presented the electronic transitions for commonly observed wavelengths with electronic transitions from $^5D_0 \rightarrow ^7F_J$ ($\Delta J = 0, 1, 2, 3, 4, 5$) for Eu(III) ions and $^5D_4 \rightarrow ^7F_J$ ($\Delta J = 0, 1, 2, 3, 4, 5, 6$) for Tb(III) ions. Based on this mechanism, the design of lanthanide-based optical probes consists of three major components: a luminescent metal center, a protective chelate, and a sensitizing antenna [12], [42].

The overall quantum yield, Q_{Ln}^L , of a lanthanide complex is given by **Equation 1**:

$$Q_{Ln}^L = \frac{I_{Ln}(E)}{I_L(A)} \quad (1)$$

where: $I_{Ln}(E)$ is the number of photons emitted by the lanthanide metal ion;
 $I_L(A)$ is the number of photons absorbed by the ligand;

The large wavelength shift between absorption of light by the ligand and emission of photons from lanthanide ions is called ligand-induced Stokes' shift or Richardson's shift[12]. This large energy gap should exist in order to avoid back energy transfer that results in low quantum yield, short and temperature-dependent lifetimes. The sensitization efficiency, that characterizes the set ligand(s)/Ln(III) ion can be calculated from the following **Equation 2**:

$$\eta_{sens} = Q_{Ln}^L / Q_{Ln}^{Ln} \quad (2)$$

where: η_{sens} represents the sensitization efficiency;

Q_{Ln}^{Ln} is the intrinsic quantum yield of the Ln metal ion when excitation has been performed directly on the 4f excited state;

Q_{Ln}^L is the overall quantum yield;

So in order to fully characterize the process, we need to know the following photophysical parameters: Q_{Ln}^{Ln} , Q_{Ln}^L , τ_{obs} , τ_{rad} and η_{sens} .

From a theoretical point of view to design chromophore ligands that thanks to the antenna effect will outstretch brightnesses of the order of 10^4 of lanthanide ions and 10^6 for terbium nanoparticles is relatively easy and quite straightforward. All you need to do is surround the lanthanide ion with a highly absorbing ligand that has a large molar absorption coefficient. In this way, you will minimize back transfer energy losses and energy losses that may occur from nonradiative deactivation pathways of lanthanide ion. Nonetheless, from a practical point of view is not so straightforward and an easy task to deal with. One must consider different parameters concerning the ligand that are: ligand must form stable complexes over a wide pH range, resist aqueous hydrolysis at subnanomolar concentrations and saturate the Ln(III) coordination sphere to prevent water from coordinating to the lanthanide ion since bound solvent effectively quenches luminescence. As we take into account that sensitization occurs from the triplet-excited state, the ligand or otherwise called antenna should have a high intersystem crossing efficiency (η_{isc}). Therefore, in order to minimize the thermal repopulation of the triplet state the ligand triplet state should have at least 1850 cm^{-1} difference in energy from the lanthanide ion emitting state. Simultaneously, there is not only one mechanism that takes place when we talk about ligand-to-Ln (III) energy transfer but is more

complicated than that. We can count several mechanisms like exchange (Dexter) mechanism, dipolar-dipolar, dipolar-multipolar (Förster type), as well as several electronic levels, both from the ligand(s) and from the metal ion. During the past decades, scientists in the field have worked hard to synthesize the “perfect” couple of ligand-metal ion that has a high luminescence and is adaptable in biological media[12, 39]. In **Figure 2.2.2.2** is depicted Tb doped LaF_3 nanoparticles and the chemical structures of L_2^* maleimide ligand and L_1^* isothiocyanate ligand. Concerning the synthesis of these two ligands a detailed description is given in the thesis of Cyrille Charpentier [43], who was a Ph.D. student in the laboratory of Dr. Loïc Charbonnière, a partner in our joint ANR project “neutrinos”. Tb NPs were synthesized according to previously published procedures [13].

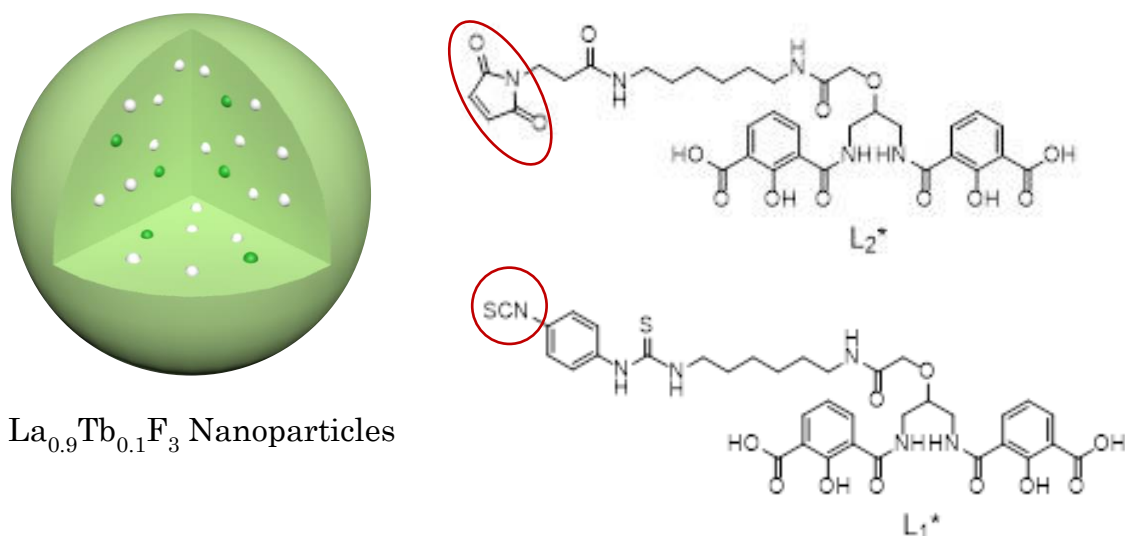


Figure 2.2.2.2: On the left side has depicted the nanoparticles based on lanthanide ions, [Tb doped LaF_3 NPs ($\text{La}_{0.9}\text{Tb}_{0.1}\text{F}_3$)], and the right side presents two synthesized ligands. L_1^ ligand with an isothiocyanate functional group (red circle) and L_2^* ligand with a maleimide functional group (red circle). All components were synthesized in the group of Dr. Loïc Charbonnière [Institut Pluridisciplinaire Hubert Curien (IPHC), Equipe de Synthèse Pour l'Analyse (SynPA), reference[43].*

To summarize, the features that a decent ligand must fulfill in order to obtain an efficient lanthanide-based luminescent probe are the following:

- ✓ Chromophore should possess high molar absorptivity (ϵ)
- ✓ Preferable excitation wavelength above ca. 350 nm (less expensive excitation sources and avoid excitation of endogenous fluorophores)
- ✓ Exquisite tuning of the singlet and triplet electronic states
- ✓ Ln^{3+} cation must have a good shielding by the ligand
- ✓ High solubility in aqueous media, therefore is useful for biological applications
- ✓ High kinetic and thermodynamic stabilities by forming strong coordination the lanthanide cation
- ✓ To form kinetically inert complexes
- ✓ Ideally, obtain an activated labeling function

2.2.2.3 Visible-emitting ions

Lanthanide ions that emit in visible are Pr^{III} , Sm^{III} , Eu^{III} , Tb^{III} , and Dy^{III} (and Er^{III} and Tm^{III} for upconversion nanoparticles). Several lanthanide ions emit both in visible up to 750 nm and in the NIR. The most commonly used visible-emitting Ln (III) ions are Eu^{III} characterized by red-emitting color and Tb^{III} complexes characterized by green-emitting color. The main reasons that these ions are mostly used and studied relies on several important features such as the high quantum yield (>10%), long lifetimes up to millisecond and its usability in commercial applications in biotechnology as well are less affected by the presence of high-energy vibrators. The focus of this thesis will be about Tb^{III} ions based nanoparticles and I will mention briefly some of the highest quantum yield obtained in a solid and liquid state as well the different antenna ligands that were used for each case with the associated references mentioned in literature. In order to isolate and increase luminescence, the ions could be incorporated into inorganic (zeolites) cage-type hosts, organic (chelates or cryptands), polymer matrices (mainly to decrease the energy migration between luminescent ions, concentration quenching) or the use of bulky multidentate organic ligands which will also confer stability at nano to picomolar concentrations. So in this context, plenty of different useful antennae have been synthesized in the past decades that work quite well with the visible ions. One of the first example with the highest overall quantum yield is mentioned in the paper from

Bredol *et al.*, where they present the Tb^{III}-benzoate with a 100% QY excited at 254 nm in solid state[44]. They explain that this could be obtained as a straightforward synthesis as anhydrous white powders. Unfortunately, in water, the quantum yield does not have the same fate. The overall quantum yields reported in water are much lower. In aqueous solutions, the most stable oxidation state is +III for all lanthanide cations. In the paper of Petoud *et al.*, they report a quantum yield as high as 63% in water for Tb^{III} [45]. Practical applications for commercial assays have found ligands based on 2-hydroxyisophalamide (IAM) that provide emissive Tb(III) complexes with a high quantum yield up to ~ 60% that are stable and can be detected up to nanomolar concentrations. For further detailed explanation about quantum yields, synthesis of ligand and other photophysical parameters associated with the visible-emitting ions I invite you to read the review of Bünzli *et al.*, [12]. The data are reported in more detail and with the associated references. In order to overcome this issue of low quantum yield in aqueous solution Ln^{III} complexes can be inserted into micelles or nanoparticles [13, 39, 46, 47]. The paper [13] of Charbonnière *et al.* has reported a brightness of $2.2 \times 10^6 \text{ M}^{-1}\text{cm}^{-1}$ of Tb-doped nanoparticles coupled to L₁₁ ligand with a quantum yield up to ~30% shows high stability in water[13]. An important point to take into account when designing luminescent lanthanide labels is role-played by OH, NH and CH oscillators in the quenching of lanthanide emission. Horrocks and coworkers in the late 1970s demonstrated that the O-H oscillators in the first coordinating sphere of the cations affected the lifetime of Eu and Tb complexes. In order to determine the number of water molecules in the first coordination sphere, the lifetime of the cations was measured in H₂O and D₂O (heavy water or heavy hydrogen because it contains a larger amount of hydrogen isotope deuterium than normal water). The lifetimes were measured in these two media, compared and from that was derived an **Equation 3** that allows us to estimate the number of water molecules present in the first coordination sphere.

$$q = \mathcal{A} \left(\frac{1}{\tau_{H2O}} - \frac{1}{\tau_{D2O}} - \mathcal{B} \right) \quad (3)$$

where: q is inner hydration number;

\mathcal{A} is empirical value proposed by Horrocks, a constant different for each metal;

\mathcal{B} is a term introduced by Beeby and Parker *et al.*, to account for second sphere water molecules;

This work was followed by investigating the influence of other oscillators (NH, amide NH, CH) and outer sphere contributions[32, 48].

2.2.3 Applications of lanthanides

A broad picture of lanthanide application in different field of science is drawn in **Figure 2.2.3.1**. We observe the applications of these luminescent materials in everyday life without even noticing, such as the fluorescent bulb that contains less than 1 gram of Ln phosphor or light-emitting diode (LED) lamp, or a cell phone that contains less than 0.1 grams of rare earth, followed by telecommunications and laser materials. A well-known laser is the neodymium-doped yttrium aluminum garnet (Nd-YAG) laser with its main emission wavelength at 1064 nm, which can be frequency-doubled (532 nm), tripled (355 nm), or quadrupled (266 nm). Luminescence arising from f-f transitions and d-f transitions have found numerous applications. The d-f transition has found its application in scintillators for the detection of ionizing radiation, in white-light LEDs under the form of a yellow phosphor, $\text{Y}_3\text{Al}_5\text{O}_{12}:\text{Ce}^{\text{III}}$ (0.033 mol%). The broad d-f emission from Eu(II) has found application in several different areas as for instance in long persistence materials, in emergency and safety signals, road marking, dials and displays, textile printing and recently they are tested for applications in bio-imaging and energy storage.

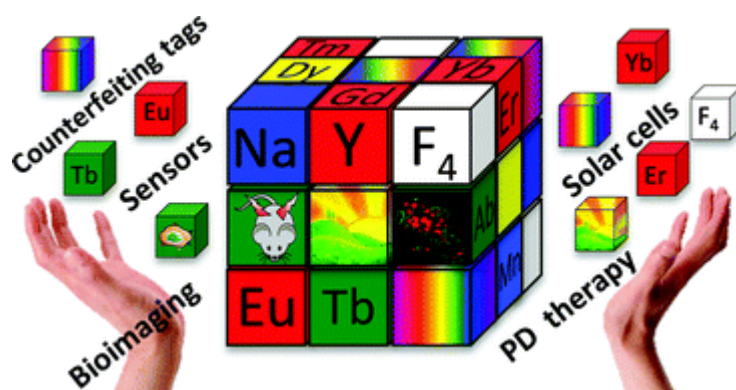


Figure 2.2.3.1: Many-faceted applications of lanthanide luminescence. (Reprinted from reference [49], Copyright 2013 The Royal Society of Chemistry)

The basis of numerous applications arises from the luminescence of f-f transitions. Lanthanide compounds have found their use in time-resolved bioanalysis and

bioimaging. Due to their long lifetime up to a few milliseconds, they are complementary to conventional organic dyes (that have mainly a lifetime up to a few tens of nanoseconds) or semiconducting nanocrystals. The usefulness of long lifetime fluorophores relies on efficient suppression of autofluorescence coming from the solution itself or from the scattering of light in the instrumental setup by introducing a delay between pulsed excitation of the sample and the acquisition of the emitted luminescence signal. The limiting factor in high sensitivity detection is the autofluorescence that all biological samples display, so by suppressing it, automatically the sensitivity of detection (signal to noise ratio) within a sample is highly increased. Since lanthanides have a long decay time, they will continue to emit the following disappearance of the autofluorescence. Each lanthanide has a distinct decay time, so depending on the decay time we can choose to collect the emitted photons in a time-window associated with the decay time of the desired lanthanide. This time-gated window can be varied depending on the experiment in order to optimize the signal-to-noise ratio. Therefore, the detector is turned on after the excitation pulse to integrate the intensity from the lanthanides. As an excitation source is used a pulsed-laser by introducing a time-delay that corresponds to efficient suppressing of all the signals, like background signal correlated with the excitation pulse, direct and multiple scattered excitation light, Raman scattering or endogenous fluorophores (i.e., eukaryotic cells) within the sample[41, 43, 51]. This idea is depicted in **Figure 2.2.3.2**.

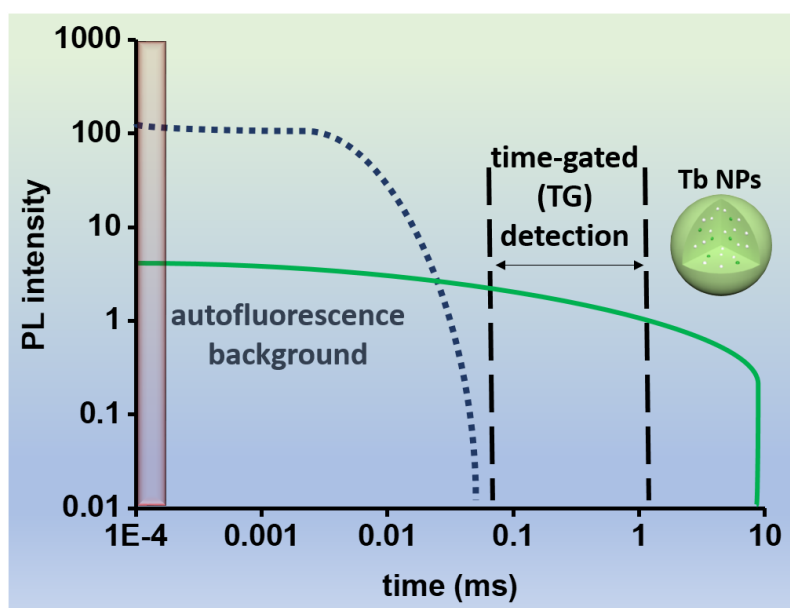


Figure 2.2.3.2: Principle of time-gated detection. Photoluminescence intensity after pulsed excitation plotted as a function of time. (Reprinted from the poster ‘Terbium nanoparticle biofunctionalization and characterization for extracellular biosensing’, Nanax Conference 2019 Hamburg/Germany, V. Cifliku)

The group of Wallace Oy in the 1980s developed the principle of time-resolved detection in the DELFIA[®] system (Dissociation Enhanced Lanthanide Fluorescence ImmunoAssay) for highly sensitive detection of antigens. DELFIA system requires the performance of several steps, like several fixations, washing and separations that are time-consuming. Hence, to overcome these drawbacks, a homogeneous time-resolved fluoroimmunoassay (TR-FIA) was introduced by using luminescent lanthanide chelates in one-step only. This method does not require fixation or washing steps so it results in a less time consuming with high sensitivity for a homogeneous assay, with detection limits in the pM or fM range[5, 52]. The narrow and well-separated emission bands of lanthanide complexes with significant long PL lifetimes allowed for multiplexed detection of several biologically relevant analytes in the same solution, in one-time measurement. A multiplexed detection of microRNA (miRNA) in 2015 was demonstrated from the group of Hildebrandt *et al.* This study has shown FRET from a Tb donor to three different organic dye acceptors (Cy 3.5, Cy 5, and Cy 5.5), otherwise called triplexing[52]. Besides their use as sensitive sensors in solution, lanthanides have found application in luminescence microscopy and especially in time-resolved luminescence microscopy (TRLM) due to their long lifetime, strong stability under UV illumination in live cells, high brightness and discriminated signal due to delay time introduced. A simple set-up of TG PL microscopy is composed of a wide-field inverted microscope, pulsed LASERs or LEDs triggering a delayed detection using an ICCD cameras for TG detection[8, 16, 48]. With this set-up in hand and lanthanides on the other side, we could investigate FRET processes as TRLM is one of the rare tools to allow the observation of molecular interactions in the range of 10 nm in living organisms. Single-molecule detection and visualization of molecule trafficking inside cells is the ultimate target for lanthanide luminescence. Therefore, lanthanide-doped nanoparticles (NPs) have been largely developed and prepared by a simple and reproducible microwave-assisted synthetic protocol in water as described in the paper

of Charbonnière *et al.* [13]. With exceptional brightness, the sensitivity is considerably boosted and the concentration used of lanthanides in/on the cells reached the pM, nM range. Some intriguing work is made on multimodal probes that consist of combining two or more imaging techniques in order to remedy the intrinsic drawbacks to a given imaging technology[54, 55]. A combination of NIR/MRI probes due to the deep penetration of NIR light in biological tissues and good spatial resolution of magnetic resonance imaging with high sensitivity of luminescent probe could be a milestone in biomedicine applications. Quite a lot of efforts are put on cancer detection with luminescent lanthanides, both in solution as *in-cellulo*, but going one-step further they appear to be adequate in drug delivery. For instance, Eu-doped nanoparticles integrated into the channels of porous silica microspheres (YVO₄: Eu^{III} @ SiO₂) have a large loading capacity of doxorubicin (44 wt %) used in the treatment of cancer. This compound could be used in gastric cancer therapy since the intensity of Eu^{III} luminescence correlates with the cumulative release of the drug at low pH[55]. New tools in bioanalysis are upconverting nanophosphors. Upconversion (UC) has an anti-Stokes shift character where the excitation is performed on the high wavelength part of the spectrum, otherwise saying two or more low energy photons are absorbed followed by emission of a more energetic photon. Simply saying, lanthanide-ions doped UCNPs are excited in the NIR with a laser and photons are emitted in the visible/NIR light. UCNPs have found a growing interest in the field of biomedical applications due to their excitation ($\lambda_{\text{exc}} = 980\text{-}800\text{ nm}$) in the so-called biological window resulting in an increased transparency of biological tissue towards NIR light as compared to UV or visible light excitation. The deep penetration depth in biological tissues up to several millimeters to centimeters and minimal photo damage make these compounds very attractive for biomedical applications. To eliminate autofluorescence and light scattering without even illumination, new solution is proposed and this is offered by the use of persistent luminescence nanoparticles (PLNPs). The reason of this name comes from their illumination during hours or even days after the removal of excitation source that could be UV or visible light, X-ray or γ -ray, electron or plasma beam. Few hundred years ago in 1602 Vincenzo Cascariolo in Bologna discovered *Bolognian Phosphor* which was a material that glow in the dark after exposure to light[56]. Investigating this kind of

materials was concluded that excitation energy is stored in traps followed by its subsequent release by thermal deactivation. The most efficient materials in our days are $\text{Eu}^{\text{II}}/\text{Ln}^{\text{III}}$ or $\text{Eu}^{\text{II}}/\text{Mn}^{\text{II}}/\text{Ln}^{\text{III}}$ ($\text{Ln} = \text{Dy}, \text{Nd}, \text{Tm}, \text{Pr}$) co-doped aluminates, silicates and nitridosilicates. These materials can be functionalized and they have been proposed as diagnostics method in quantifying α -fetoprotein (AFP) excreted during cancer cell growth. PLNPs materials are conjugated with AFP-antibody-coated gold NPs and luminescence can be detected without illumination. PLNPs have found use in *in vivo* imaging techniques since they possess the advantages of eliminating autofluorescence and light scattering[49]. A futuristic vision in nanomedicine is to produce energizing nanobiodevices with NIR-driven solar cells, so production of electricity from conversion of NIR light by photovoltaic cells. The group of Chen in 2007 have made some initial attempts by proposing a solar cell device with a 4 μm thick embedded layer of $[\text{Na}(\text{Y}_{1.5}\text{Na}_{0.5})\text{F}_6:\text{Yb} (20\%), \text{Er} (2\%)]$ upconverting nanorods ($0.2 \times 1.0\mu\text{m}$). Under ($\lambda_{\text{exc}} = 980 \text{ nm}$) illumination with 1 W power, the overall laser-to-electricity conversion yields amounts of 0.047% corresponding to a maximum power of 470 μW . The yield of upconversion has been estimated 0.45%. There is still room for improvement. The same group has proposed a better version of this device by changing the percentage composition $[\text{NaY-F}_4:\text{Er} (2\%), \text{Yb} (20\%)]$ of these materials and using one-step hydrothermal synthesis for preparation with biological compatibility enhancement by replacing the liquid I_3/I_2 electrolyte with a stable succinonitrile-based gel electrolyte. The same parameters were used (980nm laser, 1W power) and the yield of laser-to-electricity conversion has been increased almost twice 0.09% with a power of 44.5 μW . The laser-electricity conversion decreases up to 0.019% with a power of 22.2 μW when the cell is covered with 1mm layer of chicken skin as a biological model. Theoretically, this model can power 2000 devices fabricated with nanowires or nanotubes since the energy required to energize these materials is 10nW per nano item. Other exciting fields that the luminescence of lanthanide materials covers in forensic science are security inks, counterfeiting tags, or identifying codes. The powerful tool of luminescence materials helps in identifying fake from real euro bills, just by looking at them under UV light. In this case, a downshifting mechanism is used. These euro bills contain a mix of different phosphors and in the case of euro bills contains Eu^{III} (orange-red emission)

and Eu^{II} (blue and green emission) phosphors, presented in **Figure 2.2.3.3**.

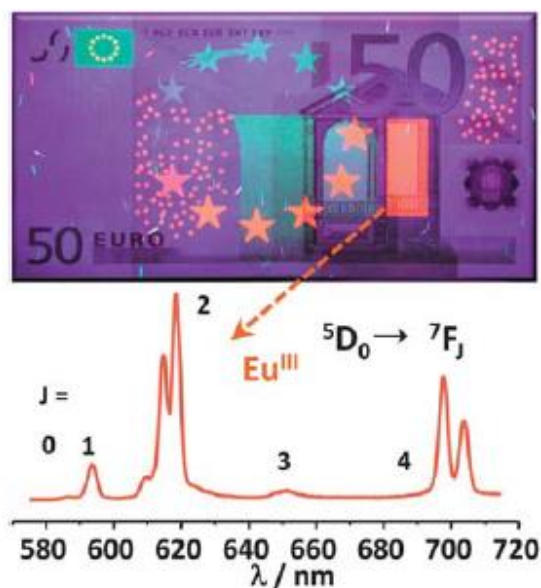


Figure 2.2.3.3: (Top) Fifty-euro bill illuminated under UV light at 366 nm and (bottom) emission spectrum of the orange-red luminescence, typical of a Eu^{III} complex. (Reprinted from reference [49], Copyright 2013 The Royal Society of Chemistry).

The materials that use the mechanism of upconversion like $\beta\text{-NaYF}_4:\text{Yb,Ln}$ ($\text{Ln} = \text{Er}, \text{Tm}$) nanoparticles have found a very useful application in identifying fingerprints by tuning their lifetimes, excitation power and different composition of the nanocrystals as well as their morphology. Potential new applications that lanthanides have found their use are in telecommunication, luminescence thermometry, pressure and impact sensors based on triboluminescence, solar energy conversion and quantum information processing. One has to keep in mind that even though today the knowledge of these materials is better known than a few years ago when mainly the experiments were in trial-and-errors, each lanthanide is a special case and each application has special requirements[12, 41, 50] !

2.3 Time-Resolved Fluorescence Microscopy

Fluorescence lifetime has become a popular tool in the past decades, starting from the 1980s when it was already recognized that the use of TG together with the use of lanthanide complexes could enhance the detection limit compared to regular fluorescent dyes[57]. In the early 1990s appeared the first microscopy systems that adapted the TG method[50]. By employing time-resolved technique we are able to measure and discriminate the PL lifetime of every fluorophore[14]. Fluorophores are used to tag different molecules and by employing fluorescence-based techniques, qualitative and quantitative information could be obtained[8, 48, 59]. The presence of autofluorescence makes it difficult to discriminate from the synthetic fluorophores signals. Even though spectral selection techniques (excitation and emission filters) can help in signal discrimination, it still remains a problem to solve since components like flavins, vitamins and co-enzymes have a broad emission spectrum (from blue to red) and as well they are excited in the UV[59]. To overcome this problem: A) fluorophores with longer lifetimes (ms) should be used and B) a detector that can be maintained in the off-state for a resolving period (gate-delay) while short-lived fluorescence fades away must be put into practice[60]. A very useable device that was introduced for image recording was a slow-scan charge-coupled device (CCD) camera. CCD camera has the ability to generate high image quality under low light due to its ability to directly integrate photons as an electron at a high quantum efficiency during exposure[60, 62]. Erkki Soini and his colleagues in Turku developed a series of chemical compounds that strongly encapsulated the lanthanide, thereby preventing the quenching effect of water molecules and had an increased quantum yield thanks to the use of chromophores “antenna molecules” in the chelate compounds[58, 60]. When combined lanthanide-doped NPs with TG imaging technique it makes it possible to image in the second biological window (1000-1350 nm) that can provide a better signal-to-noise ratio and higher penetration depth for in vivo imaging[62]. In this thesis, TG imaging was employed in combination with TbNPs (long lifetime) to efficiently detect EGFR expression on different cell lines at very low nanomolar concentrations.

2.4 The EGFR family of receptor tyrosine kinases

The EGFR (or ErbB) family of receptor tyrosine kinases (RTK) consists of four different receptors: EGFR (also called ErbB1 or HER1), ErbB2 (HER2), ErbB3 (HER3) and ErbB4 (HER4). They bind different subsets of a dozen of ligands and trigger activation of a variety of downstream cascades. The discovery of this signaling system dates back to the 1950s when Dr. Stanley Cohen and coworkers isolated the epidermal growth factor (EGF) from the submaxillary gland of the mouse. They report that the role of the growth factor is to stimulate epidermal proliferation and keratinization[64, 65]. The following year's scientists performed experiments on understanding the diverse physiological effects of EGF stimulation, but the identification of the receptor that is known today as 'EGFR' did not come until the late 1970s [66, 67]. To complete this family, in the following years 1981-1985 was discovered human ErbB2 (Her2) and its rodent homolog (Neu) [67], followed by ErbB3 in 1989 [68] and ErbB4 in 1993 [69].

2.4.1 Structure and molecular mechanisms of EGF receptors

The epidermal growth factor receptor and three family members (HER2, HER3, and HER4) are types I transmembrane proteins. They are composed of three parts, **Figure 2.4.1.1**: heavily glycosylated and disulfide-bonded ectodomain (extracellular region) that provides a ligand-binding site divided into four subdomains (I-IV), also known as LD1, CR1, LD2, and CR2 subdomains respectively; a single transmembrane domain (TM); and a large cytoplasmic region that encodes a tyrosine kinase and multiple phosphorylation sites (intracellular region)[70].

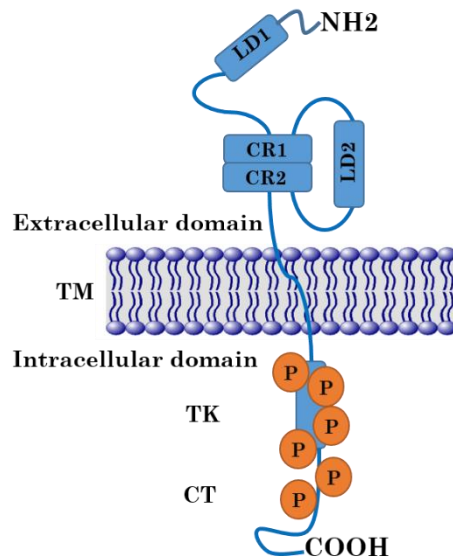


Figure 2.4.1.1: The basic structure of the EGFR transmembrane proteins. In the extracellular domain, LD1 and LD2 are two repeated ligand-binding domains. CR1 and CR2 are two repeated cysteine-rich regions. TM indicates the short transmembrane spanning sequences. In the intracellular domain, TK is a catalytic tyrosine kinase and CT is the carboxyl-terminal tail. Circled Ps are the phosphorylation sites within the TK and CT regions. (This figure is revised based on the reference [70]).

EGF receptors are present at the plasma membrane as both monomers and dimers, including homo- and hetero-dimers. They play an important role in embryonal development of the nervous, cardiovascular and gastrointestinal system. However, the EGF receptor is present and overexpressed in several carcinogenic cells like; A431 human epidermoid carcinoma; SNU16 and KATOIII gastric cancer; MDA-MB-231, MCF-7, SUM229 breast cancer; EBC-1 and H1993 non-small lung cancer cell lines, etc. A431 is a cell line that expresses abnormally high levels of EGFR and is employed in the current research application by taking advantage of EGFR overexpression as a diagnostic method in cancer detection. Quite a lot of studies urge the implementation as therapeutic targeting of these receptors even though they retain complex dimerization mechanisms[71].

In the structure of EGFR family domains II and IV, called CR1 and CR2 respectively are homologous cysteine-rich domains, whilst domain I and III mediate ligand binding and share 37% amino acid identity. Albeit their similarities, these receptors have also important differences among them. The first difference is that they recognize different

ligands, except for HER2 that does not bind to any known ligand but functions as a co-receptor for the rest of the EGFR family. The second difference is ascribed to the kinase domain of HER3 receptor that lacks enzyme activity and requires heterodimerization for *trans*-phosphorylation of its kinase domain. Ligands that bind only to EGFR are EGF and TGF- α ligands, whilst neuregulins bind only to HER3 and HER4, **Figure 2.4.1.2A**. The resting form of EGFR, HER3, and HER4 receptor keeps the dimerization arm (domain II of extracellular part) unexposed and needs a ligand binding in order to adopt a conformation compatible with dimerization. Upon ligand binding to domains I and III a conformational change exposes the dimerization arm, promoting receptor dimerization. The dimerization arm of HER2 is constantly exposed, forming heterodimers with other ligand-bound receptors. Ensuing ligand-mediated receptor dimerization, the formation of an asymmetric kinase domain dimer promotes allosteric activation of one kinase domain, which then performs *trans*- and auto-phosphorylation of the cytoplasmic tail of both receptors, **Figure 2.4.1.2B**.

Several signaling pathways like [Ras/MAP kinase, phospholipase C γ , signal transducer, activation of transcription (STATs) and phosphatidylinositol (PtdIns) 3-kinase] will be triggered by EGF receptor tyrosine kinase. The activated receptor dimers may also trigger other mechanisms like endocytosis, both clathrin-dependent and independent by facilitating the internalization of the entire complex through lysosomal degradation or recycling of the receptors to the plasma membrane. Oncogenic mutants that lack some part of the extracellular domain or most of it, have been shown to perform a spontaneous oligomerization accompanied by tyrosine phosphorylation[70, 71]. The EGFR family receptors are highly studied due to their major role in the cellular progresses managing cell cycle, proliferation and apoptosis. Overexpression of EGFR family receptors and gain of function mutation are the dominant mechanisms observed in cancers. For instance, the overexpression of EGFR has been observed in numerous cancers with relatively high percentages.

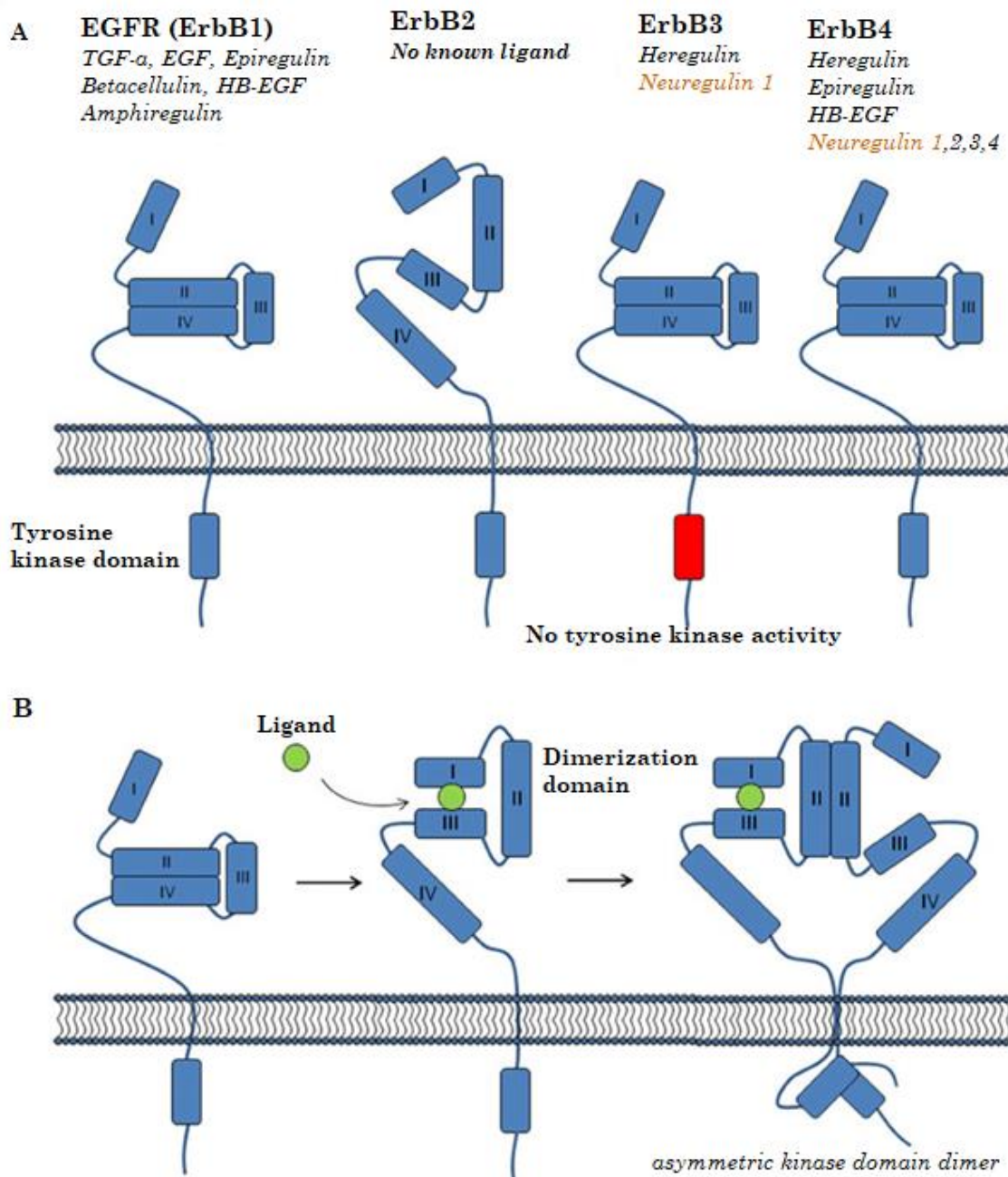


Figure 2.4.1.2: The EGFR receptor family. (A) A schematic showing the structure of the four EGFR family receptors (EGFR, HER2, HER3, and HER4), including the four domains within the extracellular region, the intracellular tyrosine kinase domain and the ligands specific to each receptor. EGFR, HER3, and HER4 are shown in the unliganded, "closed" conformation, except for HER2 receptor that does not require ligand binding due to its permanent exposure of the dimerization arm. (B) The conformational change associated with the ligand binding, receptor dimerization and formation of an allosteric kinase domain dimer. (Reprinted from reference [9], Copyright 2016 Kennedy, Hastings, Han and Croucher).

For example, triple-negative breast cancer was found with 60% overexpression, head and neck squamous cell carcinomas (HNSCC) overexpressed at 80%, non-small-cell lung cancer had an overexpression of 60% and glioblastomas an overexpression of 40% of EGFR. Since the receptors of EGFR family have been identified as potent oncogenes, numerous therapeutic agents have been developed in order to prevent their role in cancer proliferation and survival. Two classes of drugs widely studied and utilized are monoclonal antibodies and small molecule tyrosine kinase inhibitors (TKIs). Monoclonal antibodies act on the receptor's extracellular domain, interfering with the receptor through increased internalization, activating antibody dependent cell-mediated cytotoxicity or disrupting receptor dimerization. TKIs function by inhibiting the cytosolic tyrosine kinase domains through either direct competition with adenosine triphosphate (ATP) or allosteric inhibition of ATP binding. Although the task has been quite challenging, still some prominent monoclonal antibodies like cetuximab and panitumumab target EGFR with improved survival rates for patients with metastatic colorectal cancer harboring a wildtype KRAS⁵. Cetuximab is an approved therapeutic agent and has an increased efficiency once combined with platinum-based chemotherapy and radiation therapy for head and neck squamous cell carcinomas. Afatinib is another drug that can suppress TKIs (tyrosine kinase inhibitors) and EGFR at patients with advanced non-small cell lung cancer (NSCLC). By binding covalently to all homo- and heterodimers formed by members of the ErbB family (including EGFR), afatinib irreversibly blocks signals from these receptors and slows the growth and spread of cancer. Another promising inhibitor of the intracellular domains of the receptor tyrosine kinase EGFR and HER2 is Lapatinib. This drug is approved for inhibition of HER2 receptor overexpressed in breast cancer upon patient relapse following standard treatment with chemotherapy and trastuzumab. To target HER3 receptor there is no clinically approved monoclonal antibodies but different strategies are under investigation. Since this receptor does not embrace a tyrosine kinase activity,

⁵KRAS was identified as an oncogene in Kirsten RAt Sarcoma virus. The KRAS gene provides instructions for making a protein called K-Ras. The protein relays signals from outside the cell to the cell's nucleus. These signals command the cell growth, proliferation, maturation and differentiations.

is infeasible to be targeted with a small molecule inhibitor. However, keeping in mind that HER3 receptor forms heterodimers with HER2 receptor, a different strategy can fit by targeting simultaneously HER2 and HER3. Recent data from preclinical studies models demonstrate the simultaneous activity of a bispecific antibody (MM-11) as a single agent and in combination with trastuzumab. Even though many efforts have been made to target and inhibit efficiently these receptors the success met was not so satisfactory. This may come from not completely explored mechanisms of the dimerization profile. For many years, the dimerization was thought to occur only within EGFR family members, and co-immunoprecipitation was the only experimental technique utilized to observe all of these receptors interactions, but new studies suggest that due to the plasticity of these receptors, the pool of potential heterodimers is much larger than previously thought. In order to overcome the challenge-acquired resistance, is crucial to obtain a rigorous understanding of these potential interactions and their effect on EGFR family signaling pathways. So far, their use as monotherapy is reported inefficient to target cancer cells, so more sophisticated approaches need to be developed. Optimistically, the progresses in untangling the under-appreciated mechanisms of these potent oncogenes will manage to be more effective on to what we expect today from personalized medicine [7, 9, 11, 22].

3. Stability tests of Terbium Nanoparticles

3.1 Introduction

The importance of nanoparticles/nanomaterials for biomedical applications has hugely increased thus high stability and biocompatibility particles with low toxicity are necessary requirements. It is of primary importance to know the colloidal stability of the nanoparticles (NPs) used in solution for a better optimization considering the final nanoparticle intended bio distribution. In order to develop well-defined nanoformulations for use in therapeutic relevance, an adequate characterization of NPs with dynamic light scattering (DLS) and zeta potential (ZP) should be performed. Nanomaterials do not behave the same as bulk materials, so sufficient characterization

is necessary to understand the surface charge, particle size and chemical (surface functionalization with different ligands), crystallinity and properties of NPs. The safety issue arises when it comes to the size of NPs, so the easy, simple and reproducible tools like DLS and ZP have emerged from the realms of physical colloidal chemistry to ascertain the particle size and surface charge[74].

To get some answer about these inquiries, I performed three studies to observe the stability of bare TbNPs.

In the first study I investigate the influence of time and media on the size of bare TbNPs for a period of two months. The second study demonstrate the influence of pH on the size of these TbNPs dispersed in diH₂O, and in the third study are presented the results about the effect of sonication as a function of time on the particle size of TbNPs dissolved in 10mM HEPES pH 7.0.

These analyses were performed by using DLS also known as photon correlation spectroscopy, which gives us the information concerning the hydrodynamic radius (R_H) of these nanoparticles by measuring the Brownian motion and correlates with to the size of the particles. The nanoparticles in solution are illuminated with a laser (He-Ne, 4.0mW at $\lambda_{exc} = 632.8\text{nm}$)[75] and the intensity is analyzed in the scattered light.

ZP also termed as electrokinetic potential investigates the charge of the NPs at the slipping/shear plane[76].

The sonication effect is used to speed up the dissolution, to evenly disperse the nanoparticles in liquids by breaking up the intermolecular interactions, breaking up the aggregates already formed in solution[77]. The investigation of the pH range is important for the biological samples since the different cell compartments have different pH values and a hint of how the NPs size changes over the different pH is necessary before jumping into the *in-vivo* experiments. The temperature is also important because the cells in order to survive and proliferate need to be at 37°C. By performing these tests stability, I would like to have the answer to some important questions such as the stability over time. For how long we can use the nanoparticles before they aggregate and make it difficult to break up the aggregates even with sonication? What is the most suitable media/buffer to preserve the bare TbNPs? If possible, can we preserve their characteristics in buffers that are 'good' buffer for *in-cellulo* experiments and at the

same time good for the size and luminescence of the NPs?

Following the chapter I will present the data collected from DLS and ZP for the NPs in this study.

3.2 Materials and Methods

3.2.1 Materials

$\text{La}_{0.9}\text{Tb}_{0.1}\text{F}_3$ NPs in diH_2O , were kindly provided from the group of Dr. Charbonnière, research director and our collaborator in the ‘neutrino’ project at Institut Pluridisciplinaire Hubert Curien (IPHC)/CNRS, Strasbourg. Trizma® hydrochloride (Tris-HCl), hydrochloric acid (HCl), sodium hydroxide (NaOH), sodium fluoride (NaF) and ethanol solution (purity 95% >) were purchased from Sigma-Aldrich. HEPES (4-(2-hydroxyethyl)-1-piperazineethanesulfonic acid) was purchased from ThermoFisher Scientific. Disposable polystyrene cuvettes (DTS0012) and disposable folded capillary cell (DTS1070) were purchased from Malvern PANalytical Company and used for DLS and ZP measurement, respectively. Ultra-pure duster was purchased from Techspray renew company. Deionized water (diH_2O) was obtained in the lab from the machines purchased at ELGA LabWater.

3.2.2 Chemical synthesis of Terbium Nanoparticles

The use of LaF_3 allows for low energy phonons as well as a strong thermal and environmental stability. LaF_3 is a host and is transparent in the visible and NIR regions that can be easily doped with all the lanthanide ions. In **Figure, 3.2.2.1** is presented a scheme of the synthesis of $\text{La}_{0.9}\text{Ln}_{0.1}\text{F}_3$ NPs. This technique has been realized in water using a microwave irradiation. Solutions of LaCl_3 , LnCl_3 and NH_4F have been prepared in milliQ water. The first step of the synthesis consists in mixing LaCl_3 and LnCl_3 with amounts that will determine the doping of nanoparticles. The second step is to add dropwise the solution of NH_4F at room temperature. This added volume of NH_4F corresponds to three equivalents to one equivalent of lanthanides. The third step is to warm the mixture at 150°C in a microwave oven for 12 minutes. The synthesis in a

microwave irradiation allows getting regular heating with a quick and precise temperature rise, quick synthesis at medium temperature and is expected to produce nanoparticles with narrow size distribution. After centrifugation, the supernatant was eliminated and the white solid was dispersed in milliQ water using ultrasounds. After 1h at 60°C, $\text{La}_{0.9}\text{Ln}_{0.1}\text{F}_3$ NPs have been obtained with a yield of 36%[13].

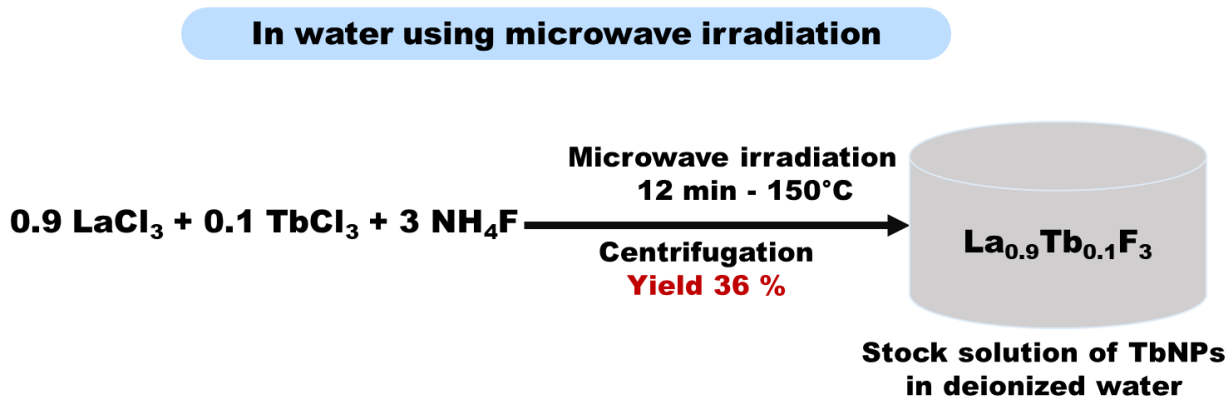


Figure 3.2.2.1: Scheme that shows the synthesis of TbNPs by using a microwave irradiation technique.

This synthesis were performed from the group of Dr. Charbonnière, our collaborator in the ‘neutrino’ project at Institut Pluridisciplinaire Hubert Curien (IPHC)/CNRS, Strasbourg.

3.2.3 Sample preparation for zeta potential measurements

The disposable folded capillary cells (DTS10700) were used for charge measurements. Before using the cell, few precautions and cleaning steps need to take place to avoid dust and bubble formation. Two syringes were used, one for filtered diH_2O and the other one for ethanol. First, we flush the cell with ethanol to facilitate wetting. Second, we fill the syringe with diH_2O , placed in one of the sample ports on the cell, and then flush the content of the full syringe through the capillary. This process was repeated four times, before removing the syringe and performing a final flush with dispersant being used for the measurements, for instance (diH_2O ; 10mM Tris/HCl, pH 7.2; or 10mM Tris/HCl, 1mM NaF pH 7.2). After all this cleaning process has taken place, the cell is ready to be used. When inserting the cell, we must ensure that the Malvern logo faces towards the front of the instrument (Nano ZS, ZEN3600) and be sure to the correct cell in the

software before running the experiment. The measurements were performed three times in a row. All the samples were sonicated 1 hour before the measurements were performed and the sonicate temperature was kept at 20-25 °C by continuously adding ice.

3.2.4 Sample preparation for dynamic light scattering measurements

Disposable polystyrene cuvettes (DTS0012) were used to perform DLS measurements. This cell does not require further cleaning, but once the package of the sample is open, dust may enter the cell. To avoid any dust, I used an ultra-pure duster spray. Later I filled the prepared solution of 1mL volume inside the cell and placed a cap on the top of the cell. The cell was inserted inside the instrument (Nano ZS, ZEN3600) and the experiments were performed three times in a row. All the samples were sonicated 1 hour before the measurements were performed and the sonicate temperature was kept at 20-25 °C by continuously adding ice.

3.2.5 Instrumentation in DLS measurements

A typical DLS system is composed of six components: a laser that illuminates the sample, a detector (in our case placed at 173° angle to detect backscattering) that measures the intensity of the scattered light, attenuator that reduces the intensity of the laser (depends on the sample concentration), a cell, a digital signal processor called a correlator and a computer. The correlator compares the scattering intensity at successive time intervals to derive the rate at which the intensity is varying. The scheme that shows the instrumentation of DLS is depicted in **Figure 3.2.5.1**.

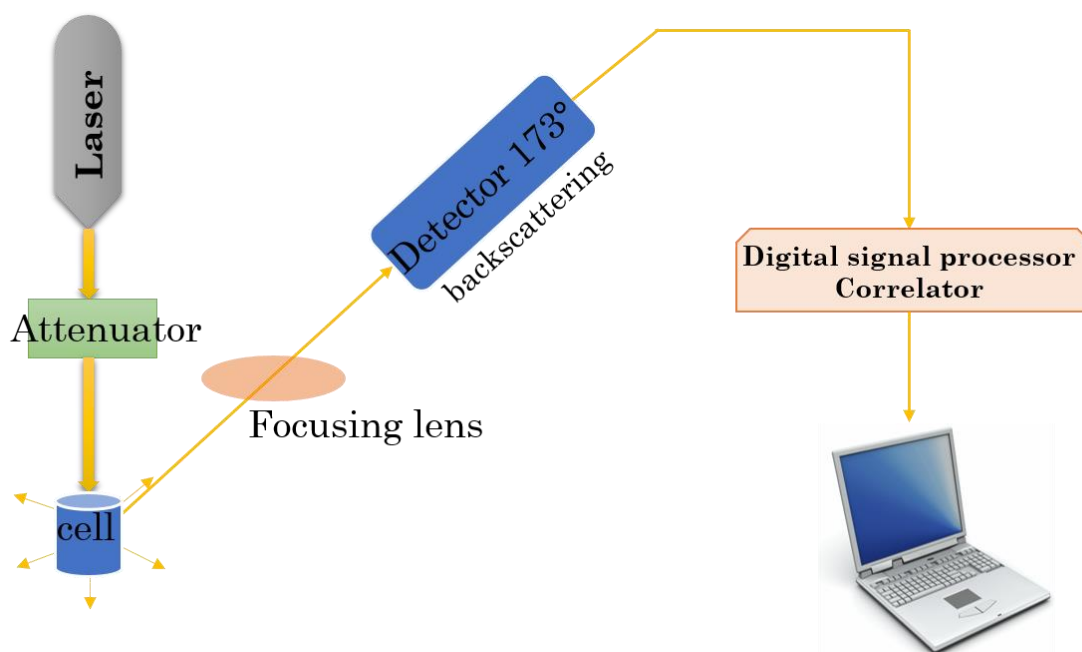


Figure 3.2.5.1: Scheme that shows the instrumentation of DLS, in this case is depicted the Malvern Zetasizer Nano SZ that we use in the lab. This figure is revised based on the reference [74].

The laser used is He-Ne, 4.0 mW at 633 nm wavelength that provides a stable beam of coherent monochromatic light, coordinated to an attenuator that alters the power of the laser. The hydrodynamic diameter of particles that can be measured is within the range of 0.6 nm to 6 μm . The DLS instrument is equipped with an avalanche photodiode (APD) detector with quantum efficiency $> 50\%$ at 633 nm. The detector is placed at 173° angle to detect backscattering. There are several advantages on measuring the backscatter: the incident light does not have to travel through the entire sample thus higher concentration can be measured, thus the effect known as multiple scattering, where the scattered light from one particle is itself scattered by other particles, is reduced and the effect of dust is greatly reduced. Upon experiment realization, the data are stored in the retrievable database where they provide typically the z-average size and size distribution with polydispersity index (PDI) over intensity, volume and number.

3.2.6 Instrumentation in ZP measurements

The same Malvern Zetasizer (Nano SZ) instrument is used to measure ZP. ZP is composed of seven main components: laser, cell, detector, digital signal processor, computer, attenuator and compensating optics, **Figure 3.2.6.1**. The measurements are

performed at any point within the cell, thanks to the improved laser Doppler velocimetry method, the M3 measurement technique and the application of Phase Analysis Light Scattering (PALS). Compensation optics are installed to correct for any differences in the cell wall and the dispersant refraction within the scattering beam path by maintaining the alignment of the scattering beams.

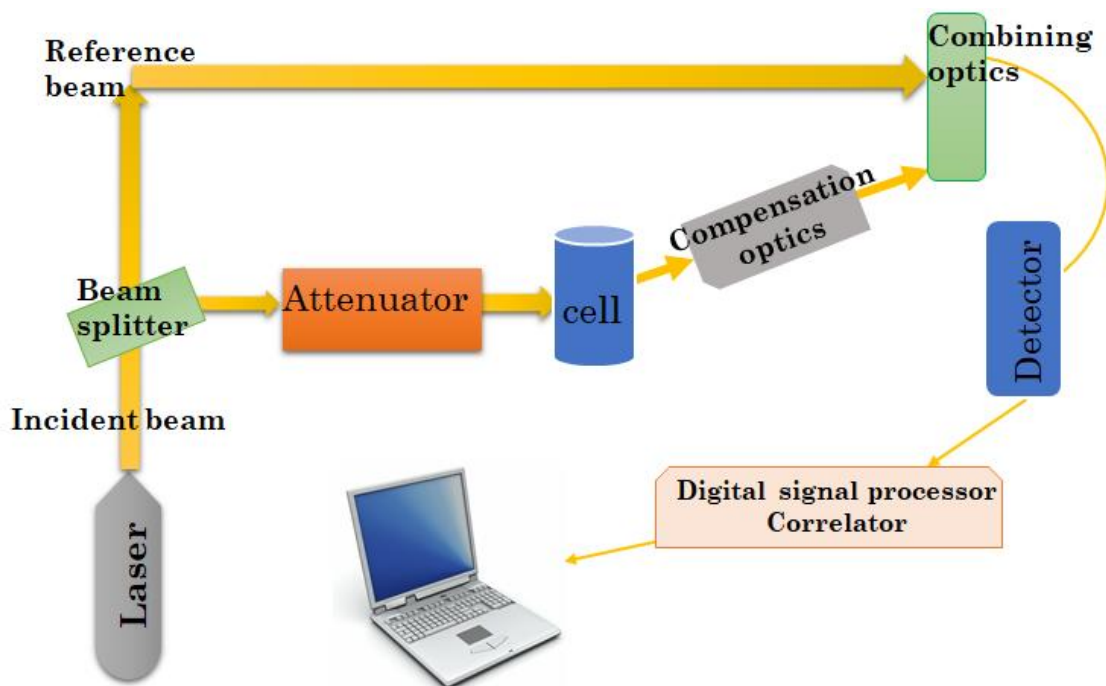


Figure 3.2.6.1: Scheme that shows the instrumentation of ZP measured by electrophoretic light scattering, in this case is depicted the Malvern Zetasizer Nano SZ that we use in the lab. This figure is revised based on the reference [74].

Once an electric field is applied, the electrophoretic mobility is measured and consequently the ZP. These data are both presented on the Zetasizer software. During electrophoresis, the mobile particles scatter an incident light. The scattered light has different frequency than the original laser because particles are considered mobile. Therefore, the frequency shift is proportional to the speed of the particles (*Doppler shift*). The laser beam is split into two beams by a beam splitter, one is directed towards the sample and the other one is used as a reference beam. The light that is scattered from the cell is combined with the reference beam to determine the Doppler shift. Since the Doppler shift was proportional to the velocity, we can deduce the particle velocity and then through a series of several mathematical equations the ZP is measured.

3.3 Results and Discussion

3.3.1 Influence of time and media on the size of bare TbNPs

Size investigation of the NPs over a period of two months were performed simultaneously with the buffer stability (diH₂O; 10mM Tris/HCl, pH 7.2; 10mM Tris/HCl, 1mM NaF pH 7.2) at final concentration of TbNPs [8.5×10^{-9} M]. Important information concerning their hydrodynamic radius were obtained. All the results were put together in table and figure format (**Table 3.3.1.1; Figure 3.3.1.1**).

Table 3.3.1.1

| Day | Peak | diH ₂ O | | | 10mM Tris/Cl, pH 7.2 | | | 10mM Tris/Cl, 1mM NaF pH 7.2 | | |
|-----|------|--------------------|------|----------|----------------------|------|----------|------------------------------|------|----------|
| | | Size (d.nm) | PDI | % Number | Size (d.nm) | PDI | % Number | Size (d.nm) | PDI | % Number |
| 0 | 1 | 86.3 ± 16.2 | 0.13 | 100 | 669.6 ± 304.2 | 0.26 | 39.3 | 359.6 ± 132.9 | 0.16 | 100 |
| | 2 | - | | - | 197.2 ± 59.5 | | 60.7 | - | | - |
| 7 | 1 | 142.6 ± 24.1 | 0.31 | 100 | 4471 ± 990.8 | 0.45 | 23.6 | 443.2 ± 230.2 | 0.26 | 25.6 |
| | 2 | - | | - | 1130 ± 305.4 | | 76.4 | 101.4 ± 26.3 | | 74.4 |
| 15 | 1 | 89.4 ± 16.9 | 0.13 | 100 | 1954 ± 944.6 | 0.39 | 25.9 | 405.5 ± 176.1 | 0.27 | 21.7 |
| | 2 | - | | - | 476.0 ± 169.5 | | 74.1 | 96.01 ± 25.9 | | 78.3 |
| 30 | 1 | 43.7 ± 15.8 | 0.18 | 37.6 | 3502 ± 1248 | 0.5 | 21.3 | 814.8 ± 367.3 | 0.29 | 99.8 |
| | 2 | 20.56 ± 3.5 | | 62.4 | 716.3 ± 192.8 | | 78.7 | 5112 ± 793.7 | | 0.2 |
| 39 | 1 | 89.8 ± 15.9 | 0.15 | 100 | 1272 ± 528.4 | 0.26 | 100 | 953.9 ± 503.4 | 0.27 | 60.8 |
| | 2 | - | | - | - | | - | 4944 ± 720.1 | | 0.3 |
| | 3 | - | | - | - | | - | 256.1 ± 58.2 | | 38.8 |
| 60 | 1 | 93.1 ± 16.7 | 0.18 | 100 | 280 ± 69.3 | 0.27 | 49 | 920.5 ± 353.6 | 0.39 | 99.3 |
| | 2 | - | | - | 741.2 ± 408.4 | | 51 | 5285 ± 717.2 | | 0.7 |

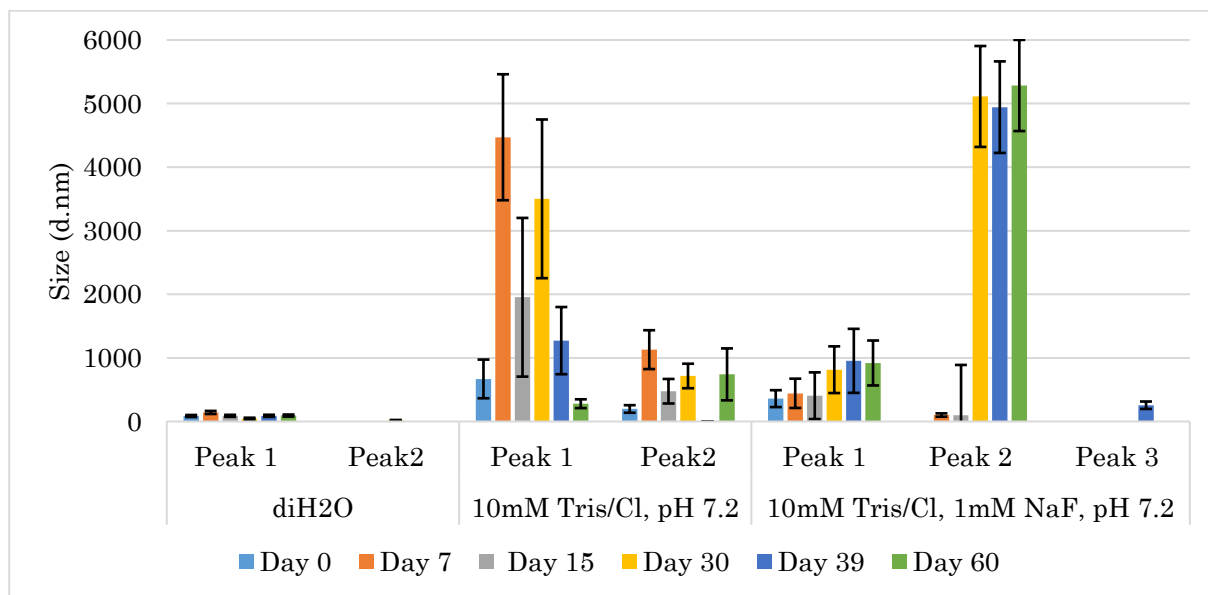


Figure 3.3.1.1: DLS measurements at 25°C of bare TbNPs [8.5×10^{-9} M] over period of 60 days and at three different buffers (diH₂O; 10mM Tris/HCl, pH 7.2; 10mM Tris/HCl, 1mM NaF pH 7.2), performed in Malvern NanoZS instrument.

From this big figure with so many data, we could ‘zoom in’; in each of the media and below is presented the figure of bare terbium nanoparticles dispersed in diH₂O media (Figure 3.3.1.1A).

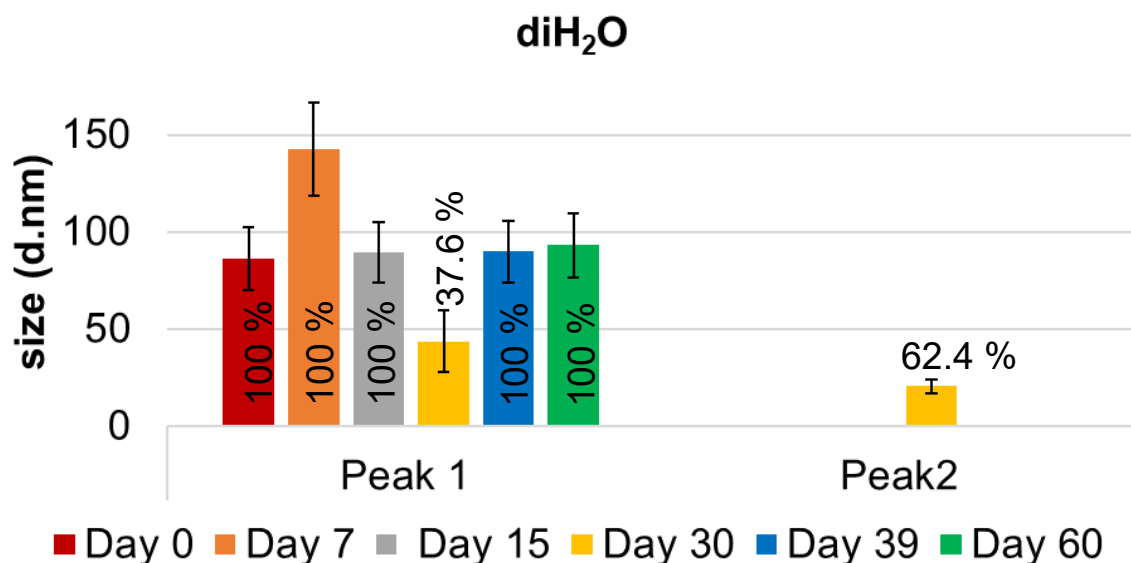


Figure 3.3.1.1A: DLS measurements at 25°C of bare TbNPs [8.5×10^{-9} M] over period of 60 days and at diH₂O, performed in Malvern NanoZS instrument.

The original solution of bare TbNPs was dissolved in diH₂O. From this mother solution were performed the dilution of the NPs in a NaF containing buffer (10mM Tris/HCl, 1mM NaF pH 7.2) and 10mM Tris/HCl, pH 7.2. The reason that NaF was added on the Tris/HCl buffer at 1mM was due to the strong coordination of the fluoride ions at the surface of the NPs thus these ions will not impede ligand coordination at the NPs surface but mainly cover the surface of the NPs by limiting non-specific interactions. This phenomenon was observed from the group of Dr. Charbonnière (our collaborator) while performing FRET experiments. According to their experiments, the weak coordination of the fluoride ions at the surface of the NPs helped to reduce the surface charge of the NPs, to limit non-specific interactions. In addition, another important phenomenon that was observed from Doctor Charbonnière et al., back in 2006 [47] was that when adding potassium fluoride to the buffer the luminescence of TbNPs will increase such as lifetime and quantum yield. In our case, the addition of NaF would helped in avoiding the interactions and possible agglomeration of bare nanoparticles between each other. However, we should avoid higher concentrations of fluoride ions

because it is a high competitor of the ligands and we lose photosensitization. The reason that the NPs need to be dispersed in a buffer rather than staying in diH₂O is due to the leaching effect. The TbNPs will lose their luminescence over time if they are dispersed in diH₂O from the role-played by OH oscillator of water because of the high energy vibration in the quenching of lanthanide emission. Therefore, is really important to store them in a suitable buffer[97, 98].

From the table 3.3.1.1 we observed that TbNPs dispersed in diH₂O from day 0 to day 7 the size in diameter has an increase of ~ 1.6 fold, but the percentage number (%) shows a unified peak. The polydispersity index (PDI) for DLS typically depicts the intensity of light scattered by various fractions of the particles differing in their sizes and is calculated by $(\text{width}/\text{mean})^2$ for each peak. When $\text{PDI} \leq 0.1$ the solution is considered highly monodisperse, while the values of 0.1-0.4 are considered moderate and when $\text{PDI} > 0.4$ the solution is considered highly polydisperse. Taking into consideration the comments given in the review article[74] about the solutions dispersed in diH₂O we might observe a slight increase of the size by 2-10 nm due to the absence of ions, which fails to shield the long-distance interactions between particles, hence obtaining larger size than the actual. Therefore, on day 0 TbNPs in diH₂O have a size in the nanometer range and are monodispersed. At day 7, the size increased and they are moderately polydisperse. At day 15, the size decreased and they become again monodisperse. After a month, we observe a dualization of the peak into two peaks with their associated (%) but each peak shows a monodispersity. Day 39 we observe almost the same size as the day 15 with one monodispersed peak. Day 60 (2 months) already the size did not had a significant change and had as well a good monodispersity by taking into account the values recorded for PDI. Bare TbNPs dispersed in water for two months and preserved in the fridge at 4°C show mainly a monodisperse behavior with the size in the nanometer range (≤ 100 nm) thus they can be used for different experimental purposes for this time being.

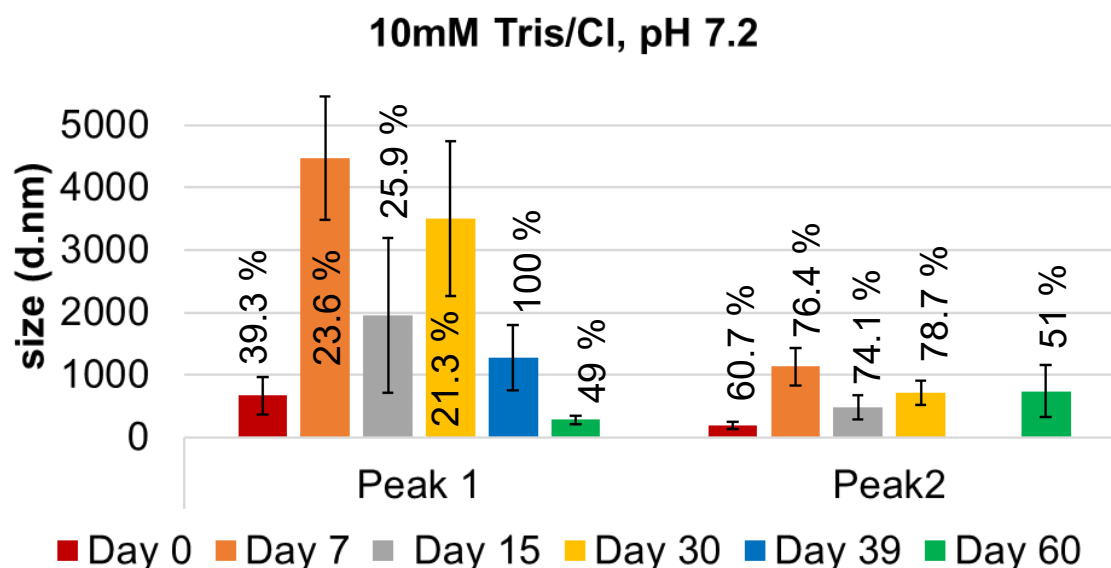


Figure 3.3.1.1B: DLS measurements at 25°C of bare TbNPs [8.5×10^{-9} M] over period of 60 days and at 10mM Tris/HCl, pH 7.2, performed in Malvern NanoZS instrument.

Bare TbNPs dispersed in 10mM Tris/HCl pH 7.2 (**Figure 3.3.1.1B**) showed a moderate and highly polydisperse behavior from the day 0 until day 60. These DLS measurements are associated with their percentages in order to show the population of nanoparticles distribution and homogeneity. We see that the nanoparticles that represent the highest percentage or saying it differently that represent the highest population have values in the range of $\sim 1 \mu\text{M}$. It seems that TbNPs preserve better their hydrodynamic radius in diH₂O rather than in 10mM Tris/HCl pH 7.2.

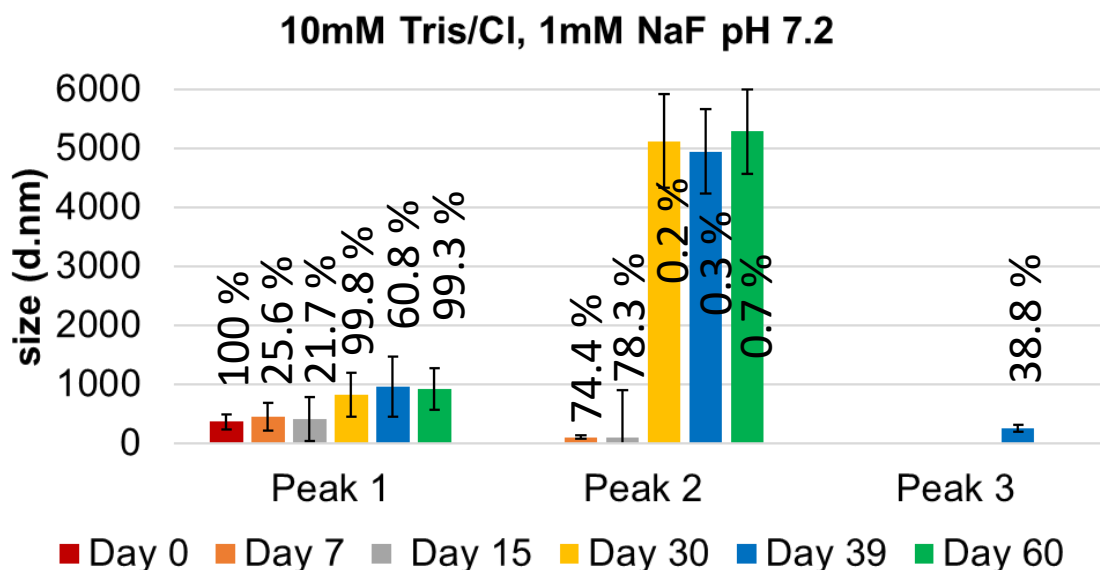


Figure 3.3.1.1C: DLS measurements at 25°C of bare TbNPs [8.5×10^{-9} M] over period of 60 days and at 10mM Tris/HCl, 1mM NaF pH 7.2, performed in Malvern NanoZS instrument.

We observed that bare TbNPs dispersed in 10mM Tris/HCl, 1mM NaF pH 7.2 demonstrated relatively smaller sizes than the bare TbNPs dispersed in 10mM Tris/HCl pH 7.2. Addition of sodium fluoride helps in decreasing the aggregation by avoiding the interactions of bare terbium nanoparticles between each other and keeping a relatively stable size for the period of two months with some heterogeneous populations (smaller population that does not even reach 1%) that have relatively large sizes. The behavior of NPs in this media varies from monodispersed (day 0) to moderate. From these results, we can clearly see that bare TbNPs dispersed in 10mM Tris/HCl, 1mM NaF pH 7.2 for the period of two months have sizes less than 1 μ m for the dominant population with highest percentage. Even though the size of bare TbNPs has a better preservation of hydrodynamic radius in Tris buffer with 1mM NaF, we cannot use this buffer for *in-situ* experiments. It was shown by the group of Doctor Machalinski that addition of NaF at 1mM concentration and higher induces early phases of cell apoptosis in human leukemic cells [80].

At this point, we need to find a buffer that will not cause such big agglomeration of NPs and is suitable (not harmful) when incubated with cells for *in-situ* experiments.

Parallel to DLS measurements, ZP measurements were performed and the results are depicted in (Table 3.3.1.2; Figure 3.3.1.2).

Table 3.3.1.2

| Day | diH ₂ O | 10mM Tris/Cl, pH 7.0 | 10mM Tris/Cl, 1mM NaF pH 7.0 |
|-----|--------------------|----------------------|------------------------------|
| | Zeta (mV) | Zeta (mV) | Zeta (mV) |
| 0 | 36.2 ± 7.6 | 14.4 ± 3.3 | 23.7 ± 3.3 |
| 7 | 41 ± 4.7 | 14.9 ± 2.8 | 22 ± 3.6 |
| 15 | 28.4 ± 9.8 | 11 ± 2.5 | 21.7 ± 3.4 |
| 30 | 25.8 ± 6.9 | 13.6 ± 3.1 | 19.1 ± 2.9 |
| 39 | 15.8 ± 4.9 | 14.1 ± 3.0 | 15.4 ± 3.4 |
| 60 | 12.3 ± 3.6 | -1.89 ± 3.7 | -14.1 ± 2.9 |

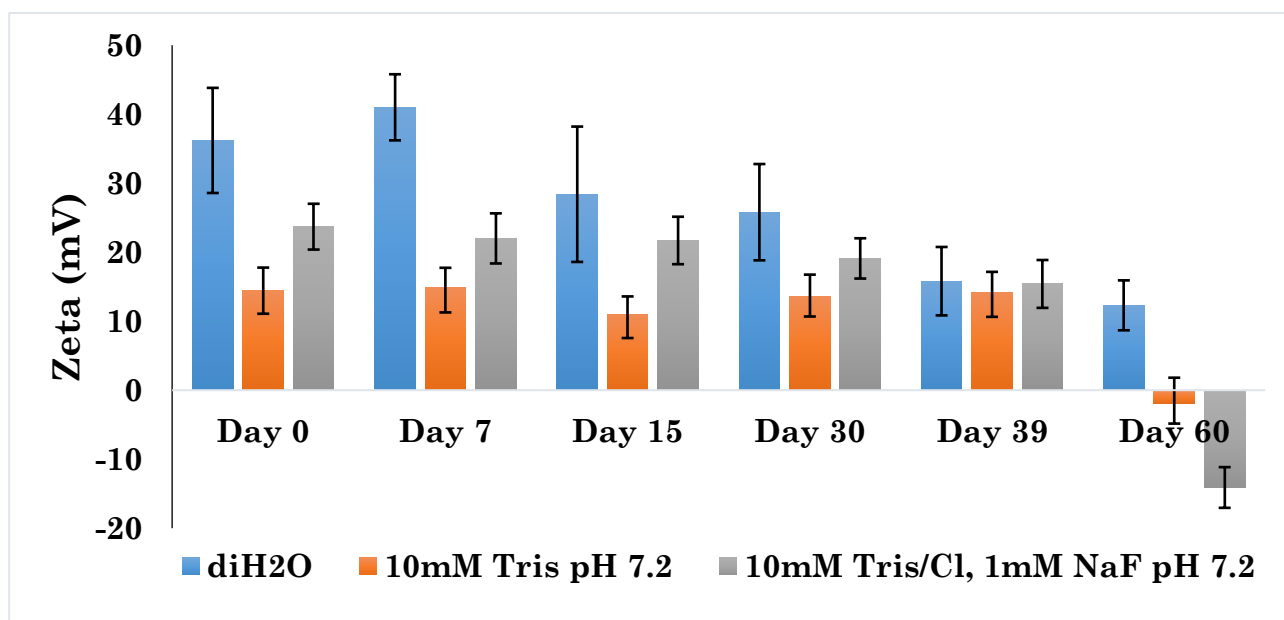


Figure 3.3.1.2: ZP measurements at 25°C of bare TbNPs [8.5×10^{-9} M] over a period of 60 days and at three different buffers (diH₂O; 10mM Tris/HCl, pH 7.2; 10mM Tris/HCl, 1mM NaF pH 7.2), performed in Malvern NanoZS instrument.

The main factors influencing ZP are pH, ionic strength and the concentration. pH is known as the most influential parameter in aqueous dispersions. The values of ZP goes from positive to negative from acidic to basic pH, respectively. Colloids lose stability when the pH is close to isoelectric point (the pH where the ZP becomes zero). The second most important factor is the ionic strength and valence of the ions. There is a proportional relation between ionic strength and ZP. By increasing the ionic strength, the adsorbed double layer (EDL) will be more compressed so the ZP will decrease and

vice versa. Ions with higher valence will have a more compact EDL and the ZP will decrease in magnitude. Zwitterions do not contribute to the ionic strength of a solution[81]. A third complex factor is the concentration. ZP increases with the concentration. Nevertheless, at high concentrated solutions, a thickness of EDL dominates and then ZP will decrease. In our case, the experiment was performed at constant concentration of TbNPs [8.5×10^{-9} M] thus, we cannot conclude about the effect that concentration will have on the values of ZP. A major difference between (diH₂O and 10mM Tris/HCl, pH 7.2; 10mM Tris/HCl, 1mM NaF pH 7.2) is the pH. Since diH₂O has an acidic pH and Tris/Cl has a neutral pH, taking note that ZP is positive at acidic pH and negative at basic pH that can be a reason that the values of ZP at diH₂O are higher (positive) and demonstrate a high stability.

The ZP values obtained from two months experiments (**Table 3.3.1.2 and Figure 3.3.1.2**) fall into the big picture described in literature of highly unstable (\pm 0-10mV), relatively stable (\pm 10-20mV), moderately stable (\pm 20-30mV) and highly stable ($> \pm$ 30mV). Unfortunately, the reality is more complex than that, but at least it provides indications on NPs stability. It is possible that a solution may have a low ZP but they are still stable. This is because ZP only provides information on the electrostatic repulsive forces but not on the van der Waals attractive forces. Steric interactions contribute also to colloid stability, for instance PEGylating facilitate stability of NPs while decreasing the ZP[72, 77].

From the experiments performed it is noteworthy that the ZP of NPs will decrease with time in all the three different buffers (diH₂O; 10mM Tris/HCl, pH 7.2; 10mM Tris/HCl, 1mM NaF pH 7.2), but for 10mM Tris/HCl, pH 7.2 and 10mM Tris/HCl, 1mM NaF pH 7.2 the charge will change from positive to negative. This may come due to the accumulation of F⁻ and OH⁻ ions on the slipping plane. Since the size increased with time, an aggregation of NPs may occur and the ZP decreases with time, the ions of the buffer that once served as a ‘barrier’ between bare TbNPs itself are losing this coordination by accumulating all on the surface of the slipping plane. Alternatively, another hypothesis is the leaking of the NPs and the fluoride ions (negatively charged) will give this negative value of ZP. I emphasize that TbNPs in diH₂O given the results

from zeta potential have high stability for about two weeks and on the period of two months; there is ~ 2.9 fold decrease in the charge stability by making it relatively stable. While for TbNPs in 10mM Tris/HCl, pH 7.2 the charge is almost constant categorizing it in the relatively stable group, but at the end of two months falls into the category of highly unstable. For TbNPs in 10mM Tris/HCl, 1mM NaF, pH 7.2 showed a moderately stable behavior, better than in 10mM Tris/HCl, pH 7.2 as expected.

3.3.2 pH influence on the size of TbNPs in diH₂O

Every aliquot of bare TbNPs was prepared at different pH by adding small amounts of NaOH/HCl to modify the pH. The concentration of TbNPs used in this experiment is $[1.70 \times 10^{-7} \text{ M}]$. Before DLS measurement, the samples were sonicated for 30 minutes at 25°C. The experiment data are presented in **(Table 3.3.2.1 and Figure 3.3.2.1)**. From this experiment, we wanted to observe the influence of pH on aggregation. We observed a size stability of TbNPs from acidic to basic pH in diH₂O. There is a small increase on the size at pH 8.0 but not significant. The PDI indicates a highly monodisperse solution and the percentage number gives the indication of one peak being present (one population of NPs) in the solution.

Table 3.3.2.1

| pH | 4.0 | 5.0 | 6.0 | 7.0 | 8.0 |
|-------------|-------------------|-------------------|-------------------|-------------------|-------------------|
| Size (d.nm) | 68.96 \pm 12.03 | 71.47 \pm 33.74 | 66.04 \pm 11.84 | 65.45 \pm 11.26 | 93.16 \pm 17.11 |
| % Number | 100 | 100 | 100 | 100 | 100 |
| PDL | 0.13 | 0.14 | 0.13 | 0.16 | 0.14 |

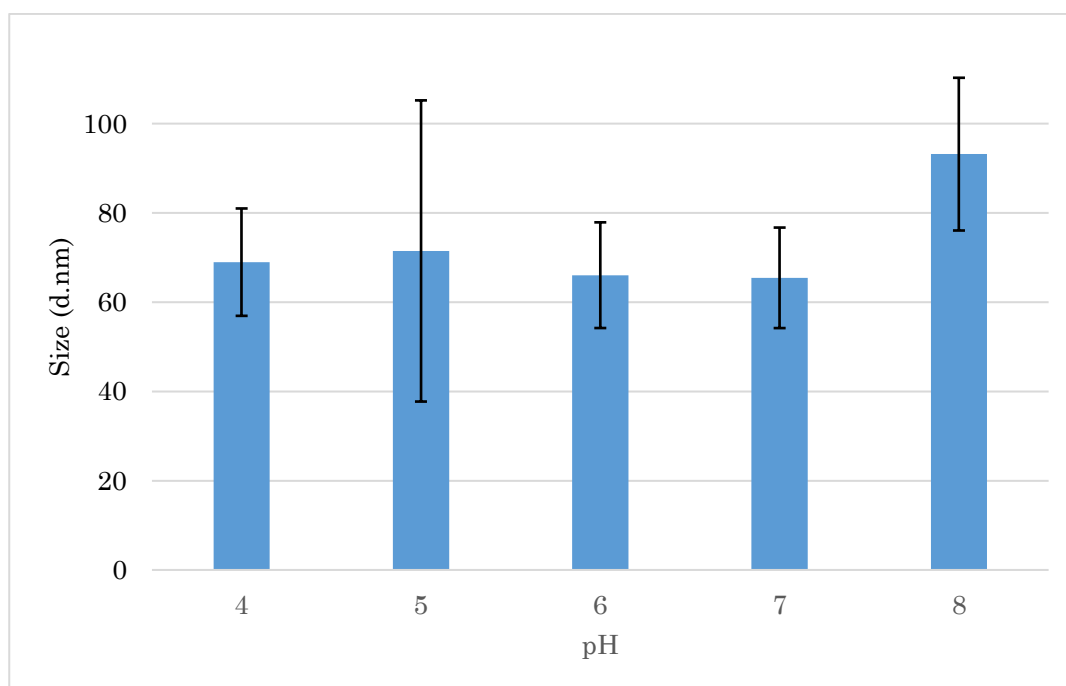


Figure 3.3.2.1: DLS measurements of bare TbNPs [1.70×10^{-7} M] in diH_2O at 25°C , from pH 4.0 to 8.0, experiment performed in Malvern NanoZS instrument

3.3.3 Effect of sonication on bare TbNPs as a function of time

To sonicate the samples we used an ultrasonic cleaner (USC-THD) purchased from VWR®. During the sonication, the temperature is monitored to be between $20\text{-}25^\circ\text{C}$ by continuously adding ice. The concentration of bare TbNPs was [$2.95 \times 10^{-9}\text{M}$]. We used sonication for evenly dispersing nanoparticles in their associated buffers. From the first study we observed that bare TbNPs at buffers such as (10mM Tris/HCl, pH 7.2; 10mM Tris/HCl, 1mM NaF pH 7.2) formed aggregates or micro-sized colloidal even though they were sonicated for 1h. So we decided to test a new buffer (10mM HEPES, pH 7.0) that showed less clustering effect on NPs and observe the effect of sonication on the particle size in this particular buffer as a function of time. The temperature was carefully monitored to be around ($20\text{-}25^\circ\text{C}$) during sonication since this effect will release heat and the temperature in the water will increase with time, and then we do not know the effect that temperature will have on the size of NPs. The variation of the particle size has been analyzed by DLS (at 25°C). The results presented in **(Table 3.3.3.1 and Figure 3.3.3.1)**, showed that TbNPs in 10mM HEPES pH 7.0 without sonication will

have a tendency to form some sort of aggregation. We observed two different populations, but the dominant one is (117.5 ± 117.5 nm with 86%) over the population of (526.4 ± 151.7 nm with 14%), which means that the majority of particles have a size 117.5 ± 117.5 nm. The PDI shows a value > 0.4 that clearly indicates a polydisperse solution of TNPs. This behavior of NPs may come due to their bare surfaces that will tend to agglomerate. After 1h sonication at (20-25°C) the size of TbNPs decreases significantly, it shows only one peak instead of two, but the PDI is > 0.4 , which according to the Sourav Bhattacharjee review[74] and the guidebook provided from Malvern Zetasizer[82], indicates a polydisperse solution. After sonication, we stored the NPs at 4°C and decided to measure the size after (30 min and 1 hour at 4°C). We observed an increase on the size of NPs with time. Sonication resulted in a decrease of the particle size of bare TbNPs dispersed in 10mM HEPES pH 7.0. We measure again the size of nanoparticles in the same solution that was stored for 30 minutes at 4°C and we observed that a slight aggregation was formed. We did the same experiment after 1h and again a slight aggregation is taking place. From these results, we can conclude that the sonication has an important effect in homogeneously dispersing the nanoparticles in HEPES buffer but its effect is transient with time and this means that we must perform the experiments immediately after sonication.

Table 3.3.3.1

| Bare TbNPs in 10mM HEPES, pH 7.0 | Peaks | size (d.nm) | % number | PDL |
|---|--------|-------------------|----------|------|
| no sonication | Peak 1 | 526.4 ± 151.7 | 14 | 0.57 |
| | Peak 2 | 117.5 ± 117.5 | 86 | |
| 1 h sonication | Peak 2 | 53.52 ± 25.63 | 100 | 0.42 |
| after sonication (stored 30 min @ 4°C) | Peak 2 | 187.9 ± 53.09 | 100 | 0.35 |
| after sonication (stored 1 h @ 4°C) | Peak 2 | 210.6 ± 41.72 | 100 | 0.4 |

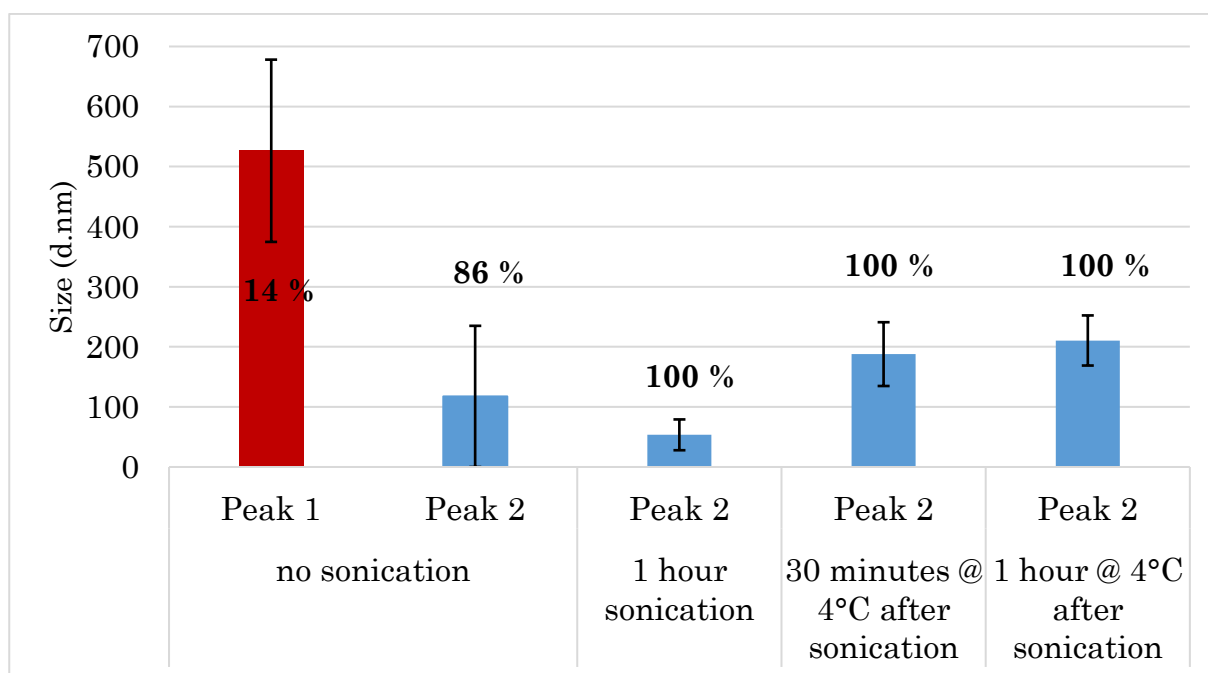


Figure 3.3.3.1: Effect of sonication on the size of TbNPs [$2.95 \times 10^{-9}M$] in 10mM HEPES pH 7.0, experiment performed in Malvern NanoZS instrument.

3.4 Conclusion

In this study were performed three different experiments with the purpose on understanding size and charge stability of bare TbNPs. The three parallel experiments performed are: i) influence of time and media on the size and charge of bare TbNPs (DLS and ZP) measurements; ii) influence of the pH on the size of bare TbNPs (in diH₂O) and iii) effect of sonication on the size of bare TbNPs (in 10mM HEPES pH 7.0) as a function of time, DLS measurements.

For the first experiment we observed that bare TbNPs dispersed in deionized water for two months and preserved in the fridge at 4°C showed mainly a monodisperse behavior with the size in the nanometer range (≤ 100 nm) thus they can be successfully used for different experiment purposes. The overall ZP was quite stable. TbNPs dispersed in 10mM Tris/HCl pH 7.2 showed a moderate and highly polydisperse behavior with size from 197.2 to 3502 nm, which makes this buffer not suitable for bare TbNPs preservation. TbNPs dispersed in 10mM Tris/HCl, 1mM NaF pH 7.2 demonstrated smaller sizes than the TbNPs dispersed in 10mM Tris/HCl pH 7.2 as expected from previous results. We observed as well a heterogeneous population of NPs (different

peaks with different sizes). The behavior of NPs in 10mM Tris/HCl, 1mM NaF pH 7.2 varies from monodispersed (day 0) to moderate. Even though in this buffer we observe a heterogeneous population of the bare TbNPs only less than 1% of the population showed sizes at the range of more than 1 μ m. Addition of sodium fluoride helps in decreasing the aggregation by avoiding the interactions of bare TbNPs between each other. The results from the ZP agreed with the results obtained from DLS for the three different media.

For the second experiment where we investigated, the influence of pH on the size of TbNPs dispersed in diH₂O was not significant, but the size was smaller at pH 6.0 and pH 7.0, which is rather a good sign for us since we perform experiments at pH 7.0.

For the third experiment where we investigated the effect of sonication on particle size we concluded that sonication helped in homogeneously dispersing the bare TbNPs in 10mM HEPES pH 7.0, but the effect of sonication on the particle size is only transient with time, which indicated that experiments should be performed immediately after sonication.

TbNPs in 10mM HEPES pH 7.0 had significantly smaller sizes than TbNPs in 10mM Tris/HCl, pH 7.2 or 10mM Tris/HCl, 1mM NaF pH 7.2, which is the reason that we chose to proceed further with the cell experiments by using HEPES instead of Tris/Cl buffer. From these experiments, we learnt more than we knew about our TbNPs and their performance in different buffers and pHs, but certainly more experiments need to be performed in the future.

4. Terbium nanoparticle biofunctionalization for extracellular biosensing

Vjona Cifliku, Cyrille Charpentier, Marcelina Cardoso Dos Santos, Laura Francès Soriano, Joan Goetz, Aline Nonat, Clémence Cheignon, Ka-Leung Wong, Loïc J. Charbonnière, and Niko Hildebrandt. Ultrabright terbium nanoparticles for FRET biosensing and in-situ imaging of epidermal growth factor receptors. (Chemistry 2020 Jun 5).

4.1 Introduction

The rapid development of clinical diagnostics and biomarker discovery have led to an increase demand for sensitive and specific analysis of large number of biomolecules on different cancer cell lines [83]. One of the first choices in the pool of probes for bioanalysis are luminescent nanoparticles (NPs)[13, 79]. Lanthanide (Ln) based NPs were shown to be particularly appealing for bioanalytical applications, displaying line like spectral emission signatures, very long excited state lifetimes, allowing for autofluorescence free TG detection, and emission throughout almost all the UV-Vis-NIR domain [85]. However the Laporte forbidden character of $f-f$ electronic transitions of Ln severely impact the absorption properties, and concomitantly their brightness[33]. To overcome this issue, the antenna effect, consisting in embedding Ln^{3+} cations in the cavity of photosensitizing ligands for Ln molecular complexes, was extended to Ln based NPs[86]. To address the challenge of biofunctional LnNPs in a most straightforward manner, the group of *Dr. Charbonnière et al.* synthesized and characterized ligands that can be used for both bioconjugation and photosensitization[13, 43]. Activated functional groups were used for covalent binding of the ligands to amine or sulfhydryl groups on biomolecules. These antenna-ligand-labelled biomolecules were then attached to Tb-doped LaF_3 NPs (TbNPs) via coordination between the chelating antenna functions of the ligand and Tb^{3+} ions on the TbNP surface. Thus, surface attachment of biomolecules directly resulted in photosensitization of the TbNPs, such that the biomolecules could “switch on” the TbNP PL and lead to ultra-bright luminescent TbNPs for specific biological recognition, **Figure 4.1.1**.

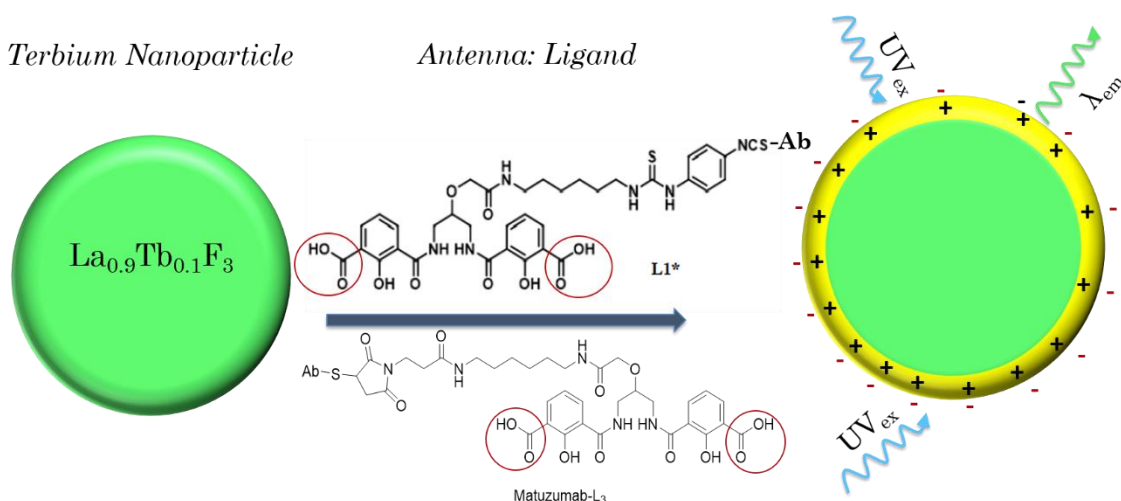


Figure 4.1.1: Principle of bio functionalized ultra-bright Ln nanoparticles. Without antenna-ligand-functionalized biomolecules (in this case antibodies - Ab), TbNPs do not emit significant PL upon UV excitation (left). Efficient coordination of the AB-ligand conjugates to Ln^{3+} ions on the TbNP surface leads to bright-photosensitized Tb PL and biofunctional NP surfaces.

To demonstrate the functionality of the TbNP-bioconjugates, we applied them to a prototypical biosensing approach that is the detection of EGFR [7, 26, 27]. The goal of this approach is the visualization of EGFR expression and internalization by different cell lines with TG PL microscopy. The high interest about EGFR comes from its significant role in the alteration of a variety of human malignancy. ErbB family receptors, but mainly in particular EGFR have been found to be present and even more overexpressed in the immortalization of several solid tumour's such as non-small cell lung cancer, head and neck cancers, breast, gastric, prostate etc [7, 22]. The over-activation of EGFR converts normal cells to malignant by fuelling the cells with sustained signals for proliferation, anti-apoptosis, angiogenesis and metastasis[22]. The conventional monoclonal antibody (mAb) has been the most popular molecule used in clinical trials directed against the ligand-binding domain of the receptor[87]. Matuzumab is a humanized monoclonal antibody that binds selectively to EGFR and inhibits ligand-mediated binding[88]. In this study was accomplished *in-cellulo* detection of ligand-receptor binding on cells with TbNP-antibody (Matuzumab) conjugates that could specifically bind to transmembrane EGFR. High specificity and sensitivity were shown by TG imaging of EGFR on both strongly (A431)[8] and weakly

(HeLa[89] and Cos7[11]) EGFR-expressing cell lines, whereas non-expressing cell lines (NIH3T3)[90] and EGFR-passivated A431 cells did not show any signals. Despite the relatively large size of TbNP-antibody conjugates, they could be internalized by A431 cells upon binding to extracellular EGFR, which showed their potential as bright and stable luminescence markers for intracellular signaling[86, 87]. To localize the TbNP-AB conjugates on the cell envelope (A431 cell line), we used co-staining with the plasma membrane marker MemBright-640 (MB-640)[93]. Several PL images were acquired at different heights of the cells (so called “z-stacking” from the ventral (bottom) to the dorsal (top) plasma membrane with z -steps of 0.22 μm . Careful PL analysis showed that TbNP-bioconjugates could be efficiently implemented into real bioimaging applications.

4.2 Materials and methods

4.2.1 Materials

$\text{La}_{0.9}\text{Tb}_{0.1}\text{F}_3$ NPs, L_1^* isothiocyanate ligand and L_2^* maleimide ligand⁶ with a chemical formula of $[(\text{C}_{35}\text{H}_{36}\text{N}_6\text{O}_{10}\text{S}_2)]$, (MW = 766.84 g/mol); $(\text{C}_{34}\text{H}_{39}\text{N}_5\text{O}_{13})$, (MW = 725.71 g/mol)], respectively together with the L_{CN} ligand were kindly provided from the group of Dr. Charbonnière, research director and our collaborator in the ‘neutrino’ project at Institut Pluridisciplinaire Hubert Curien (IPHC)/CNRS, Strasbourg. Merck Serono provided Matuzumab antibody (IgG against EGFR). Human epidermoid carcinoma (A431) cells were a kind gift from Dr. Christophe Le Clainche, research director at Institut de Biologie Intégrative de la Cellule (I2BC)/CNRS, Gif sur Yvette. NIH3T3 mouse embryonic fibroblast cells were a kind gift from Dr. Laure Bidou, maître de conference at Institut de Biologie Intégrative de la Cellule (I2BC)/Orsay. COS-7 monkey fibroblast and HeLa cervical cancer cells were purchased from American Type Culture Collection (ATCC) Company. Plasma membrane marker MemBright-640 (MB-640) was a kind gift from Dr. Andrey Klymchenko, research director at Laboratoire de Biophotonique et Pharmacologie (LBP)/Strasbourg. Cell view Petri dish with a borosilicate bottom ($175\mu\text{m} \pm 15\mu\text{m}$), Hank’s balanced salt solution (HBSS), HEPES (4-(2-hydroxyethyl)-1-

⁶ L_1^* and L_2^* for the activated ligand (often referred to with an asterisk)

piperazineethanesulfonic acid), and phosphate-buffered saline (PBS) were purchased from ThermoFisher Scientific. Reduced serum media (Opti-MEM), Dulbecco's modified eagle medium (DMEM), fetal bovine serum (FBS), Penicillin-Streptomycin (Pen-Strep), and L-glutamine were purchased from Sigma-Aldrich. Trizma® hydrochloride (Tris-HCl), hydrochloric acid (HCl), sodium hydroxide (NaOH), Tris (2-carboxyethyl) phosphine hydrochloride (TCEP), and dimethyl sulfoxide (DMSO) were purchased from Sigma-Aldrich. Sodium chloride (NaCl), was purchased from Duchefa. All chemicals were used as received. Deionized water (diH₂O) was obtained in the lab from the machines purchased at ELGA LabWater.

4.2.2 Characterization of bare TbNPs by transmission electron microscopy

The copper grid was ionized with a 15 mA plasma, to make the surface hydrophilic. 5µL of bare TbNP solution was added on the top of the copper grid and dried with a filter after 30 seconds. A 120kV electron cryo-microscope (Tecnai FEI) was used which has a LaB6 filament and equipped with a K2 basic camera (Gatan) and a cooled object holder (Gatan 626). Images were processed and analysed with ImageJ and graphs with Origin Lab. This work was benefited from the CryoEM platform of I2BC, supported by the French Infrastructure for Integrated Structural biology (FRISBI) [ANR-10-INSB-05-05].

4.2.3 Labeling of Matuzumab antibody with L₂* maleimide ligand

Matuzumab antibody (IgG against EGFR was provided by Merck Serono) was diluted into a final concentration of 1.86mg/mL (12.4µM) in 10 mM HEPES at pH 7.0. A volume of 2µL (~10 molar equivalents) of TCEP (Tris (2-carboxyethyl) phosphine hydrochloride) were added in the solution in order to break down the disulphide bonds, this solution was then incubated at 25°C for 1 hour in the dark at 400 rpm, mild shaking. L₂* maleimide ligand was used for antibody conjugation. L₂* maleimide ligand was dissolved at 5mM in DMSO (dimethyl sulfoxide) and a volume of 10.75µL (in concentration excess,

~20 molar equivalents) was mixed with the antibody sample in 10mM HEPES at pH 7.0. The mixtures were incubated for 2 h 30 min while rotating at 400 rpm, mild shaking at 25°C. For L₂-Ab⁷ conjugate purification, the sample was washed 6 times with 10mM HEPES pH 7.0 using 30 kDa MWCO Amicon Ultra-0.5-spin column and stored at 4°C. L₂* maleimide ligand concentration was determined by absorbance measurement at 316 nm using a molar absorptivity of 10,000 M⁻¹cm⁻¹. Antibody was quantified by absorbance measurement at 280 nm using a molar absorptivity of 210,000 M⁻¹cm⁻¹. The labeling ratios (~ 7 L₂ ligand per Antibody) were determined by linear combination of the respective absorbance values of L₂* maleimide ligand and antibody within the L₂-Ab conjugate absorbance. Final concentrations in the conjugates were (C_(L2) = 29.69μM and C_(Ab) = 4.29μM).

4.2.4 Labeling of L2-Ab conjugate with Terbium Nanoparticles

The conjugation of TbNPs with L₂-Ab conjugates was carried out on the same day as the imaging experiments. A volume of 12.35μL of TbNPs taken from the stock solution (170nM in diH₂O determined by ICP-AES) was mixed with 106μL of L₂-Ab [C_(L2) = 29.69μM and C_(Ab) = 4.29μM] in 144μL of HEPES buffer at pH 7.0 in order to obtain [TbNPs] = 8nM; [L₂] = 12μM; and [Ab] = 1.73μM. The mixture of L₂/Ab-TbNPs was then incubated in the dark for 2 hours at 25°C, 400 rpm with mild shaking. Due to strong L₂-Tb coordination, we did not perform separation experiments and named the final TbNP-AB stock solution after the AB per Tb ratio (214AB/TbNP). An aliquot of 250 μL of 214AB/TbNP were mixed with 750 μL of Opti-MEM ([TbNPs] = 2nM, [L₂] = 3μM, and [AB] = 0.43μM) prior incubation with cells.

4.2.5 Cell Culture

All cells (A431 human epidermoid carcinoma, NIH3T3 mouse embryonic fibroblast, COS-7 monkey fibroblast, and HeLa cervical cancer) were grown in Dulbecco's modified

⁷ L1 and L2 (without asterisk) for the one attached to the biomolecule because it lost its activated function.

eagle medium (DMEM), supplemented with 10% fetal bovine serum (FBS), 1% antibiotics (Pen-Strep), and 2 mM L-glutamine at 37 °C and 5% CO₂. The cells were passaged with trypsin-EDTA 0.05%.

4.2.6 Cell incubation with TbNP-AB conjugates

Cells were seeded at 5×10^4 cells/dish in a CELL view Petri dish with a borosilicate bottom ($175\mu\text{m} \pm 15\mu\text{m}$) and incubated at 37 °C and 5% CO₂ overnight. The following day, the cells were washed with Hank's balanced salt solution (HBSS). The solution of TbNP-AB was mixed rapidly with Opti-MEM and incubated for 30 minutes at 37 °C and 5% CO₂. After incubation, the cells were washed 3 times with phosphate-buffered saline (PBS) to rinse off any free TbNP-AB conjugates and 1.5mL of Opti-MEM solution was added to the cell dish for immediate observation under the microscope at 37 °C.

4.2.7 Co-staining TbNP-AB with MeM Bright-640 (MB-640)

MB-640 dye was used for plasma membrane labeling of A431 cells following 20 minutes of incubation at 37°C, 5% CO₂ with TbNPs at final concentration of 2nM diluted in Opti-MEM media. The cells were washed three times with HBSS. Then, a freshly prepared solution of MB-640 in HBSS was added at the final concentration of 20 nM without washing step and cells were imaged immediately.

4.2.8 Time-gated PL microscopy

Cell imaging was performed using a wide-field, inverted microscope (Olympus IX71), coupled with UV laser (349 nm, 200 Hz, Nd:YLF, Triton, Spectra-Physics) for pulsed excitation and an intensified CCD camera (ICCD, PI-MAX3, Princeton Instruments) for time-gated detection. Laser power was significantly reduced by using neutral density filters (ND Filter OD 0.5: NDUVO5B and OD 1: NDUV10B, Thorlabs). Laser irradiance on the sample was 160 mW/cm², which corresponds to a UV light dose of 2.8 $\mu\text{J}/\text{cm}^2$. The laser beam was redirected onto the sample with a 405 nm dichroic mirror (Di02-R405,

Semrock Inc.). PL signals of TbNPs were collected with a high numerical aperture (NA = 1.35) immersion oil objective (UPLSAPO 60 × O, Olympus) and detected using a 542 nm band-pass filter (FF01 542/20–25, Semrock Inc.). Acquisition settings in Winview software controlling the camera were fixed at a delay time of 10.88 μ s, gate width of 2 ms, gates/exposure of 1200 (for cell imaging), and intensifier gain of 100 V. DIC images were acquired with no delay time, a gate width of 300 ms, gates/exposure of 1, and an intensifier gain at 6 V. The background acquired on a bare substrate with the same acquisition settings (gating sequence, laser frequency) was subtracted from the raw images.

4.2.9 Z-stacking microscopy

A431 cells were incubated for 20 minutes (37°C, 5% CO₂) with 2 nM of TbNP-AB, then incubated with 20 nM of MemBright-640 (MB-640) plasma membrane marker, and then imaged immediately at room temperature. Fluorescence images were acquired on a wide-field inverted microscope Olympus IX83 using an X-Cite Exacte illumination source (Excelitas Technologies) and iXon Ultra 888 EMCCD camera (Andor). TbNPs were excited with 100 W illumination power and a 320 nm excitation filter (FF01–320/40–25, Semrock Inc.), a 495 nm dichroic mirror (FF495- Di03, Semrock Inc.), and a 542 nm emission filter (FF01–542/20–25, Semrock Inc.) were used for imaging. MB-640 was excited with 10 W illumination power and a 640 nm excitation filter (FF01–640/14–25, Semrock Inc.), 652 nm dichroic mirror (FF652/(25 × 36)-Di01, Semrock Inc.), and 676 nm emission filter (FF01–676/29–25, Semrock Inc.) were used for imaging. An UPLSAPO 60x objective (Olympus) was used for all images. Z-stack images were obtained using a translation stage (Prior Scientific Instruments Ltd) with 0.22 μ m step width. Images of TbNPs were acquired with x750 EM gain, 30 MHz readout speed, 1.1 μ s vertical shift speed, and x2 preamplifier sensitivity. Images of plasma membrane stained with MB-640 were acquired with the same parameters except EM gain at x2. iXon camera and Olympus microscope were controlled by Micromanager software 2.0-beta[94].

4.3 Results and Discussion

4.3.1 Characterization of TbNPs

TbNPs were synthesized according to previously published procedures[13] and their shape and composition were characterized by transmission electron microscopy (TEM, **Figure 4.3.1.1**), dynamic light scattering (DLS), zeta potential (ZP) and inductively coupled plasma mass spectrometry (ICP-MS) analysis. The concentration of the NPs was determined (following the previously published method[13]) using the average size of the NPs as determined by TEM measurement, the density of $\text{La}_{0.9}\text{Tb}_{0.1}\text{F}_3$ calculated as the percentage weighted density of LaF_3 and TbF_3 , and the total amount of La (or Tb) in the solution, as determined by ICP-MS analysis.

From transmission electron microscopy, we obtain information concerning the shape and the average size of inorganic core of NPs. The experiment was performed at the final concentration of 8.44×10^{-9} M of TbNPs in 10mM Tris/HCl pH 7.2. A histogram data analysis was performed in Origin software to obtain an information concerning the diameter of NPs. For image (**A**) the core diameter of $\text{La}_{0.9}\text{Tb}_{0.1}\text{F}_3$ NPs is 24 ± 11.1 nm, analysis performed on 157 NPs and for image (**B**) the core diameter is 22 ± 8.7 nm, analysis performed on 96 NPs. As well with a naked eye we observe a slightly trend of aggregation. This occurrence may come due to the drying process before imaging but also due to the naked surface of bare NPs. From the measurement of DLS and ZP of $\text{La}_{0.9}\text{Tb}_{0.1}\text{F}_3$ at final concentration of 2.11×10^{-8} M in diH_2O , we obtained a diameter of $(82.56 \pm 28.49 \text{ nm})$ and a charge of $(+17.3 \pm 3.42 \text{ mV})$.

Transmission electron microscopy of bare TbNPs

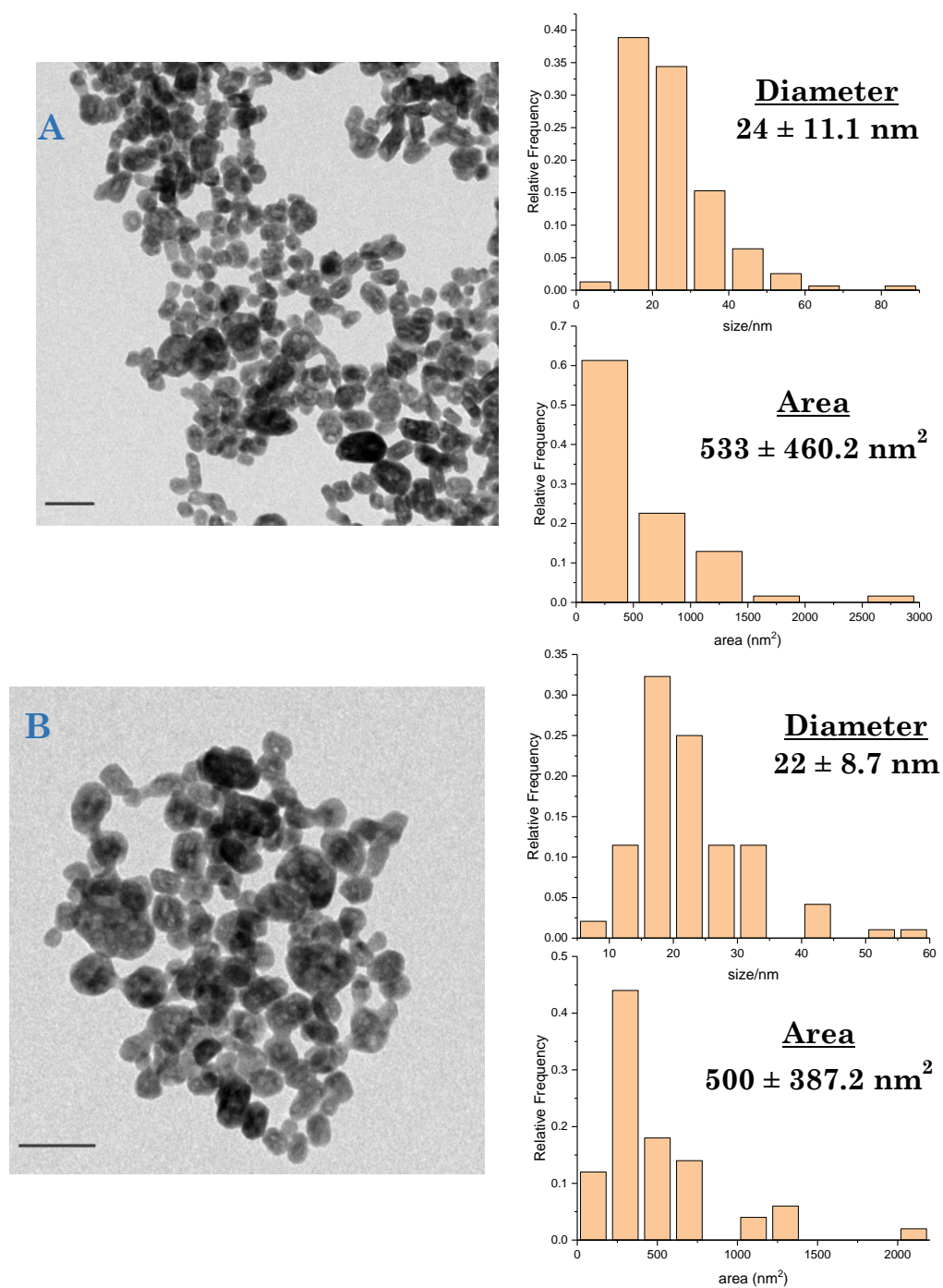


Figure 4.3.1.1: TEM images of the TbNPs [$8.44 \times 10^{-9} \text{ M}$] in 10mM Tris/HCl pH 7.2 (glow ionization, scale bar: 50nm, 15kX).

4.3.2 Fluorescence microscopy imaging of EGFR

The prototypical bioanalytical application consisted in the specific imaging of EGFR on cell membranes. Targeting EGFR and EGFR signalling are important for cancer research and many different cell lines have been investigated concerning their EGFR content and function[86, 90, 91]. Bright and non-photobleaching nanoprobe for specific imaging of single, multiple, or clustered receptors from the epidermal growth factor family of receptor tyrosine kinases (EGFR, HER2, HER3, HER4) have the potential to significantly advance such cancer-related studies[8]. One paramount requirement for a successful application of NP-based imaging agents is the functional conjugation with biological ligands (against the cell membrane receptor) that allow for specific targeting and the suppression of non-specific adsorption of the NPs to the cell, which often results in non-specific endocytosis of the NPs[14, 46]. We selected the AB Matuzumab[26, 27], which is not only a very specific ligand against EGFR but can also serve as a prototypical system for demonstrating functional TbNP-AB conjugation in general. Another important prerequisite is a good dispersion of the AB-conjugated NPs during incubation with cells, such that they do not interact with each other (formation of NP clusters) but can accomplish specific EGFR imaging without deposition of NP aggregates around or on the cell surface. Finally, a highly interesting photophysical property of our TbNPs is their long PL lifetime (millisecond range), which can be exploited in time-gated imaging to suppress all autofluorescence background (which is in the nanosecond range)[49, 92]. All time-gated images were taken on live cells and did not require delicate fixation protocols.

L₂-AB conjugates were prepared by coupling the maleimide-activated ligand L₂* to thiols (reduced cysteine's) on the AB and resulted in a labeling ratio of ~7 L₂ per AB to assure efficient attachment of the ABs to the TbNP surface. Absorption spectra were acquired using Lambda 35 UV/Vis spectrophotometer from PerkinElmer and PL spectra were acquired using a Xenius fluorescence spectrometer (SAFAS).

In **Figure 4.3.2.1** are shown the optical properties of L₂* maleimide ligand, L₂* maleimide ligand conjugated to antibody (matuzumab) and the PL emission spectrum of TbNPs.

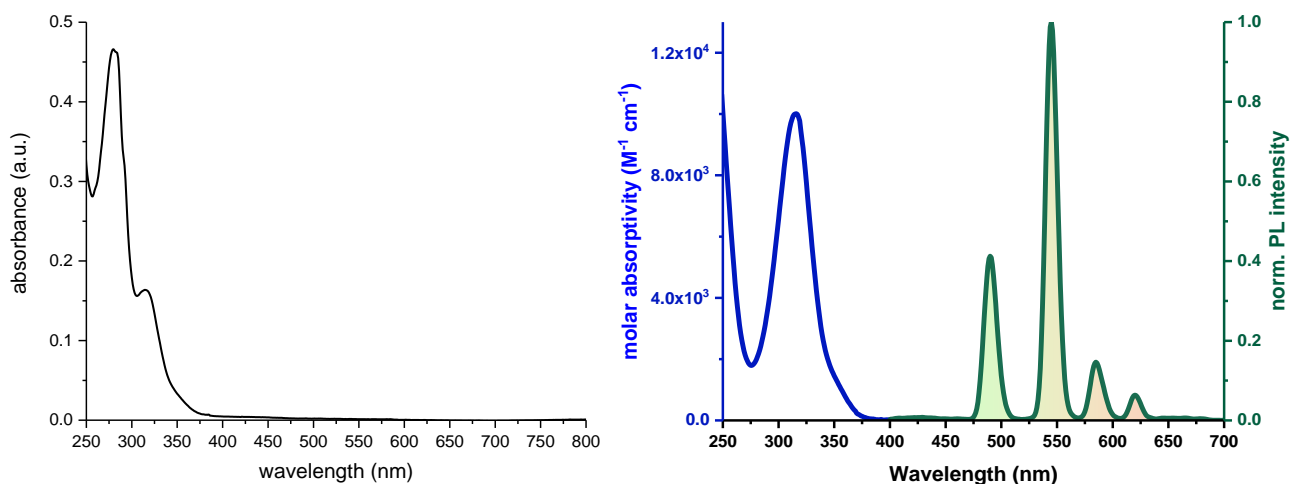


Figure 4.3.2.1: Optical properties of L_2^* maleimide ligand, L_2 -Ab and L_2 -TbNPs. Left: Absorption spectrum (black) of the conjugated L_2^* maleimide ligand with matuzumab antibody. Right: PL emission spectrum of L_2 -TbNPs (green) normalized to unity and molar absorptivity spectrum of L_2^* maleimide ligand (blue).

To investigate the influence of AB-conjugation conditions for optimized EGFR imaging performance, we prepared TbNP-AB conjugates with *i*) different amounts of L_2 -AB, *ii*) L_2 -AB and additional photosensitizing ligands (to entirely cover the TbNP surface with photosensitizing ligands), and *iii*) under different conjugation conditions (different conjugation buffers). TbNP-AB conjugates were prepared by simple mixture of L_2 -AB conjugates with TbNPs at ratios of *circa* 20, 100, and 200 ABs per TbNP. In initial titration experiments (addition of L_2 -AB to TbNPs), we could show that up to *circa* 200 L_2 -AB could be added to TbNPs to accomplish saturation of PL increase due to surface-attached photosensitizing ligands (**Figure 4.3.2.2**).

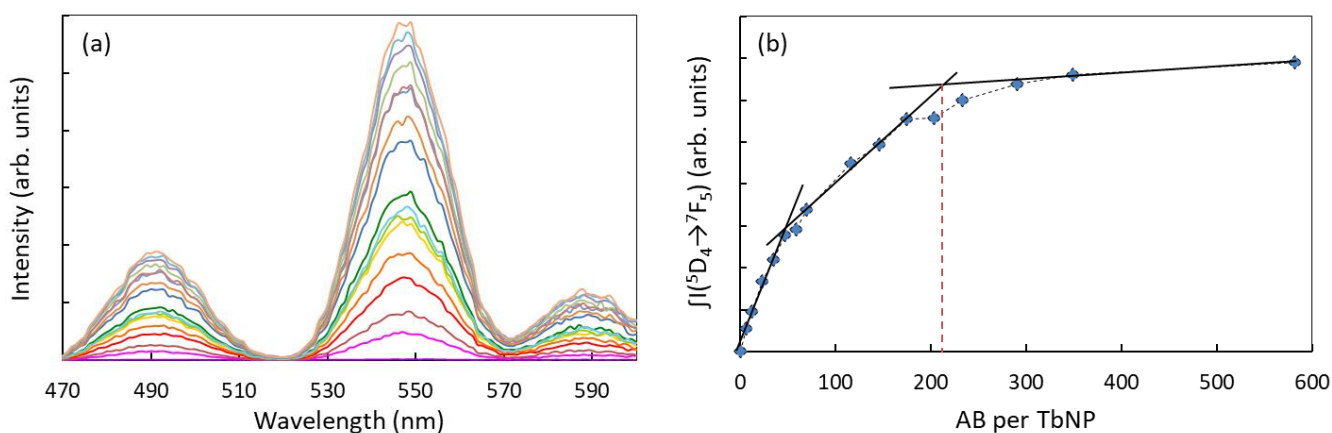


Figure 4.3.2.2: Spectrofluorometric titration of TbNPs by L_2 -AB. *a*) Evolution of the time-gated luminescence spectra ($\lambda_{exc} = 337$ nm) of a 0.8 nM solution of $La_{0.9}Tb_{0.1}F_3$ (Tris/HCl

0.01 M, pH = 7.0) upon addition of L₂-AB. (b) Evolution of the Tb centered emission intensity at 545 nm (⁵D₄ → ⁷F₅ transition) as a function of the [AB]/[NP] ratio. Dotted red line indicates the full coverage of the NPs corresponding to 214 AB/NP.

We therefore assumed that L₂-AB can efficiently bind to TbNPs until a maximum ratio of 200 and that this value corresponded to ~100 % surface coverage. Relatively high ratios of ABs per TbNP were used because previous experiments resulted in strong clustering of TbNP-AB conjugates at lower labeling ratios. For the 20AB/TbNP samples, we also added non-activated photosensitizing ligands (LCN) to investigate the influence of a complete coverage of the TbNP surface with photosensitizers on brightness and stability. While 20AB/TbNP and 100AB/TbNP samples were prepared in Tris buffer (10 mM, pH 7.2) to match the conditions of the in-solution FRET experiments performed from the group of Dr., Charbonnière, we used HEPES buffer (10 mM, pH 7.0) for the highest labeling ratio of 200AB/TbNP because we found that HEPES can improve labeling and imaging conditions[98].

To evaluate clustering of the different TbNP-AB conjugates, we first performed DLS measurements in solution (**Table 4.3.2.3, Figure 4.3.2.3**).

Table 4.3.2.3

| Nr of Ab/NP (% surface covered) | Peaks | Size (d.nm) | % Number | PDL |
|---|--------|-----------------|----------|------|
| 214 Ab/NP (100%) in 10mM HEPES, pH 7.0 | Peak 1 | 326.5 ± 192.1 | 100 | 0.24 |
| 107 Ab/NP (50%) in 10mM Tris/Cl, pH 7.2 | Peak 1 | 601.8 ± 192.7 | 98.4 | 0.43 |
| | Peak 2 | 5560 ± 8.60E-05 | 1.6 | 0.43 |
| 20Ab/NP (10%) in 10mM Tris/Cl, pH7.2 | Peak 1 | 972 ± 428.2 | 62.8 | 0.6 |
| | Peak 2 | 208.4 ± 69.55 | 21.4 | |
| | Peak 3 | 4855 ± 703.4 | 15.8 | |
| 20Ab/NP (10%) + LCN ligand (90%) in 10mM Tris/Cl, pH7.2 | Peak 1 | 937.1 ± 341.4 | 94.7 | 0.47 |
| | Peak 2 | 5501 ± 202.5 | 5.3 | |

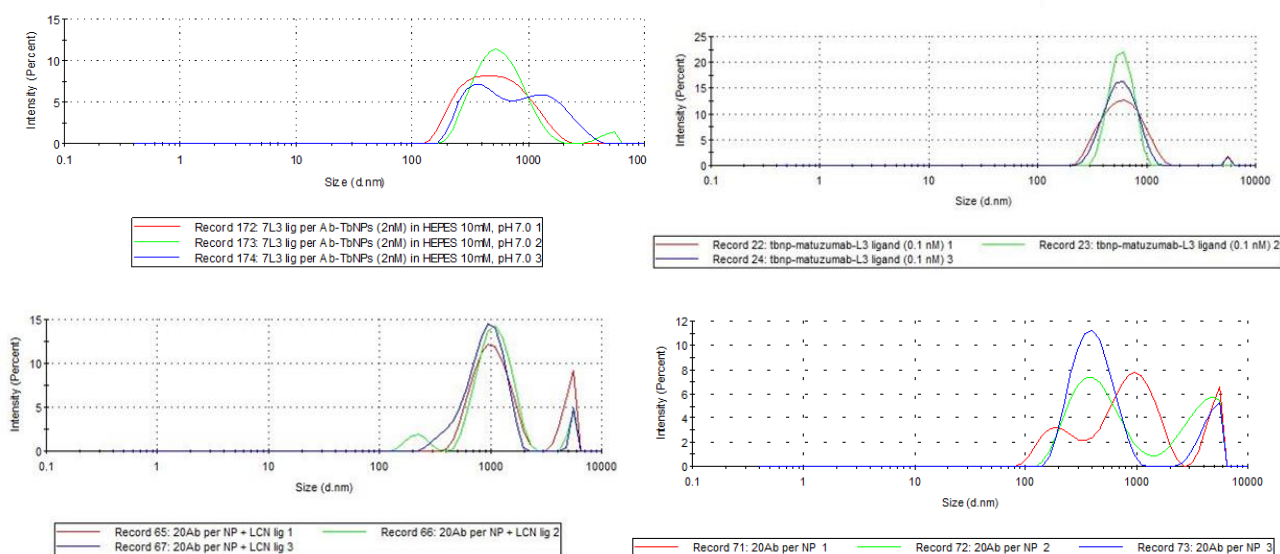
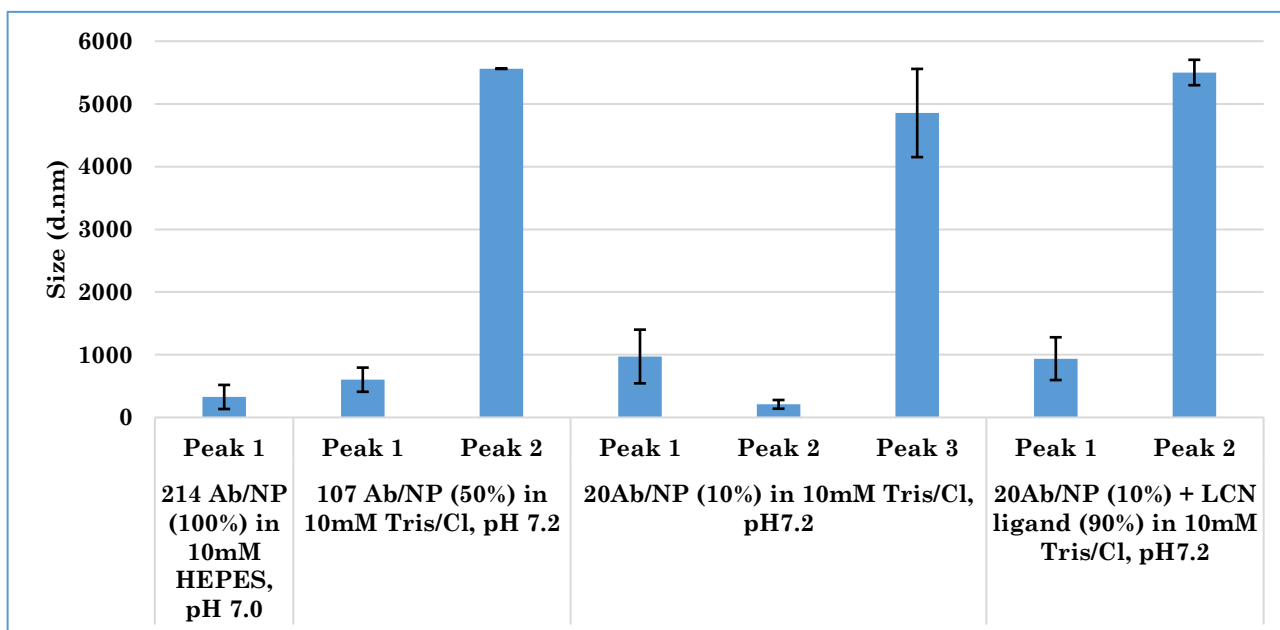


Figure 4.3.2.3: DLS measurements (raw data on the bottom) of the different AB-TbNP conjugates showed diameter peaks of different sizes.

These analyses showed that the hydrodynamic diameters of TbNP-AB conjugates became smaller for higher labeling ratios, that the 20AB/TbNP and 100AB/TbNP samples showed some clustering (additional species with very large hydrodynamic

diameters above 4 μm), and that the addition of non-conjugated ligands (20AB/TbNP+L_{CN}) could not significantly reduce clustering or the size of the main NP species. While the investigation of the hydrodynamic sizes in solution can provide a first good indication of the sample quality, investigation of the different TbNP-AB conjugates at actual imaging conditions are much more important for evaluating their imaging performance. We therefore used time-gated PL imaging of A431 cells incubated with the different TbNP-AB conjugates and performed a cluster analysis, which analyzed the intensities and areas of PL spots imaged on the cells. Transmission images in differential interference contrast (DIC) were simultaneously registered to show the cell surfaces and overlay them with TbNP PL signals, **Figure 4.3.2.4**.

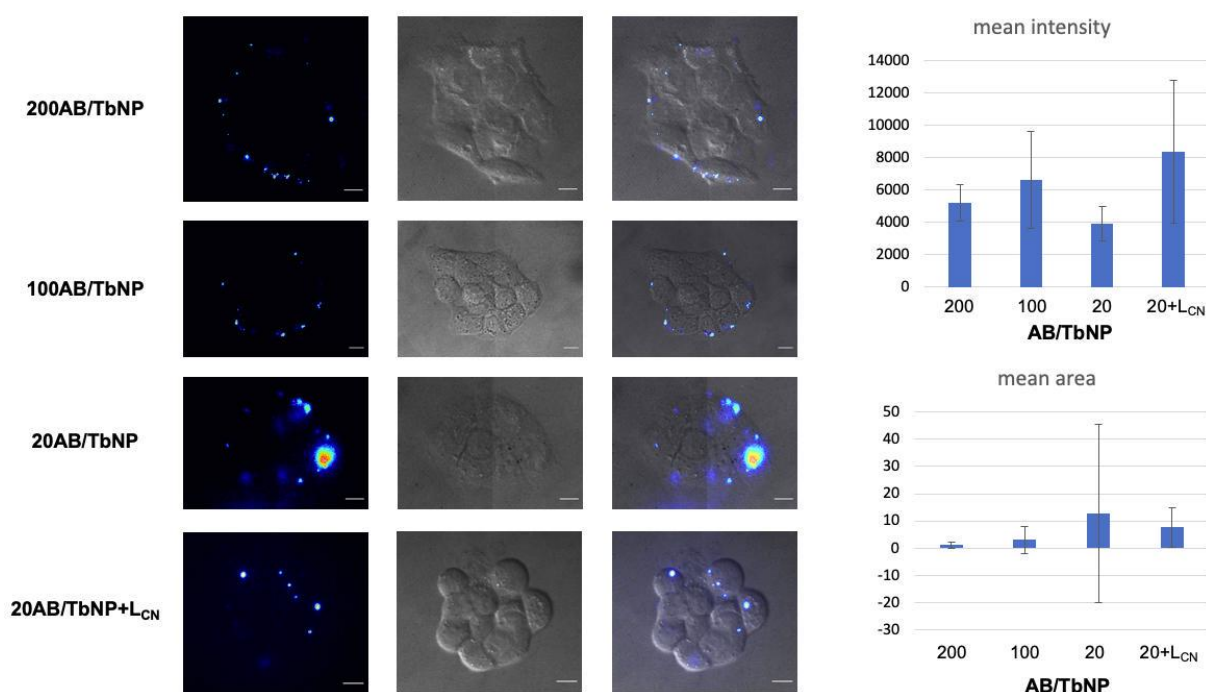


Figure 4.3.2.4: Time-gated PL imaging of A431 cells incubated with different TbNP-AB conjugates. The images on the left show PL images (left), for which the PL intensity of the luminescent areas is color coded from dark blue (low intensity) to red (high intensity), differential interference contrast (DIC) transmission images (center), and their overlay (right). Scale bars are 10 μM in length. The graphs on the right show the quantification of all emitting spots concerning the mean intensity (top) and the mean area (bottom).

These results showed clear evidence for strong clustering of the 20AB/TbNP samples on the cell surfaces. While the addition of L_{CN} resulted in higher PL intensities and reduced clustering (smaller areas of PL spots), significantly better results were accomplished for

the samples with higher labeling ratios. Previous studies showed that EGFR forms clusters of ~ 150 nm in diameter on HeLa cells and that EGFR on highly EGFR-overexpressing A431 cells results in even stronger clustering and favors the assembly of NPs into larger clusters[21, 93]. Thus, we also expected a clustered fluorescence EGFR staining pattern for higher AB/TbNP ratios but with significantly smaller clusters. Although the mean PL intensities reduced from 20AB/TbNP+ L_{CN} to 100AB/TbNP and 200AB/TbNP, the latter were still higher than for 20AB/TbNP and the mean areas of the PL spots were strongly reduced. Independent of the different performances, all three TbNP-AB conjugates could be used for imaging and were therefore investigated in more detail concerning specificity and sensitivity of EGFR detection with different cell lines. Because the 20AB/TbNP+ L_{CN} samples did not result in a strong performance improvement and the other three samples were better suited for a direct comparison, we did not further investigate the L_{CN} -containing conjugates. Taking into consideration *i)* the very similar brightness of 100AB/TbNP and 200AB/TbNP (~ 1.3 -fold higher intensity for 100AB/TbNP), *ii)* the smallest PL spot area (least clustering) for 200AB/TbNP (~ 2.7 -fold smaller than for 100AB/TbNP), *iii)* the lowest intensity and highest clustering for 20AB/TbNP, *iv)* the same buffers (Tris) for 20AB/TbNP and 100AB/TbNP, and *v)* the amount of available samples from the same batch, we investigated the following systems: *a)* 20AB/TbNP and 100AB/TbNP for investigating the possibility of detecting EGFR on cells with high (A431)[100] and low (HeLa and COS-7)[11, 84] EGFR expression and *b)* 200AB/TbNP for investigating sensitivity, specificity (A431 cells *vs* EGFR-passivated A431 and EGFR-deleted NIH3T3 cell lines), and endocytosis of EGFR-bound TbNP-AB conjugates.

Similar to non-targeted (pure TbNPs without bioconjugation) imaging[14], we required only low nanomolar concentrations of TbNP-AB conjugates to acquire sufficient PL signals for imaging EGFR on the cell membranes. A431, HeLa, and COS-7 cells were incubated for 30 minutes with 1 nM of 20AB/TbNP or 100AB/TbNP and imaged after carefully washing off TbNP-AB conjugates, **Figure 4.3.2.5**. Both TbNP-AB conjugates could image EGFR on A431 cells and, as expected, the 20AB/TbNP showed stronger clustering (several very large PL spots). For the lower EGFR-expressing HeLa and COS-7 cell lines, 20AB/TbNP signals were below the detection threshold and could not image

EGFR, whereas the better performance of 100AB/TbNP allowed for EGFR detection on the cells. For both cell lines, the 100AB/TbNP PL images showed less TbNP clusters (smaller PL spots compared to A431 images), which could be an indication of lower EGFR expression levels. While both TbNP-AB conjugates could be used for EGFR-targeted imaging, the results clearly showed the advantages of higher AB-conjugation ratios in terms of sensitivity and reduced NP clustering.

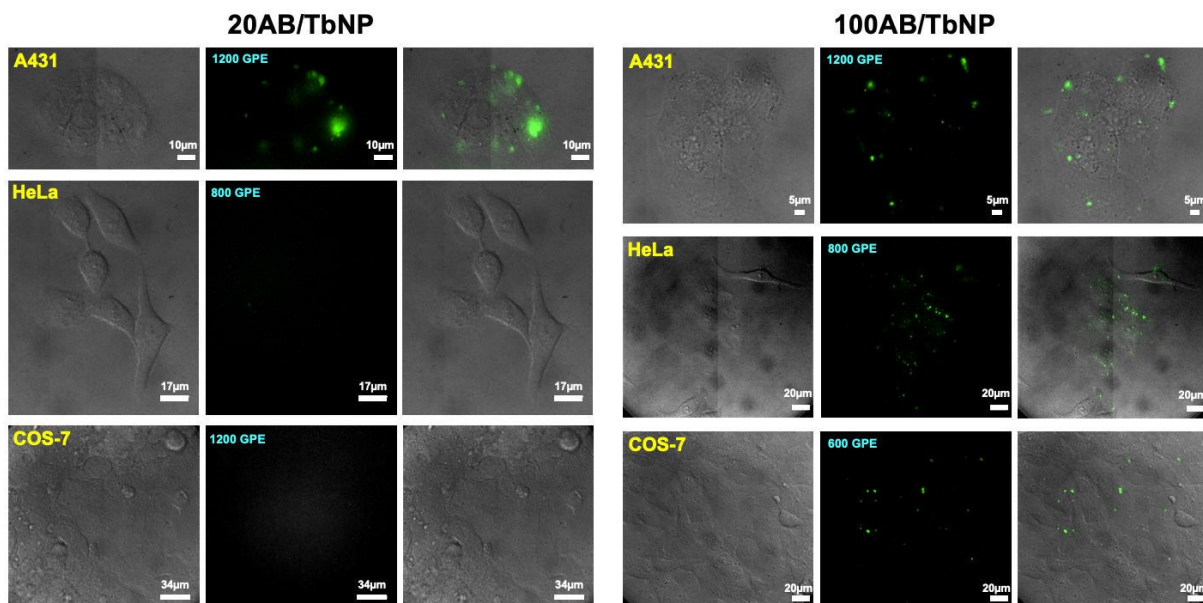


Figure 4.3.2.5: Time-gated PL imaging of EGFR on the membranes of A431, HeLa, and COS-7 cells. All cells were incubated with 1 nM of 20AB/TbNP (left) or 100AB/TbNP (right). Images show DIC transmission (left), time-gated PL (center), and their overlay (right). PL of TbNPs is shown in green. GPE: Gates per exposure.

Images for A431 EGFR imaging using 2 nM TbNPs are shown in **Figure 4.3.2.6**.

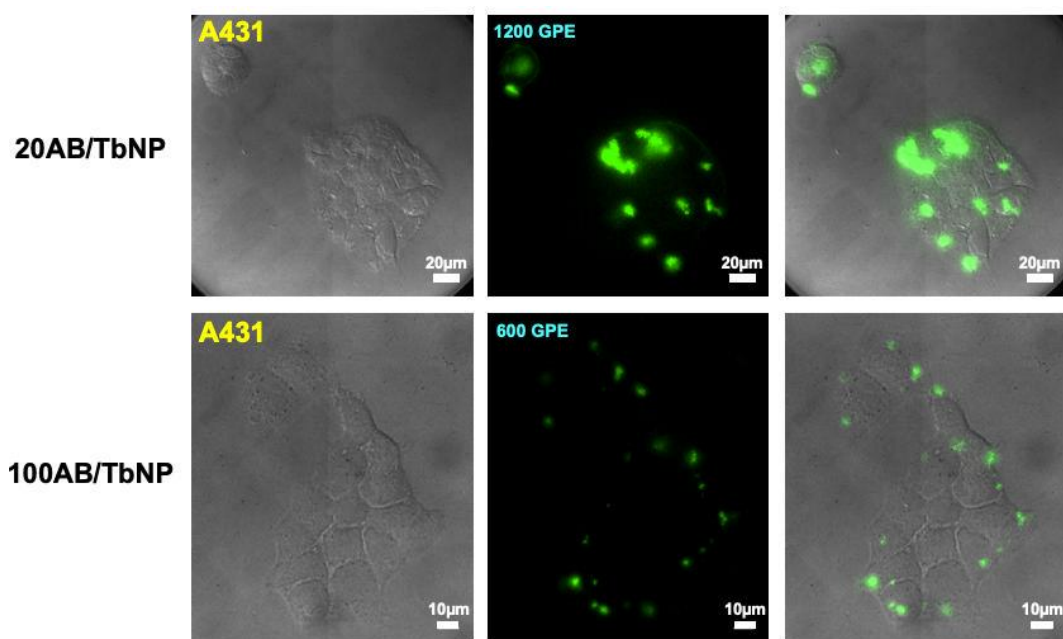


Figure 4.3.2.6: Time-gated PL imaging of EGFR on the membranes of A431 cells that were incubated with 2 nM of 20AB/TbNP (top) or 100AB/TbNP (bottom). Images show DIC (left), time-gated PL (center), and their overlay (right). PL of TbNPs is shown in green. GPE: Gates per exposure.

Below are shown additional images of 100AB/TbNP-based EGFR imaging on HeLa and COS-7 cells, **Figure 4.3.2.7**.

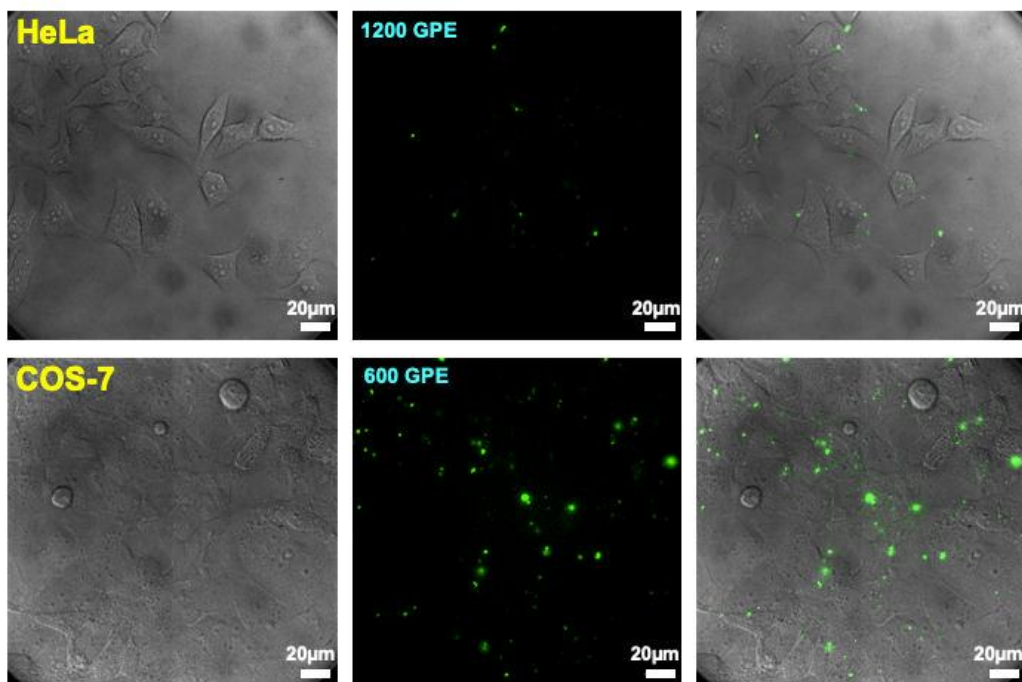


Figure 4.3.2.7: Time-gated PL imaging of EGFR on the membranes of HeLa and COS-7 cells incubated with 1 nM of 100AB/TbNP. Images show DIC (left), time-gated PL (center), and their overlay (right). PL of TbNPs is shown in green. GPE: Gates per exposure.

PL imaging of A431 cells with 200AB/TbNPs showed that different concentrations of the TbNP-AB conjugates resulted in different immunostaining patterns, **Figure 4.3.2.8 and Figure 4.3.2.9**. Although the signals were relatively weak, 0.5nM TbNPs could still image EGFR on the cell membranes with high specificity. Using the same TbNP concentrations on NIH3T3 cells that did not express EGFR or on A431 cells that were passivated with non-conjugated AB (to saturate EGFR binding sites on the cell membrane) did not result in any PL signals, **Figure 4.3.2.10**. At higher concentrations, the EGFR on the cell membranes became more visible. For 2nM of TbNP-AB conjugates almost the entire membrane could be stained, which showed the very high EGFR expression of A431 cells, **Figure 4.3.2.8 bottom**. These results demonstrated the importance of optimizing the AB-conjugation conditions and that a maximum coverage of AB on the TbNP surface leads to TbNP-AB conjugates that can be applied for bright and targeted EGFR imaging with stable lanthanide emitters.

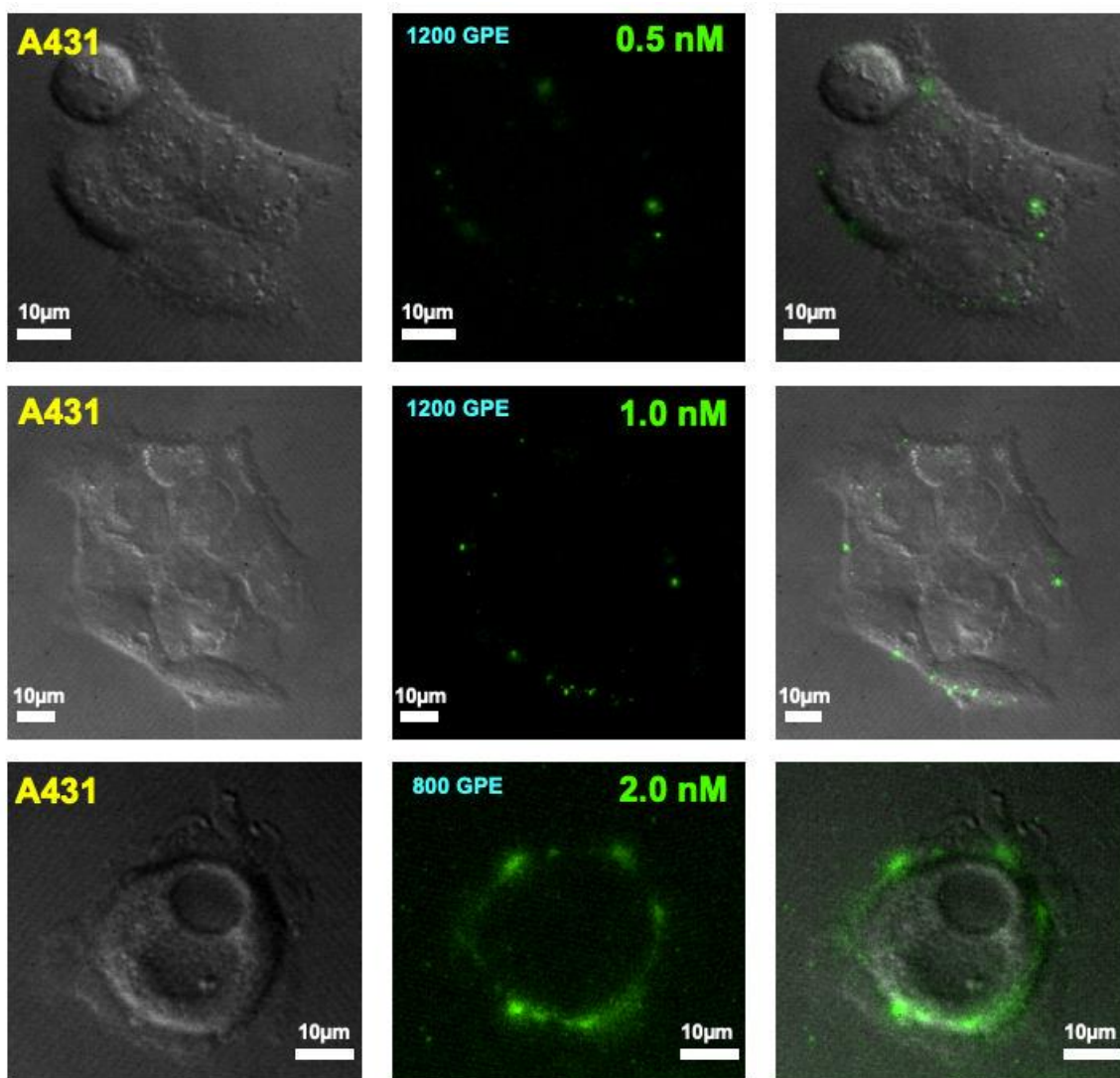


Figure 4.3.2.8: Time-gated PL imaging of EGFR on the membranes of A431 cells that were incubated for 30 minutes with different concentrations of 200AB/TbNP. The representative images show DIC transmission (left), time-gated PL (center), and their overlay (right). PL of TbNPs is shown in green. GPE: Gates per exposure.

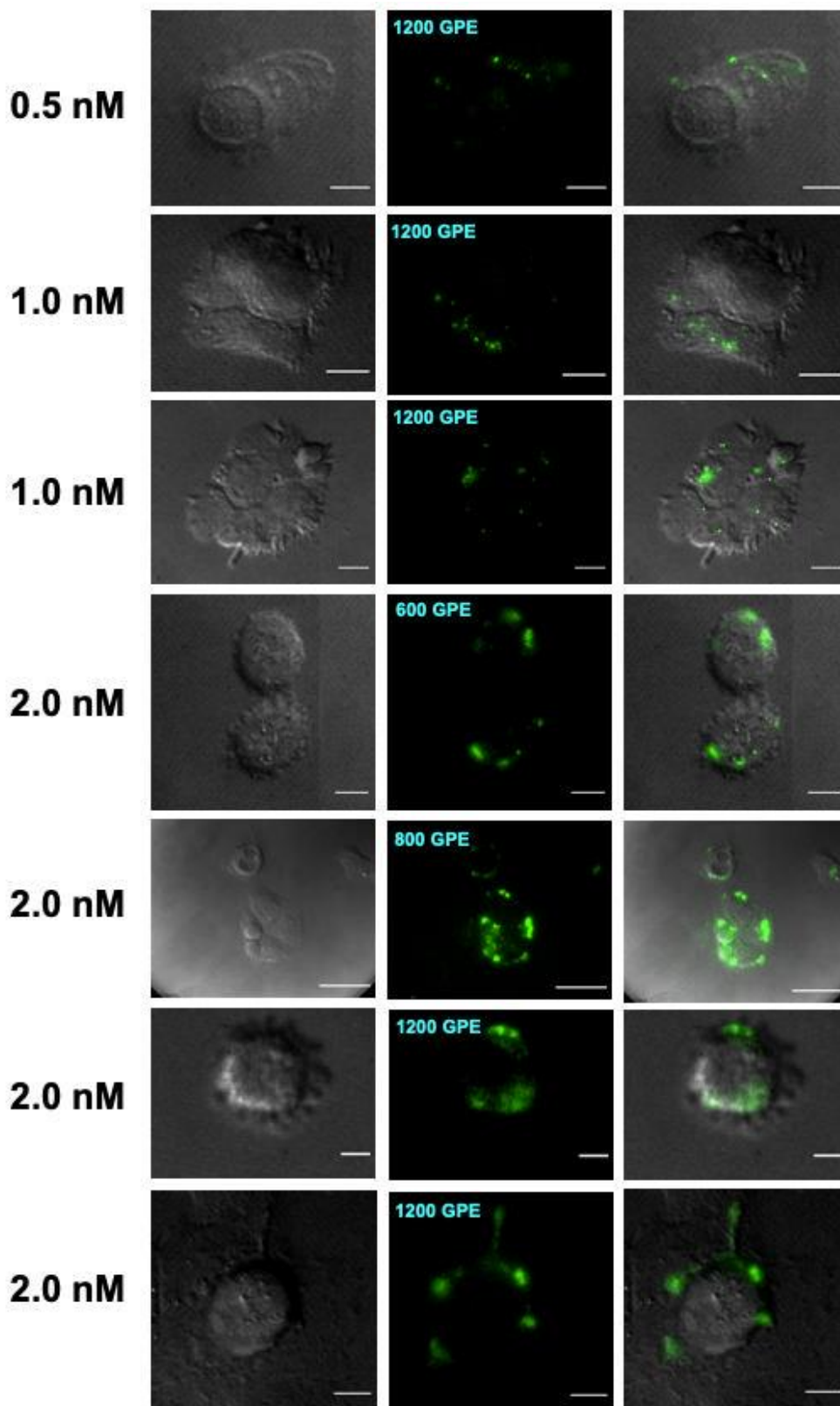


Figure 4.3.2.9: Time-gated PL imaging of EGFR on the membranes of A431 cells that were incubated for 30 minutes with different concentrations of 200AB/TbNP. The images show DIC transmission (left), time-gated PL (center), and their overlay (right). PL of TbNPs is shown in green. GPE: Gates per exposure. From top-bottom of the picture (0.5

nM - $2 nM$ with 600gpe) scale bar is $10 \mu m$. Image of $[TbNPs] = 2nM$, GPE 800, scale bar is $50\mu m$. The image below same concentration of TbNPs but with GPE 1200, scale bar is $5\mu m$. Last image at the bottom, has a scale bar of $10\mu m$.

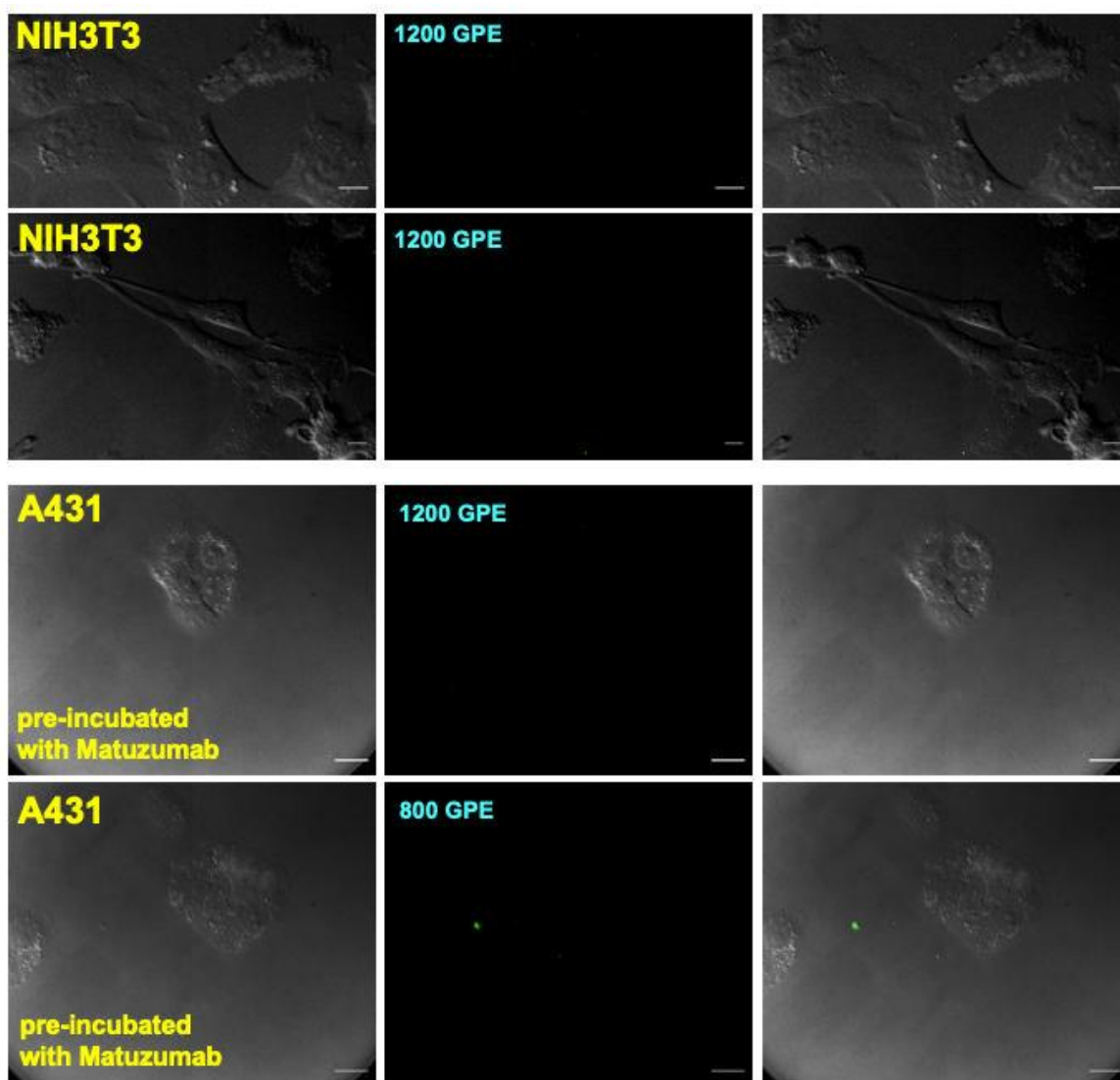


Figure 4.3.2.10: Time-gated PL imaging of NIH3T3 and A431 cells incubated with $0.5 nM$ of 200AB/TbNP. NIH3T3 does not express EGFR and EGFR expressed on A431 cells was passivated (prior to TbNP-AB incubation) with unconjugated AB. Therefore, TbNP-AB conjugates could not stain the cells and no PL is visible (on the bottom page there is one PL spot, which is outside of cells and caused by attachment to the cell view slide). Images show DIC (left), time-gated PL (center), and their overlay (right). PL of TbNPs is shown in green. GPE: Gates per exposure. Scale bar is $10\mu m$ for NIH3T3 and for A431 the scale bar is $20\mu m$.

Encouraged by the excellent EGFR imaging conditions, we aimed at investigating a possible cellular uptake (endocytosis) for intracellular trafficking of EGFR[87, 95]. To

localize the TbNP-AB conjugates on the cell envelope, we used co-staining with the plasma membrane marker MemBright-640 (MB-640)[93]. Several PL images were acquired at different heights of the cells (so called “z-stacking” from the ventral (bottom) to the dorsal (top) plasma membrane with z-steps of 0.22 μm). **Figure 4.3.2.11** shows representative sections of the z-stack with TbNP-AB inside the membrane, inside the cell, and outside the cell.

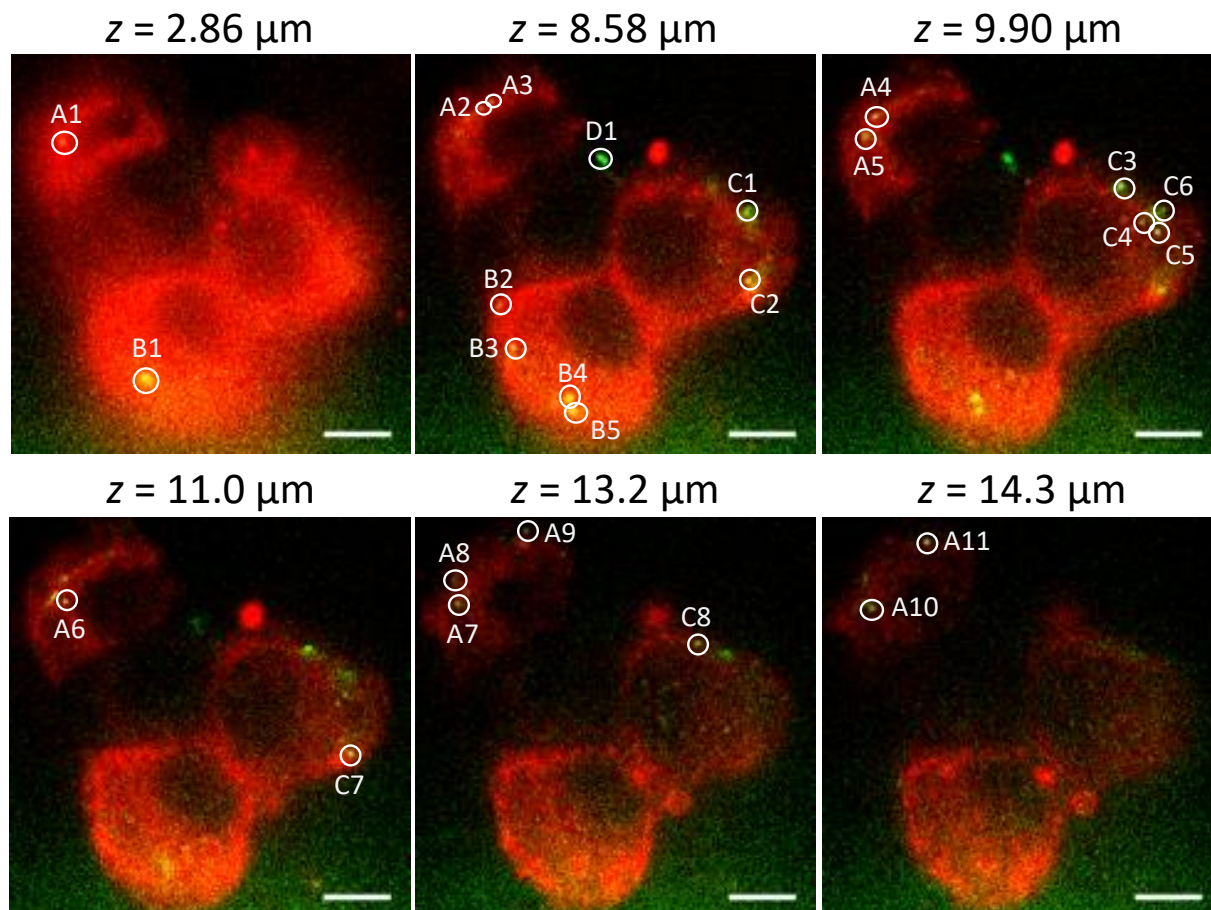


Figure 4.3.2.11: PL image sections taken at different heights (bottom: $z = 0$) of three representative cells (A, B, and C). The plasma membrane is coloured in red and TbNP-AB in green. Colocalization of membrane and TbNP-AB is represented in yellow. Numbered areas show TbNP-AB at different locations within the cells.

Deeper analysis of all the circled areas with lateral sections (xz and yz) are shown in **Figure 4.3.2.12**.

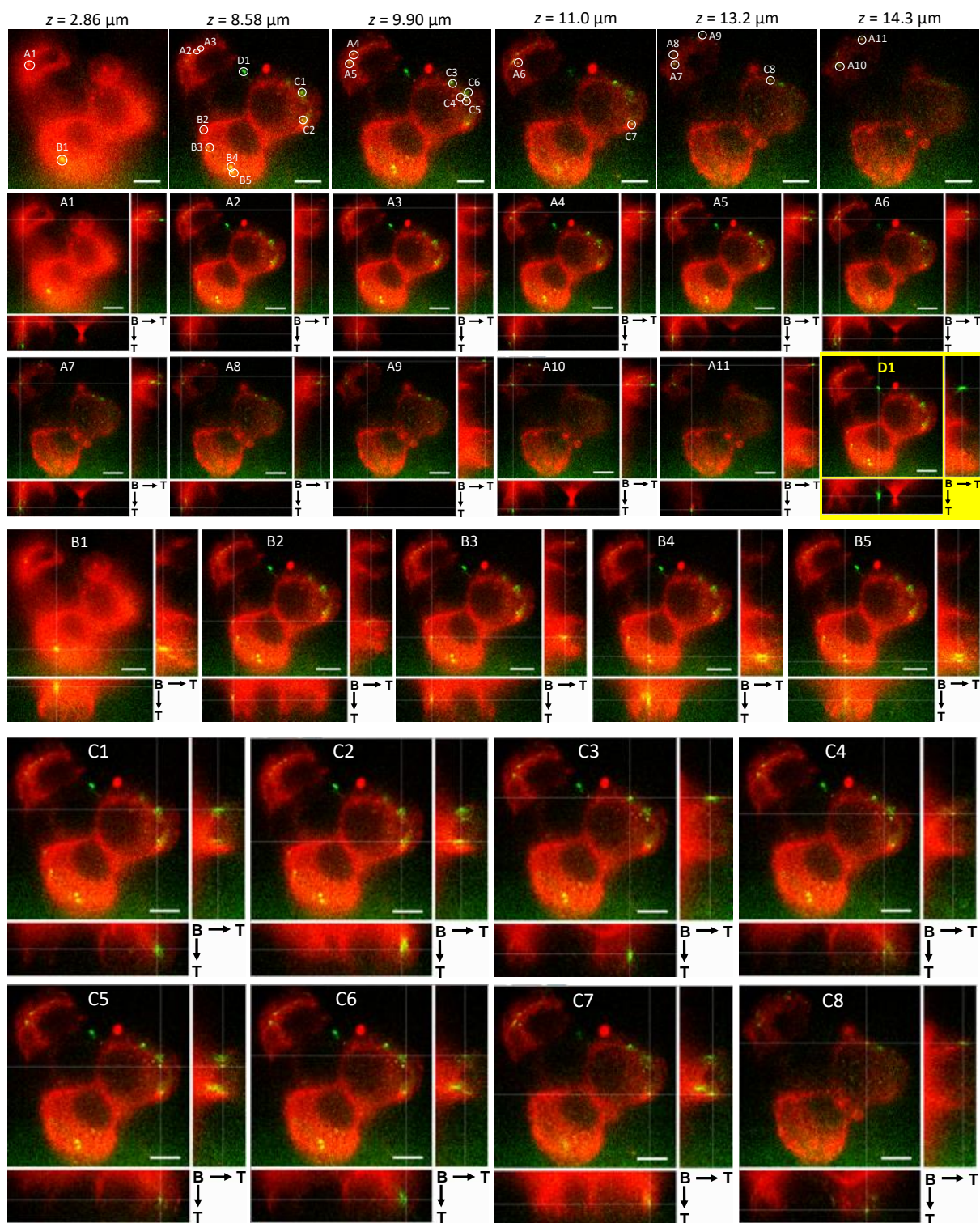


Figure 4.3.2.12: z-stack sections accompanied by lateral sections (xz below and yz right of each z-sections, B: bottom of the cell, T: top of the cell), which visualize the lateral locations of the TbNP-AB conjugates that were numbered in **Figure 4.3.2.11** (shown again on the top for clarity) respectively for cell A (A1-A11), cluster outside of the cell D (D1), cell B (B1-B5), and cell C (C1-C8). Horizontal/vertical white lines in the z-section images indicate the positions xy on the z-section and xz and yz on lateral sections. Scale bar: 10 μm .

In the lowest z-section image (**Figure 4.3.2.11** and **Figure 4.3.2.12**, $z = 2.86 \mu\text{m}$) the two yellow (colocalized TbNP-AB and MB-640 PL) points (A1 and B1) indicate that TbNP-AB are localized in the ventral membrane. In the second image (**Figure 4.3.2.11** and **Figure 4.3.2.12**, $z = 8.58 \mu\text{m}$) almost all TbNP-AB (with the exception of C1 and D1) are colocalized with the membrane (yellow spots). Taking into account that this section is close to the center of the cell, as also shown in lateral section, the TbNP-ABs are most probably localized in the side membranes of the cells. In contrast, C1 is not colocalized with the membrane (green), indicating that the TbNP-AB has not yet adhered to the plasma membrane. D1 (also green) is a cluster of TbNP-AB outside the cell (floating in the medium). Slightly above in the cells (**Figure 4.3.2.11** and **Figure 4.3.2.12**, $z = 9.90 \mu\text{m}$) TbNP-AB A4 and A5 (yellow) are probably colocalized with side membrane, C3 is outside the cell but close to the membrane (bound to extracellular EGFR) and C4, C5, and C6 appear to be inside the cell (internalized very recently and located just below the membrane), which confirms findings that at 37°C after 15 to 20 minutes, EGFR already internalizes[101]. Similar to the above interpretation we can assign A6 and C7 (**Figure 4.3.2.11** and **Figure 4.3.2.12**, $z = 11.0 \mu\text{m}$) to the side membrane. A7, A8 and C8 (**Figure 4.3.2.11** and **Figure 4.3.2.12**, $z = 13.2 \mu\text{m}$) to the dorsal membrane, and A9, A10, and A11 (**Figure 4.3.2.11** and **Figure 4.3.2.12**, $z = 14.3 \mu\text{m}$) to be outside and close to the dorsal membrane (bound to extracellular EGFR). This analysis of 25 PL spots in only three cells can merely provide a broad picture of the different possible localizations of TbNP-AB in and on the cells (64% colocalized with the plasma membrane, 20% on the extracellular side of the membrane, 12% internalized inside the cells, and 4% in the medium outside the cells). However, it suggests that TbNP-AB conjugates are capable of specifically recognizing EGFR without significantly hindering its internalization. Indeed, incubation of A431 cell lines with TbNP-AB (200AB/TbNP) for 5 hours revealed clearly different staining patterns (**Figure 4.3.2.13** and **Figure 4.3.2.14**) with PL signals originating from inside the cells (beyond the membranes and around the nuclei), which is another good evidence that the binding of TbNP-AB conjugates to the transmembrane EGFR leads to endocytosis and internalization of the entire EGFR-TbNP-AB complexes. While our results are only a proof-of-concept and did not aim at the investigation of intracellular signalling, the

results demonstrate that TbNP-AB conjugates may become useful for intracellular live cell bioanalysis. Deeper investigation with many more cells, higher spatial resolution (confocal or super resolution), and at different TbNP-AB incubation times (kinetic study) would be necessary to fully understand the dynamic cellular uptake behaviour of EGFR-attached TbNP-AB.

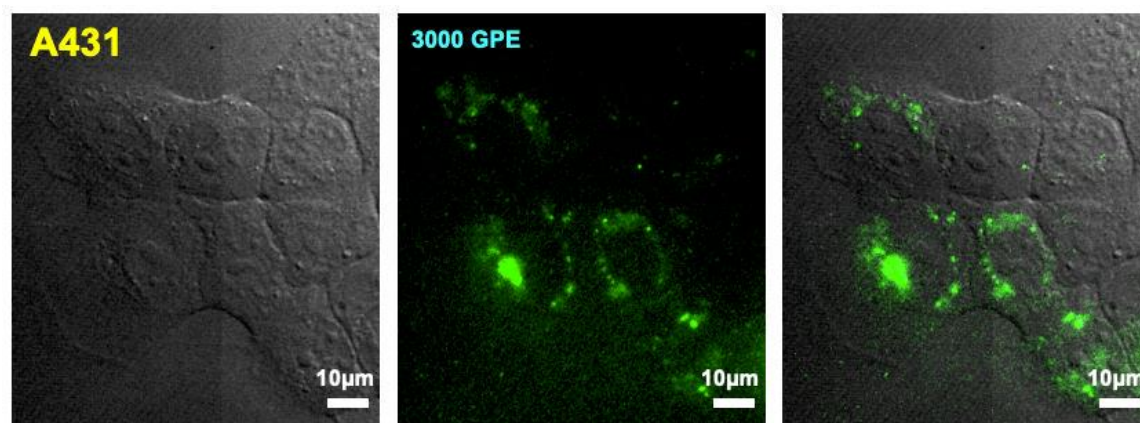


Figure 4.3.2.13: Time-gated PL imaging of EGFR on and in A431 cells that were incubated for 5 hours with 2 nM of 200AB/TbNP. The representative images show DIC transmission (left), time-gated PL (center), and their overlay (right). PL of TbNPs is shown in green. GPE: Gates per exposure.

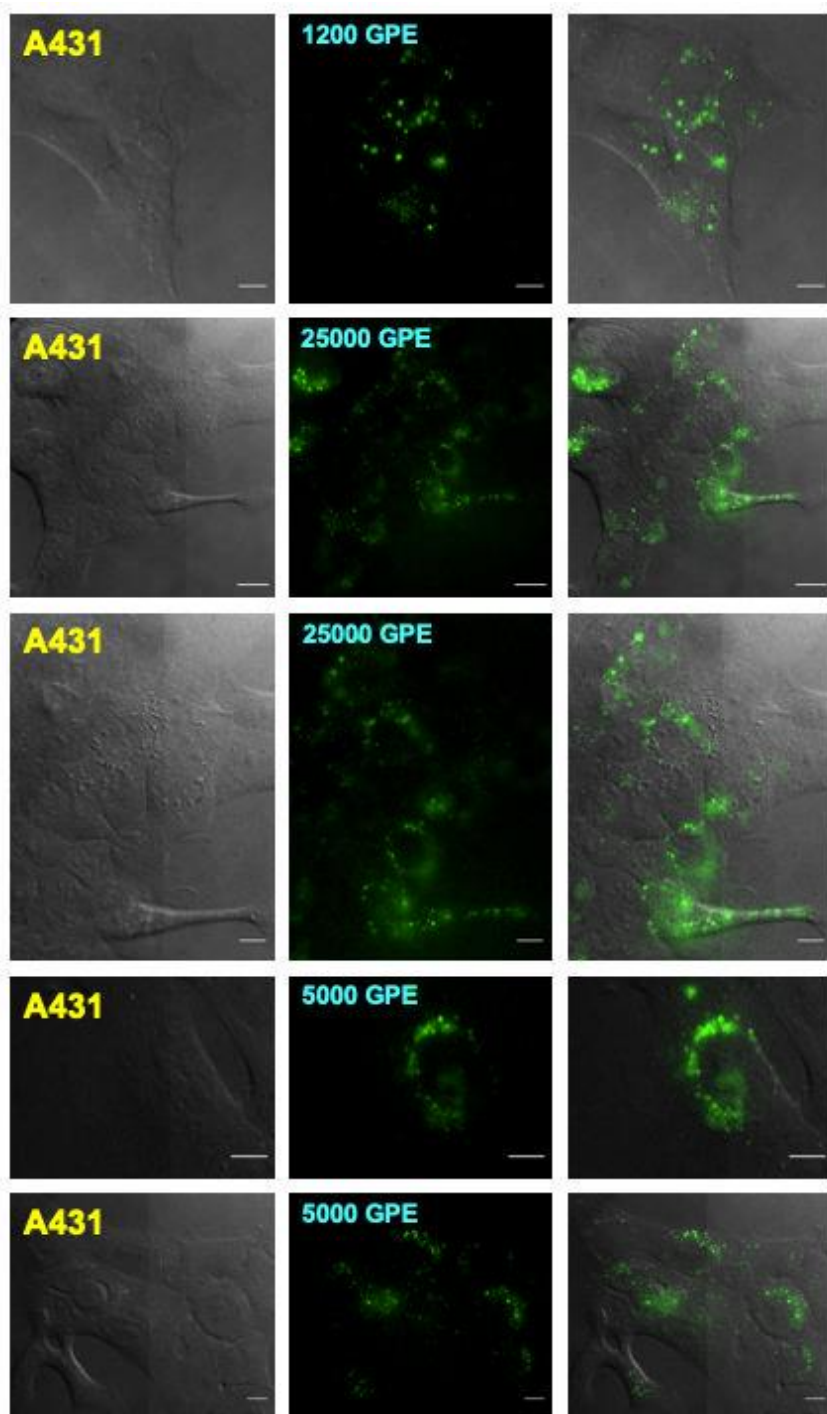


Figure 4.3.2.14: Time-gated PL imaging of EGFR on and in A431 cells that were incubated for 5 hours with 2 nM of 200AB/TbNP. The images show DIC transmission (left), time-gated PL (center), and their overlay (right). PL of TbNPs is shown in green. GPE: Gates per exposure. Scale bar 10 μ m all pictures, except 2nd picture with GPE 25000 that has a scale bar of 20 μ m.

4.4 Conclusion

Lanthanide-doped NPs combine photophysical advantages, such as high brightness, high photostability, line-like spectra, long PL lifetimes, and biocompatibility, with large surfaces for the attachment of various biomolecules. One of the most important prerequisites for implementing such NPs into actual bioanalytical applications is a straightforward design of functional NP-bioconjugates. In our present study, we developed a new type of ligand that can be used for both photosensitization of Tb surface ions and bioconjugation. The ligands were covalently bound to biomolecules, which then attached by simple mixing to the surface of TbNPs via ligand-Tb³⁺ coordination. This simultaneous photosensitization and bioconjugation approach resulted in extremely bright and stable TbNP bioconjugates, which we investigated on a bioimaging application. Time-gated PL microscopy was performed to demonstrate the application of TbNP-antibody conjugates for ligand-receptor binding on cell membranes and a possible implementation into the investigation of transmembrane receptor trafficking. Different cell lines with strong, weak, and no expression of EGFR as well as EGFR-passivated cells were incubated with Matuzumab-functionalized TbNPs and the antibody-TbNP labeling ratio was optimized for specific recognition of extracellular EGFR. TbNP PL images revealed the formation of EGFR clusters and time-dependent internalization of TbNP-Matuzumab-EGFR complexes that started after only 30 minutes of incubation and demonstrated the capability of TbNP-antibody conjugates to be specifically endocytosed by A431 cells. This representative application studied on live cell imaging of ligand-receptor binding and endocytosis demonstrate that surface-photosensitized lanthanide-doped NPs can be efficiently bioconjugated and used in actual biological applications. This important result is of paramount importance for implementing bright and stable lanthanide-NPs as standard PL probes into diverse clinical and bioanalytical research studies.

5. Summary and Outlook

5.1 Summary

This thesis presents the biofunctionalization and detection in-situ of ligand-receptor binding on cells realized by optimized preparation of TbNP-antibody (Matuzumab) conjugates that could specifically bind to transmembrane EGFR. High specificity and sensitivity were demonstrated by time-gated imaging of EGFR on both overexpressing (A431) and weakly (HeLa and COS-7) expressing cell lines. This immunostaining approach serves as a demonstrator for cell membrane biomarker recognition. Time-gated PL microscopy was performed to demonstrate the application of TbNP-antibody conjugates for ligand-receptor binding on cell membranes and a possible implementation into the investigation of transmembrane receptor trafficking. TbNP PL images revealed the formation of EGFR clusters and time-dependent internalization of TbNP-Matuzumab-EGFR complexes that started after only 30 minutes of incubation and demonstrated the capability of TbNP-antibody conjugates to be specifically endocytosed by A431 cells. This representative application studied on live cell imaging of ligand-receptor binding and endocytosis demonstrate that surface-photosensitized lanthanide-doped NPs can be efficiently bioconjugated and used in actual biological applications. This important result is of paramount importance for implementing bright and stable lanthanide-NPs as standard PL probes into diverse clinical and bioanalytical research studies.

From the DLS and ZP measurements, we were able to observe the stability of TbNPs over a period of two months in diH₂O. We were surprised and disappointed to witness that at 10mM Tris/HCl, pH 7.0; 10mM Tris/HCl, 1mM NaF pH 7.0 buffers the size of the NPs was significantly bigger from the size in diH₂O. The influence of pH on the size of TbNPs in diH₂O is not significant, but the smaller size is obtained at pH 6.0 and pH 7.0. From the sonication effect, we learnt that it has some influence on size homogeneity, but not for a long time. What is worth to mention is that TbNPs in 10mM HEPES pH 7.0 had significantly smaller sizes than TbNPs in 10mM Tris/HCl, pH 7.0 or 10mM Tris/HCl, 1mM NaF pH 7.0, that is why we chose to proceed further with the cell

experiments by using HEPES as a buffer instead of Tris/Cl. From these experiments, we learnt more than we knew about our TbNPs and their performance in different buffers and pHs, but certainly more experiments need to be performed in the future.

The TbNPs, L₂* maleimide ligand and L₁* isothiocyanate ligand were provided from our collaborators in Strasbourg (SynPA team) who synthesized and characterized the acid-based ligands hydroxyisophthalates and ultra-bright nanoparticles based on lanthanide ions[13]. The hydroxyisophthalates ligands must have a function that effectively photosensitizes NPs, and possess a spacer connected to an active function. The active function will have the role of reacting with a biological vector (in our case antibody), in order to make the NPs target-specific. The covering of the NPs by chromophore ligands allows, thanks to the antenna effect, to reach brightness's of the order of $10^6 \text{ M}^{-1}\text{cm}^{-1}$ for La_{0.9}Tb_{0.1}F₃ nanoparticles.

5.2 Outlook

There are several ideas that I would like to address for future experiments by using L₂*ligand-TbNPs. One is the comparison between Matuzumab antibody and Cetuximab antibody that is already in clinical use. I would like to perform the same experiment, EGFR recognition on the cell surface[102]. With this experiment in mind, I would like to observe the antibody behavior, if steric hindrance between antibodies is a factor for cluster formation.

Second is to use heavy chain antibodies (antibody with a single chain antigen binding domain, composed of heavy chain only HCAb) instead of conventional monoclonal antibodies for targeting EGFR in tumors. The advantages of using HCAb are several: small size ($\sim 15\text{kDa}$), the clearance from the blood is faster; the denaturation process is reversible and easy to produce in bacteria and eukaryotic cells due to a less complex structure[87].

In order to track signal paths protein engineering can be used useful, for instance transfecting the cell with green fluorescent protein (GFP) on the intracellular part, observe the signal, and cell dynamics. As well, I would like to investigate FRET at these

molecular levels by introducing two fluorophores, one in the extracellular part and the other one in the intracellular part of the receptor.

Another possibility could be to use confocal microscopy coupled with an excitation laser in UV instead of using wide-field microscopy. The advantage of using laser-scanning confocal microscopy would be thin optical sections out of thick specimens, it can view specimens in planes running parallel to the line of sight, it images deep into light scattering samples and produces impressive 3-dimensional views at very high resolution.

Another alternative could be to use the TbNPs as pH sensors, by changing their pH in solution and after cell incubation to observe at which compartment of cell the compound is located.

References

- [1] P. Boisseau et B. Loubaton, « Nanomedicine, nanotechnology in medicine », *Comptes Rendus Physique*, vol. 12, n° 7, p. 620-636, sept. 2011, doi: 10.1016/j.crhy.2011.06.001.
- [2] R. Shandilya, A. Bhargava, N. Bunkar, R. Tiwari, I. Y. Goryacheva, et P. K. Mishra, « Nanobiosensors: Point-of-care approaches for cancer diagnostics », *Biosensors and Bioelectronics*, vol. 130, p. 147-165, avr. 2019, doi: 10.1016/j.bios.2019.01.034.
- [3] S. Bhuckory, O. Lefebvre, X. Qiu, K. D. Wegner, et N. Hildebrandt, « Evaluating quantum dot performance in homogeneous FRET immunoassays for prostate specific antigen », *Sensors (Switzerland)*, vol. 16, n° 2, 2016, doi: 10.3390/s16020197.
- [4] X. Qiu, J. Guo, J. Xu, et N. Hildebrandt, « Three-Dimensional FRET Multiplexing for DNA Quantification with Attomolar Detection Limits », 2018, doi: 10.1021/acs.jpcclett.8b01944.
- [5] X. Qiu, K. D. Wegner, Y.-T. Wu, P. M. P. van Bergen en Henegouwen, T. L. Jennings, et N. Hildebrandt, « Nanobodies and Antibodies for Duplexed EGFR/HER2 Immunoassays Using Terbium-to-Quantum Dot FRET », *Chemistry of Materials*, vol. 28, n° 22, p. 8256-8267, nov. 2016, doi: 10.1021/acs.chemmater.6b03198.
- [6] J. Liu *et al.*, « Biomarkers predicting resistance to epidermal growth factor receptor-targeted therapy in metastatic colorectal cancer with wild-type KRAS », *OTT*, p. 557, janv. 2016, doi: 10.2147/OTT.S86966.
- [7] F. Agostoni *et al.*, « EGFR-directed monoclonal antibodies in combination with chemotherapy for treatment of non-small-cell lung cancer: an updated review of clinical trials and new perspectives in biomarkers analysis », *Cancer Treatment Reviews*, vol. 72, p. 15-27, janv. 2019, doi: 10.1016/j.ctrv.2018.08.002.
- [8] H. S. Afsari *et al.*, « Time-gated FRET nanoassemblies for rapid and sensitive intra- and extracellular fluorescence imaging », *Science Advances*, vol. 2, n° 6, p. e1600265, juin 2016, doi: 10.1126/sciadv.1600265.
- [9] S. P. Kennedy, J. F. Hastings, J. Z. R. Han, et D. R. Croucher, « The Under-Appreciated Promiscuity of the Epidermal Growth Factor Receptor Family », *Front Cell Dev Biol*, vol. 4, août 2016, doi: 10.3389/fcell.2016.00088.
- [10] G. Carpenter et S. Cohen, « 125I-labeled human epidermal growth factor. Binding, internalization, and degradation in human fibroblasts. », *The Journal of Cell Biology*, vol. 71, n° 1, p. 159-171, oct. 1976, doi: 10.1083/jcb.71.1.159.
- [11] A. Sorkin et L. K. Goh, « Endocytosis and intracellular trafficking of ErbBs », *Experimental Cell Research*, vol. 315, n° 4, p. 683-696, févr. 2009, doi: 10.1016/j.yexcr.2008.07.029.
- [12] J. G. Bünzli, « On the design of highly luminescent lanthanide complexes », *Coordination Chemistry Reviews*, vol. 293-294, p. 19-47, 2015, doi: 10.1016/j.ccr.2014.10.013.
- [13] J. Goetz, A. Nonat, A. Diallo, M. Sy, et I. Sera, « Ultrabright Lanthanide Nanoparticles », p. 526-534, 2016, doi: 10.1002/cplu.201600007.

- [14] M. Cardoso Dos Santos, J. Goetz, H. Bartenlian, K.-L. Wong, L. J. Charbonnière, et N. Hildebrandt, « Autofluorescence-Free Live-Cell Imaging Using Terbium Nanoparticles », *Bioconjugate Chemistry*, vol. 29, n° 4, p. 1327-1334, avr. 2018, doi: 10.1021/acs.bioconjchem.8b00069.
- [15] A. S. Collot Mayeul; Ashokkumar, Pichandi; Anton, Halina; Boutant, Emmanuel; Faklaris, Orestis; Galli, Thierry; Mély, Yves; Danglot, Lydia; Klymchenko, *MemBright: A Family of Fluorescent Membrane Probes for Advanced Cellular Imaging and Neuroscience*. 2019.
- [16] « Biomarkers and risk assessment: concepts and principles (EHC 155, 1993) ». <http://www.inchem.org/documents/ehc/ehc/ehc155.htm#SectionNumber:1.1> (consulté le janv. 06, 2020).
- [17] K. Strimbu et J. A. Tavel, « What are biomarkers? », *Current Opinion in HIV and AIDS*, vol. 5, n° 6, p. 463-466, nov. 2010, doi: 10.1097/COH.0b013e32833ed177.
- [18] « Biomarkers and surrogate endpoints: Preferred definitions and conceptual framework », *Clinical Pharmacology & Therapeutics*, vol. 69, n° 3, p. 89-95, mars 2001, doi: 10.1067/mcp.2001.113989.
- [19] « Personalized Medicine Coalition - Advocates for precision medicine : Examples ». <http://www.personalizedmedicinecoalition.org/Education/Examples> (consulté le janv. 06, 2020).
- [20] R. Mayeux, « Biomarkers: Potential Uses and Limitations », vol. 1, n° 2, p. 7, 2004.
- [21] J. Wang, X. Yu, S. V. Boriskina, et B. M. Reinhard, « Quantification of Differential ErbB1 and ErbB2 Cell Surface Expression and Spatial Nanoclustering through Plasmon Coupling », *Nano Lett.*, vol. 12, n° 6, p. 3231-3237, juin 2012, doi: 10.1021/nl3012227.
- [22] S. Sebastian, J. Settleman, S. J. Reshkin, A. Azzariti, A. Bellizzi, et A. Paradiso, « The complexity of targeting EGFR signalling in cancer: From expression to turnover », *Biochimica et Biophysica Acta (BBA) - Reviews on Cancer*, vol. 1766, n° 1, p. 120-139, août 2006, doi: 10.1016/j.bbcan.2006.06.001.
- [23] « Antibody Basics | Sigma-Aldrich ». <https://www.sigmaaldrich.com/technical-documents/articles/biology/antibody-basics.html> (consulté le janv. 06, 2020).
- [24] A. Rajpal, P. Strop, Y. A. Yeung, J. Chaparro-Riggers, et J. Pons, « Introduction: Antibody Structure and Function », in *Therapeutic Fc-Fusion Proteins*, John Wiley & Sons, Ltd, 2013, p. 1-44.
- [25] « Therapeutic IgG-Like Bispecific Antibodies: Modular Versatility and Manufacturing Challenges, Part 1 », *BioProcess International*, déc. 13, 2017. <https://bioprocessintl.com/manufacturing/emerging-therapeutics-manufacturing/therapeutic-igg-like-bispecific-antibodies-modular-versatility-and-manufacturing-challenges-part-1/> (consulté le janv. 06, 2020).
- [26] C. Kollmannsberger *et al.*, « A phase I study of the humanized monoclonal anti-epidermal growth factor receptor (EGFR) antibody EMD 72000 (matuzumab) in combination with paclitaxel in patients with EGFR-positive advanced non-small-cell lung cancer (NSCLC) », *Annals of Oncology*, vol. 17, n° 6, p. 1007-1013, juin 2006, doi: 10.1093/annonc/mdl042.
- [27] K. Kuester, A. Kovar, C. Lüpfer, B. Brockhaus, et C. Kloft, « Population pharmacokinetic data analysis of three phase I studies of matuzumab, a humanised anti-EGFR monoclonal antibody in clinical cancer development », *Br J Cancer*, vol. 98, n° 5, p. 900-906, mars 2008, doi: 10.1038/sj.bjc.6604265.

- [28] « DJ Merck KGaA arrête le développement du matuzumab - Börse (18/02/08) ». https://web.archive.org/web/20110719065442/http://www.newsvz.de/details_Borse,DJ-Merck-KGaA-stellt-Entwicklung-von-Matuzumab-ein,329480.html (consulté le janv. 09, 2020).
- [29] « S. P. Sinha (ed.), Systematics and the Properties of the Lanthanides, 213-254. » .
- [30] « statistic_id277268_rare-earth-reserves-worldwide-by-country-2018.pdf » .
- [31] C. B. Jørgensen, « The inner mechanism of rare earths elucidated by photoelectron spectra », in *Rare Earths*, vol. 13, Berlin, Heidelberg: Springer Berlin Heidelberg, 1973, p. 199-253.
- [32] L. Armelao *et al.*, « Design of luminescent lanthanide complexes: From molecules to highly efficient photo-emitting materials », *Coordination Chemistry Reviews*, vol. 254, n° 5-6, p. 487-505, mars 2010, doi: 10.1016/j.ccr.2009.07.025.
- [33] J.-C. G. Bünzli et S. V. Eliseeva, « Basics of Lanthanide Photophysics », in *Lanthanide Luminescence*, vol. 7, P. Hänninen et H. Härmä, Éd. Berlin, Heidelberg: Springer Berlin Heidelberg, 2010, p. 1-45.
- [34] J.-C. G. Bünzli et C. Piguet, « Taking advantage of luminescent lanthanide ions », *Chemical Society Reviews*, vol. 34, n° 12, p. 1048, 2005, doi: 10.1039/b406082m.
- [35] S. Han, R. Deng, X. Xie, et X. Liu, « Enhancing Luminescence in Lanthanide-Doped Upconversion Nanoparticles », *Angew. Chem. Int. Ed.*, vol. 53, n° 44, p. 11702-11715, oct. 2014, doi: 10.1002/anie.201403408.
- [36] P. Hänninen, H. Härmä, et T. Ala-Kleme, Éd., *Lanthanide luminescence: photophysical, analytical and biological aspects*. Berlin ; New York: Springer, 2011.
- [37] E. G. Moore, A. P. S. Samuel, et K. N. Raymond, « From Antenna to Assay: Lessons Learned in Lanthanide Luminescence », *Acc. Chem. Res.*, vol. 42, n° 4, p. 542-552, avr. 2009, doi: 10.1021/ar800211j.
- [38] R. Reisfeld, « Spectra and energy transfer of rare earths in inorganic glasses », in *Rare Earths*, vol. 13, Berlin, Heidelberg: Springer Berlin Heidelberg, 1973, p. 53-98.
- [39] M. Sy, A. Nonat, N. Hildebrandt, et L. J. Charbonnière, « Lanthanide-based luminescence biolabelling », *Chemical Communications*, vol. 52, n° 29, p. 5080-5095, 2016, doi: 10.1039/C6CC00922K.
- [40] J.-C. G. Bünzli, « Review: Lanthanide coordination chemistry: from old concepts to coordination polymers », *Journal of Coordination Chemistry*, vol. 67, n° 23-24, p. 3706-3733, déc. 2014, doi: 10.1080/00958972.2014.957201.
- [41] J. R. Lakowicz, *Principles of Fluorescence Spectroscopy Principles of Fluorescence Spectroscopy*. 2006.
- [42] M. C. Heffern, L. M. Matosziuk, et T. J. Meade, « Lanthanide Probes for Bioresponsive Imaging », *Chem. Rev.*, vol. 114, n° 8, p. 4496-4539, avr. 2014, doi: 10.1021/cr400477t.
- [43] « Thèse finale alles Cyrille Charpentier (2).pdf » .
- [44] M. Bredol, U. Kynast, et C. Ronda, « Designing Luminescent Materials », *Advanced Materials*, vol. 3, n° 7-8, p. 361-367, 1991, doi: 10.1002/adma.19910030707.
- [45] S. Petoud *et al.*, « Brilliant Sm, Eu, Tb, and Dy Chiral Lanthanide Complexes with Strong Circularly Polarized Luminescence », *J. Am. Chem. Soc.*, vol. 129, n° 1, p. 77-83, janv. 2007, doi: 10.1021/ja064902x.

- [46] M. Cardoso Dos Santos *et al.*, « Lanthanide-Complex-Loaded Polymer Nanoparticles for Background-Free Single-Particle and Live-Cell Imaging », *Chem. Mater.*, vol. 31, n° 11, p. 4034-4041, juin 2019, doi: 10.1021/acs.chemmater.9b00576.
- [47] L. J. Charbonnière, N. Hildebrandt, R. F. Ziessel, et H.-G. Löhmannsröben, « Lanthanides to Quantum Dots Resonance Energy Transfer in Time-Resolved Fluoro-Immunoassays and Luminescence Microscopy », *Journal of the American Chemical Society*, vol. 128, n° 39, p. 12800-12809, oct. 2006, doi: 10.1021/ja062693a.
- [48] J.-C. G. Bünzli, S. Comby, A.-S. Chauvin, et C. D. B. Vandevyver, « New Opportunities for Lanthanide Luminescence », *Journal of Rare Earths*, vol. 25, n° 3, p. 257-274, juin 2007, doi: 10.1016/S1002-0721(07)60420-7.
- [49] J.-C. G. Bünzli et S. V. Eliseeva, « Intriguing aspects of lanthanide luminescence », *Chem. Sci.*, vol. 4, n° 5, p. 1939, 2013, doi: 10.1039/c3sc22126a.
- [50] J. M. Zwier et N. Hildebrandt, « Time-Gated FRET Detection for Multiplexed Biosensing », in *Reviews in Fluorescence 2016*, C. D. Geddes, Éd. Cham: Springer International Publishing, 2017, p. 17-43.
- [51] S. Bhuckory, O. Lefebvre, X. Qiu, K. D. Wegner, et N. Hildebrandt, « Evaluating quantum dot performance in homogeneous FRET immunoassays for prostate specific antigen », *Sensors (Switzerland)*, vol. 16, n° 2, 2016, doi: 10.3390/s16020197.
- [52] Z. Jin, D. Geißler, X. Qiu, K. D. Wegner, et N. Hildebrandt, « A Rapid, Amplification-Free, and Sensitive Diagnostic Assay for Single-Step Multiplexed Fluorescence Detection of MicroRNA », *Angew. Chem. Int. Ed.*, vol. 54, n° 34, p. 10024-10029, août 2015, doi: 10.1002/anie.201504887.
- [53] B. Chen *et al.*, « Magnetic-fluorescent nanohybrids of carbon nanotubes coated with Eu, Gd Co-doped LaF₃ as a multimodal imaging probe », *Journal of Colloid and Interface Science*, vol. 367, n° 1, p. 61-66, févr. 2012, doi: 10.1016/j.jcis.2011.08.084.
- [54] C.-T. Yang *et al.*, « PET-MR and SPECT-MR multimodality probes: Development and challenges », *Theranostics*, vol. 8, n° 22, p. 6210-6232, 2018, doi: 10.7150/thno.26610.
- [55] Z. Cheng *et al.*, « YVO₄:Eu³⁺ functionalized porous silica submicrospheres as delivery carriers of doxorubicin », *Dalton Trans.*, vol. 41, n° 5, p. 1481-1489, 2012, doi: 10.1039/C1DT11399B.
- [56] B. Valeur, « Molecular Fluorescence Principles and Applications », *Molecular Fluorescence*, p. 399, 2001.
- [57] E. J. Soini, L. J. Pelliniemi, I. A. Hemmilä, V. M. Mukkala, J. J. Kankare, et K. Fröjdman, « Lanthanide chelates as new fluorochrome labels for cytochemistry », *J. Histochem. Cytochem.*, vol. 36, n° 11, p. 1449-1451, nov. 1988, doi: 10.1177/36.11.3049792.
- [58] S. Lindén *et al.*, « Terbium-based time-gated Förster resonance energy transfer imaging for evaluating protein–protein interactions on cell membranes », *Dalton Transactions*, vol. 44, n° 11, p. 4994-5003, 2015, doi: 10.1039/C4DT02884H.
- [59] H. J. Tanke, « Imaging of Lanthanide Luminescence by Time-Resolved Microscopy », in *Lanthanide Luminescence*, vol. 7, P. Hänninen et H. Härmä, Éd. Berlin, Heidelberg: Springer Berlin Heidelberg, 2010, p. 313-328.

- [60] L. Sevéus, M. Väisälä, I. Hemmilä, H. Kojola, G. M. Roomans, et E. Soini, « Use of fluorescent europium chelates as labels in microscopy allows glutaraldehyde fixation and permanent mounting and leads to reduced autofluorescence and good long-term stability: FLUORESCENT EUROPIUM CHELATES IN MICROSCOPY », *Microsc. Res. Tech.*, vol. 28, n° 2, p. 149-154, juin 1994, doi: 10.1002/jemt.1070280206.
- [61] Y. HIRAOKA, J. W. Sedat, et D. A. Agard, « for Quantitative Optical Microscopy of Biological Structures », vol. 238, p. 7.
- [62] D. H. Ortgies *et al.*, « Lifetime-Encoded Infrared-Emitting Nanoparticles for in Vivo Multiplexed Imaging », *ACS Nano*, vol. 12, n° 5, p. 4362-4368, mai 2018, doi: 10.1021/acsnano.7b09189.
- [63] S. Cohen, « The stimulation of epidermal proliferation by a specific protein (EGF) », *Developmental Biology*, vol. 12, n° 3, p. 394-407, 1965, doi: [https://doi.org/10.1016/0012-1606\(65\)90005-9](https://doi.org/10.1016/0012-1606(65)90005-9).
- [64] R. L.-M. And et S. Cohen, « Effects of the Extract of the Mouse Submaxillary Salivary Glands on the Sympathetic System of Mammals* », *Annals of the New York Academy of Sciences*, vol. 85, n° 1, p. 324-341, 1960, doi: 10.1111/j.1749-6632.1960.tb49963.x.
- [65] S. Cohen et G. Carpenter, « Human epidermal growth factor: isolation and chemical and biological properties », *PNAS*, vol. 72, n° 4, p. 1317-1321, avr. 1975, doi: 10.1073/pnas.72.4.1317.
- [66] S. Cohen, G. Carpenter, et L. King, « Epidermal growth factor-receptor-protein kinase interactions. Co-purification of receptor and epidermal growth factor-enhanced phosphorylation activity. », *J. Biol. Chem.*, vol. 255, n° 10, p. 4834-4842, mai 1980.
- [67] C. R. King, M. H. Kraus, et S. A. Aaronson, « Amplification of a novel v-erbB-related gene in a human mammary carcinoma », *Science*, vol. 229, n° 4717, p. 974-976, sept. 1985, doi: 10.1126/science.2992089.
- [68] M. H. Kraus, W. Issing, T. Miki, N. C. Popescu, et S. A. Aaronson, « Isolation and characterization of ERBB3, a third member of the ERBB/epidermal growth factor receptor family: evidence for overexpression in a subset of human mammary tumors », *PNAS*, vol. 86, n° 23, p. 9193-9197, déc. 1989, doi: 10.1073/pnas.86.23.9193.
- [69] G. D. Plowman *et al.*, « Ligand-specific activation of HER4/p180erbB4, a fourth member of the epidermal growth factor receptor family. », *PNAS*, vol. 90, n° 5, p. 1746-1750, mars 1993, doi: 10.1073/pnas.90.5.1746.
- [70] M. M. Moasser, « The oncogene HER2: its signaling and transforming functions and its role in human cancer pathogenesis », *Oncogene*, vol. 26, n° 45, p. 6469-6487, oct. 2007, doi: 10.1038/sj.onc.1210477.
- [71] U. Vanhoefer *et al.*, « Phase I Study of the Humanized Antiepidermal Growth Factor Receptor Monoclonal Antibody EMD72000 in Patients With Advanced Solid Tumors That Express the Epidermal Growth Factor Receptor », *JCO*, vol. 22, n° 1, p. 175-184, janv. 2004, doi: 10.1200/JCO.2004.05.114.
- [72] H. Ogiso *et al.*, « Crystal Structure of the Complex of Human Epidermal Growth Factor and Receptor Extracellular Domains », *Cell*, vol. 110, n° 6, p. 775-787, sept. 2002, doi: 10.1016/S0092-8674(02)00963-7.
- [73] B. Linggi et G. Carpenter, « ErbB receptors: new insights on mechanisms and

- biology », *Trends in Cell Biology*, vol. 16, n° 12, p. 649-656, déc. 2006, doi: 10.1016/j.tcb.2006.10.008.
- [74] S. Bhattacharjee, « DLS and zeta potential - What they are and what they are not? », *Journal of Controlled Release*, vol. 235, p. 337-351, 2016, doi: 10.1016/j.jconrel.2016.06.017.
- [75] « Zetasizer Nano ZS | Protein Size, Zeta Potential, Protein Mobility ». <https://www.malvernpanalytical.com/en/products/product-range/zetasizer-range/zetasizer-nano-range/zetasizer-nano-zs> (consulté le janv. 27, 2020).
- [76] M. Kaszuba, J. Corbett, F. M. Watson, et A. Jones, « High-concentration zeta potential measurements using light-scattering techniques », *Proc. R. Soc. A*, vol. 368, n° 1927, p. 4439-4451, sept. 2010, doi: 10.1098/rsta.2010.0175.
- [77] A. L. Poli, T. Batista, C. C. Schmitt, F. Gessner, et M. G. Neumann, « Effect of sonication on the particle size of montmorillonite clays », *Journal of Colloid and Interface Science*, vol. 325, n° 2, p. 386-390, sept. 2008, doi: 10.1016/j.jcis.2008.06.016.
- [78] C. Tan et Q. Wang, « Reversible Terbium Luminescent Polyelectrolyte Hydrogels for Detection of H_2PO_4^- and HSO_4^- in Water », *Inorg. Chem.*, vol. 50, n° 7, p. 2953-2956, avr. 2011, doi: 10.1021/ic102366v.
- [79] N. Zhang, S.-H. Tang, et Y. Liu, « Luminescence behavior of a water soluble calix[4]arene derivative complex with terbium ion(III) in gelation solution », *Spectrochimica Acta Part A: Molecular and Biomolecular Spectroscopy*, vol. 59, n° 5, p. 1107-1112, mars 2003, doi: 10.1016/S1386-1425(02)00288-3.
- [80] B. Machalinski, M. Baskiewicz-Masiuk, et B. Wiszniewska, « The influence of sodium fluoride and sodium hexafluorosilicate on human leukemic cell lines », p. 10, 2003.
- [81] E. Stellwagen, J. D. Prantner, et N. C. Stellwagen, « Do zwitterions contribute to the ionic strength of a solution? », *Anal Biochem*, vol. 373, n° 2, p. 407-409, févr. 2008, doi: 10.1016/j.ab.2007.10.038.
- [82] « DLS – Particle Sizing Systems ». <http://pssnicomp.com/?glossary=dls> (consulté le mars 19, 2019).
- [83] L. Wu et X. Qu, « Cancer biomarker detection: recent achievements and challenges », *Chem. Soc. Rev.*, vol. 44, n° 10, p. 2963-2997, 2015, doi: 10.1039/C4CS00370E.
- [84] P. D. Howes, R. Chandrawati, et M. M. Stevens, « Colloidal nanoparticles as advanced biological sensors », *Science*, vol. 346, n° 6205, oct. 2014, doi: 10.1126/science.1247390.
- [85] A. Escudero *et al.*, « Rare earth based nanostructured materials: synthesis, functionalization, properties and bioimaging and biosensing applications », *Nanophotonics*, vol. 6, n° 5, p. 881-921, août 2017, doi: 10.1515/nanoph-2017-0007.
- [86] S. Li, X. Zhang, Z. Hou, Z. Cheng, P. Ma, et J. Lin, « Enhanced emission of ultra-small-sized $\text{LaF}_3\text{:RE}^{3+}$ (RE = Eu, Tb) nanoparticles through 1,2,4,5-benzenetetracarboxylic acid sensitization », *Nanoscale*, vol. 4, n° 18, p. 5619-5626, août 2012, doi: 10.1039/C2NR31206A.
- [87] I. Altintas, R. J. Kok, et R. M. Schiffelers, « Targeting epidermal growth factor receptor in tumors: From conventional monoclonal antibodies via heavy chain-only antibodies to nanobodies », *European Journal of Pharmaceutical Sciences*, vol. 45, n° 4, p. 399-407, mars 2012, doi: 10.1016/j.ejps.2011.10.015.

- [88] J. Capdevila, E. Elez, T. Macarulla, F. J. Ramos, M. Ruiz-Echarri, et J. Tabernero, « Anti-epidermal growth factor receptor monoclonal antibodies in cancer treatment », *Cancer Treatment Reviews*, vol. 35, n° 4, p. 354-363, juin 2009, doi: 10.1016/j.ctrv.2009.02.001.
- [89] F. Zhang *et al.*, « Quantification of Epidermal Growth Factor Receptor Expression Level and Binding Kinetics on Cell Surfaces by Surface Plasmon Resonance Imaging », *Anal. Chem.*, vol. 87, n° 19, p. 9960-9965, oct. 2015, doi: 10.1021/acs.analchem.5b02572.
- [90] J. Vega, S. Ke, Z. Fan, S. Wallace, C. Charsangavej, et C. Li, « Targeting Doxorubicin to Epidermal Growth Factor Receptors by Site-Specific Conjugation of C225 to Poly(L-Glutamic Acid) Through a Polyethylene Glycol Spacer », p. 7.
- [91] J. D. Orth, E. W. Krueger, S. G. Weller, et M. A. McNiven, « A Novel Endocytic Mechanism of Epidermal Growth Factor Receptor Sequestration and Internalization », *Cancer Res*, vol. 66, n° 7, p. 3603-3610, avr. 2006, doi: 10.1158/0008-5472.CAN-05-2916.
- [92] A. Sorkin, E. Kornilova, L. Teslenko, A. Sorokin, et N. Nikolsky, « Recycling of epidermal growth factor-receptor complexes in A431 cells », *Biochimica et Biophysica Acta (BBA) - Molecular Cell Research*, vol. 1011, n° 1, p. 88-96, mars 1989, doi: 10.1016/0167-4889(89)90083-9.
- [93] M. Collot *et al.*, « MemBright: A Family of Fluorescent Membrane Probes for Advanced Cellular Imaging and Neuroscience », *Cell Chemical Biology*, vol. 26, n° 4, p. 600-614.e7, avr. 2019, doi: 10.1016/j.chembiol.2019.01.009.
- [94] A. D. Edelstein, M. A. Tsuchida, N. Amodaj, H. Pinkard, R. D. Vale, et N. Stuurman, « Advanced methods of microscope control using µManager software », *J Biol Methods*, vol. 1, n° 2, p. 10, nov. 2014, doi: 10.14440/jbm.2014.36.
- [95] N. Normanno *et al.*, « Epidermal growth factor receptor (EGFR) signaling in cancer », *Gene*, vol. 366, n° 1, p. 2-16, janv. 2006, doi: 10.1016/j.gene.2005.10.018.
- [96] O. M. Fischer, S. Hart, A. Gschwind, et A. Ullrich, « EGFR signal transactivation in cancer cells », *Biochem Soc Trans*, vol. 31, n° 6, p. 1203-1208, déc. 2003, doi: 10.1042/bst0311203.
- [97] M. Cardoso Dos Santos et N. Hildebrandt, « Recent developments in lanthanide-to-quantum dot FRET using time-gated fluorescence detection and photon upconversion », *TrAC - Trends in Analytical Chemistry*, vol. 84, p. 60-71, 2016, doi: 10.1016/j.trac.2016.03.005.
- [98] L. Martínez-Jothar *et al.*, « Insights into maleimide-thiol conjugation chemistry: Conditions for efficient surface functionalization of nanoparticles for receptor targeting », *Journal of Controlled Release*, vol. 282, p. 101-109, juill. 2018, doi: 10.1016/j.jconrel.2018.03.002.
- [99] A. Abulrob *et al.*, « Nanoscale Imaging of Epidermal Growth Factor Receptor Clustering: EFFECTS OF INHIBITORS », *J. Biol. Chem.*, vol. 285, n° 5, p. 3145-3156, janv. 2010, doi: 10.1074/jbc.M109.073338.
- [100] R. B. Lichtner et V. Schirmacher, « Cellular distribution and biological activity of epidermal growth factor receptors in A431 cells are influenced by cell-cell contact », *J. Cell. Physiol.*, vol. 144, n° 2, p. 303-312, août 1990, doi: 10.1002/jcp.1041440217.
- [101] A. D. Sorkin, L. V. Teslenko, et N. N. Nikolsky, « The endocytosis of epidermal growth factor in A431 cells: A pH of microenvironment and the dynamics of

- receptor complex dissociation », *Experimental Cell Research*, vol. 175, n° 1, p. 192-205, mars 1988, doi: 10.1016/0014-4827(88)90266-2.
- [102] C. M. Lee et I. F. Tannock, « The distribution of the therapeutic monoclonal antibodies cetuximab and trastuzumab within solid tumors », *BMC Cancer*, vol. 10, n° 1, p. 255, déc. 2010, doi: 10.1186/1471-2407-10-255.
- [103] R. Xu, « Light scattering: A review of particle characterization applications », *Particuology*, vol. 18, p. 11-21, févr. 2015, doi: 10.1016/j.partic.2014.05.002.
- [104] P. M. Carvalho, M. R. Felício, N. C. Santos, S. Gonçalves, et M. M. Domingues, « Application of Light Scattering Techniques to Nanoparticle Characterization and Development », *Front Chem*, vol. 6, p. 237, 2018, doi: 10.3389/fchem.2018.00237.
- [105] S. Honary et F. Zahir, « Effect of Zeta Potential on the Properties of Nano-Drug Delivery Systems - A Review (Part 1) », *Trop. J. Pharm Res*, vol. 12, n° 2, p. 255-264, mai 2013, doi: 10.4314/tjpr.v12i2.19.
- [106] S. Bhattacharjee, « DLS and zeta potential – What they are and what they are not? », *Journal of Controlled Release*, vol. 235, p. 337-351, août 2016, doi: 10.1016/j.jconrel.2016.06.017.

6. Appendix

6.1 Abbreviations

| | |
|--------|--|
| A431 | Human epidermoid carcinoma |
| Ab | Antibody |
| AFP | α -fetoprotein |
| ATP | Adenosine triphosphate |
| APD | Avalanche photodiode detector |
| Cos7 | Monkey fibroblast |
| DELFA | Dissociation Enhanced Lanthanide Fluorescence ImmunoAssay |
| DIC | Differential interference contrast |
| DLS | Dynamic light scattering |
| DNA | Deoxyribonucleic acid |
| EDL | Electric double layer |
| EGFR | Epidermal growth factor receptor |
| FRET | Förster resonance energy transfer |
| GPE | Gates per exposure |
| HCAb | Heavy chain antibody |
| HeLa | Cervical cancer |
| HNSCC | Neck squamous cell carcinomas |
| HS | <i>Helmholtz-Smoluchowski</i> |
| IAM | 2-hydroxyisophalamide |
| ICCD | Intensified charge coupled device |
| ICP-MS | Inductively coupled plasma mass spectrometry |
| Igs | Immunoglobulins |
| J | Total angular momentum |
| KRAS | V-Ki-ras2 Kirsten rat sarcoma viral oncogene homolog |

| | |
|----------|---|
| L | Total orbital angular momentum |
| ℓ | Angular momentum quantum number |
| La | Lanthanum |
| LED | Light-emitting diode |
| Ln | Lanthanides |
| mAb | Monoclonal antibody |
| MAPK | Mitogen-activated protein kinases |
| MB-640 | MemBright-640 |
| miRNA | microRNA |
| m_ℓ | Magnetic quantum number |
| MRI | Magnetic resonance imaging |
| m_s | Spin quantum number |
| n | Quantum number |
| Nd-YAG | Neodymium-doped yttrium aluminum garnet |
| NIH3T3 | Mouse embryonic fibroblast |
| NIR | Near infrared |
| NPs | Nanoparticles |
| PALS | Phase Analysis Light Scattering |
| PDI | Polydispersity index |
| PL | Photoluminescence |
| PLNPs | Persistent luminescence nanoparticles |
| PtdIns | Phosphatidylinositol |
| RI | Refractive index |
| RTK | Receptor tyrosine kinases |
| S | Total spin angular momentum |
| TbNPs | Terbium nanoparticles |
| TEM | Transmission electron microscopy |
| TG | Time-gated |

| | |
|--------|---------------------------------------|
| TKIs | Tyrosine kinase inhibitors |
| TM | Transmembrane domain |
| TR-FIA | Time-resolved fluoroimmunoassay |
| TRLM | Time-resolved luminescence microscopy |
| UCNPs | Upconversion nanoparticles |
| UV | Ultraviolet |
| Vis | Visible |
| Xe | Xenon |
| Z | Atomic number |
| ZP | Zeta potential |

6.2 Principles of Dynamic Light Scattering and Zeta Potential

6.2.1 Principles of Dynamic Light Scattering (DLS)

Plenty of different definitions on which the nanomaterials comply exist. However, taking into account the guidelines released from the European Union (EU) (2011/696/EU) we understood that materials that have at least one size in the range of 1 nm could be used as nanomaterials, or the ones that have a size range approximately from 1-100 nm. Another statement defines nanomaterial as the compound that has more than 50% of particles in the range of 1-100 nm. Dynamic light scattering (DLS) emerged in this context as a nanoparticulate size measurement tool, to try to define at best the size of the materials in research studies. DLS also known as photon correlation spectroscopy (PCS) detects the intensity of the scattered light that comes from the illuminated particles in a colloid. DLS will measure the Brownian motion of the particles and will relate these motions to the size of the particle. The particles in a solution are illuminated with a laser and the intensity fluctuations in the scattered light are measured over the time. Brownian motion is the movement of particles due to the random collision with the molecules of the liquid that surrounds the particle[72, 73]. From the Brownian motion we know that small particles will move faster and large particles will move slower. Therefore, to correlate the size of the particles and their speed due to Brownian motion, taking into account that these particles are solid spherical particles a *Stokes-Einstein* equation is derived[104]:

$$D_t = k_B T / 6\pi\eta R_H \quad (6.2.1.1)$$

where: k_B is Boltzmann constant ($1.38064852 \times 10^{-23} \text{ J/K}$);

T is the temperature (K);

η is absolute viscosity ($\text{kg/m}^2\text{s}$);

R_H is the hydrodynamic radius of the spherical particles (nm);

The hydrodynamic radius (R_H) of solid particles can be derived from *Stokes-Einstein* equation that gives us the calculated value of translational diffusion coefficient (D_t).

Careful attention needs to be made when feeding the software with the data of your sample since from the *Stokes-Einstein* equation, DLS depends on several variables including viscosity of the solvent, temperature, refractive index (RI) of the material and size of the particles. This technique is non-invasive, requires minimal sample preparation, it has a user-friendly interface and it needs no pre-experimental calibration, but careful interpretation needs to be made when it comes to report the DLS data.

6.2.2 Principles of Zeta Potential (ZP)

Zeta potential also described as *electrokinetic potential*, measures the potential at the slipping/shear plane of a particle moving under electric field. ZP indicates the potential difference between the electric double layer (EDL) of electrophoretically mobile particles and the layer of dispersant around the particles (aqueous or organic environment) at the slipping plane, **Figure 6.2.2.1** and is usually denoted with the Greek letter zeta (ζ) and is expressed in millivolt (mV) units [74–76]. The electrical double layer will develop around the particle surface, by resulting in an increased concentration of counter ions (ions of opposite charge to that of the particle). EDL is the liquid that surrounds the particle and exists as two parts: an inner region where the ions are strongly attached called *Stern layer* and an outer region (*diffuse*) where the ions are less firmly attached. Inside the *diffuse layer* it exist a notional boundary inside which the ions and particles form a stable entity. Due to gravity, the particle will move and ions within this boundary will move together. This boundary is called the surface of hydrodynamic shear or *slipping plane*. The potential that exist at this boundary is the one that we measure in Malvern Zetasizer® and is known as the zeta potential. The values of zeta potential indicates the potential stability of colloidal system[106].

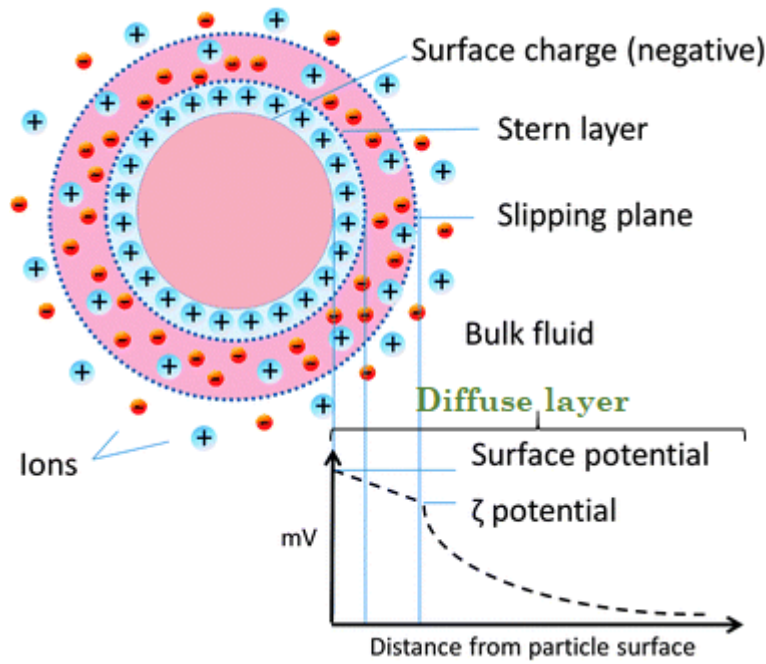


Figure 6.2.2.1: Schematic representation of the electric double layer that surrounds a negatively charged particle in a medium. On top of the particle surface there is a strongly adhered layer (Stern layer) comprising of ions of opposite charge (i.e. in this case positive ions). Beyond Stern layer a diffuse layer develops consisting of negatively and positively charged ions. The ZP is the electrokinetic potential at the slipping plane. Figure and script adapted from references [74, 76].

Upon an electric field is applied across a pair of electrodes, the charged particles in the electrolyte will be attracted towards the electrode of opposite charge (*electrophoresis*). Once the equilibrium reached in the electrolyte, the particles will move with constant velocity. The particle velocity is dependable on viscosity of the medium, voltage gradient, dielectric constant of the medium and zeta potential. Velocity of a particle in an electric field is referred to as *electrophoretic mobility*. ZP is deduced from electrophoretic mobility of charged particles under an applied electric field. Therefore, firstly the calculations to obtain the electrophoretic mobility (μ_e) of the particles should be performed, following the (**Equation 6.2.2.1**):

$$\mu_e = \frac{v}{E} \quad (6.2.2.1)$$

where: V is particle velocity ($\mu\text{m/s}$);
 E is electric field strength (Volt/cm);

Following *Henry's equation* the ZP can be obtained (**Equation 6.2.2.2**):

$$\mu_e = \frac{2 \varepsilon_r \varepsilon_0 \zeta f(Ka)}{3 \eta} \quad (6.2.2.2)$$

where: ε_r is the relative permittivity/dielectric constant;

ε_0 is the permittivity of vacuum;

ζ is the zeta potential;

η is the viscosity at the experimental temperature;

$f(Ka)$ is the Henry's function;

When particles have a size larger than 0.2 μm dispersed in a concentrated aqueous solution ($10^{-2} - 10^{-3}$ M) the Henry's equation is modified to *Helmholtz-Smoluchowski* (HS) equation, where $f(Ka)$ take a value of 1.5. When the particles have sizes (≤ 100 nm) and they are dispersed in low salt concentration (10^{-5} M) the value of $f(Ka)$ is taken as 1.0 and the Henry's equation it modified to *Hückel* equation. Hückel equation is usually not applicable for aqueous solutions and is mainly used in ceramic industry[74–77].

Synthèse en français

« Vous n'échouez jamais tant que vous n'avez pas cessé d'essayer »

Albert Einstein

Des échecs, nous nous relevons et chaque fois nous nous relevons plus fort. L'échec est un sentiment que l'on rencontre souvent dans la recherche scientifique lorsque la première expérience a échoué, la seconde également etc... Cependant, nous ne devrions jamais cesser d'essayer de trouver de nouvelles solutions, de nouvelles voies pour résoudre les problèmes. La détermination est une caractéristique qui devrait toujours accompagner l'être humain dans sa quête de connaissance et cette thèse en est la preuve.

Nous vivons à l'ère des nanosciences et des nanotechnologies, l'échelle nanométrique étant celle à laquelle les molécules et les structures biologiques fonctionnent à l'intérieur des cellules vivantes. En manipulant à ce même niveau moléculaire dans un avenir proche, nous serons en mesure de détecter plus rapidement des maladies, d'améliorer la spécificité de l'administration des médicaments et de proposer une médecine personnalisée. L'une des principales raisons pour lesquelles les nanoparticules sont si attrayantes pour les applications médicales est leur rapport surface/volume qui devient important lorsque leur taille diminue. Cette particularité est mise à profit pour obtenir des interactions chimiques appropriées avec les biomolécules. Sonder l'intérieur du monde biologique infiniment petit est nécessaire pour utiliser des capteurs nano-bio de haute spécificité et sensibilité. Un biocapteur est un dispositif analytique qui comprend une combinaison d'éléments de détection biologique comme un système de détection et un transducteur. Le transducteur, qui dans notre cas sont les nanoparticules fluorescentes, sont utilisés pour convertir le signal biochimique en un signal mesurable et quantifiable, **Figure 1.1** [1].

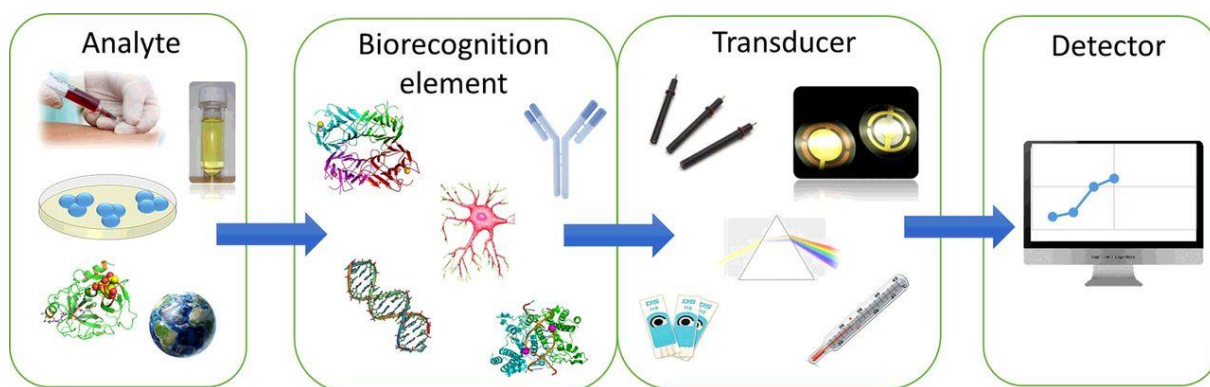


Figure 1.1 : Schéma d'un biocapteur qui se compose de deux éléments : un biorécepteur et un transducteur. (Reproduit de la référence Š. Belický et al., Copyright Essays in Biochemistry 2016)

Les transducteurs peuvent être optiques, thermiques, électrochimiques, piézoélectriques et micromécaniques. Dans ma thèse, j'ai utilisé des transducteurs optiques basés sur la fluorescence. Pour l'imagerie médicale, le rôle ultime des nanocapteurs est de diagnostiquer la maladie le plus tôt possible au niveau d'une seule cellule sans procédure douloureuse invasive et de contrôler l'efficacité de la thérapie. L'une des principales causes de mortalité dans le monde est le cancer, avec 9,6 millions de décès en 2018. C'est pourquoi un diagnostic précoce du cancer est extrêmement important pour augmenter les chances de survie, pour fournir un traitement avec moins d'effets secondaires par rapport au traitement brutal de la chimiothérapie et pour disposer du traitement le plus approprié pour l'éradication finale du cancer [2]. Les biomarqueurs pour le diagnostic du cancer peuvent être trouvés dans le sérum ou les tissus [3-5]. L'émergence d'anticorps monoclonaux ciblant l'EGFR (récepteurs du facteur de croissance épidermique) est une étape importante dans l'histoire du traitement du cancer. L'association de l'immunothérapie et de la chimiothérapie a amélioré la survie globale du patient. Une fois que les voies de signalisation de l'EGFR sont activées, elles favorisent la croissance et la progression de la tumeur, y compris l'angiogenèse, l'invasion, les métastases, la prolifération et l'inhibition de l'apoptose. C'est pourquoi il est d'une importance majeure de cibler et de mieux comprendre ces voies [6, 7].

Cette thèse est axée sur la détection de la surexpression de la protéine EGFR en

utilisant des nanoparticules de Terbium (TbNP) sur une lignée cellulaire humaine modèle (cellules A431) établie à partir d'un carcinome épidermoïde de la peau (épiderme) [8]. L'EGFR est surexprimé dans de nombreuses tumeurs solides et a fait l'objet de nombreuses recherches scientifiques [9].

La raison pour laquelle nous avons choisi la lignée cellulaire A431 comme modèle pour nos recherches est sa surexpression incontrôlée de l'EGFR [8, 9]. L'étude présentée ici a utilisé l'une des approches les plus classiques pour détecter l'EGFR dans le domaine extracellulaire avec un anticorps monoclonal (mAb). L'observation du signal a été réalisée à l'aide d'un microscope en sélection temporelle qui permet une suppression efficace de l'autofluorescence provenant des fluorophores endogènes qui résident dans les cellules et ne recueillent que les photons émetteurs de notre composé, **Figure 1.2**.

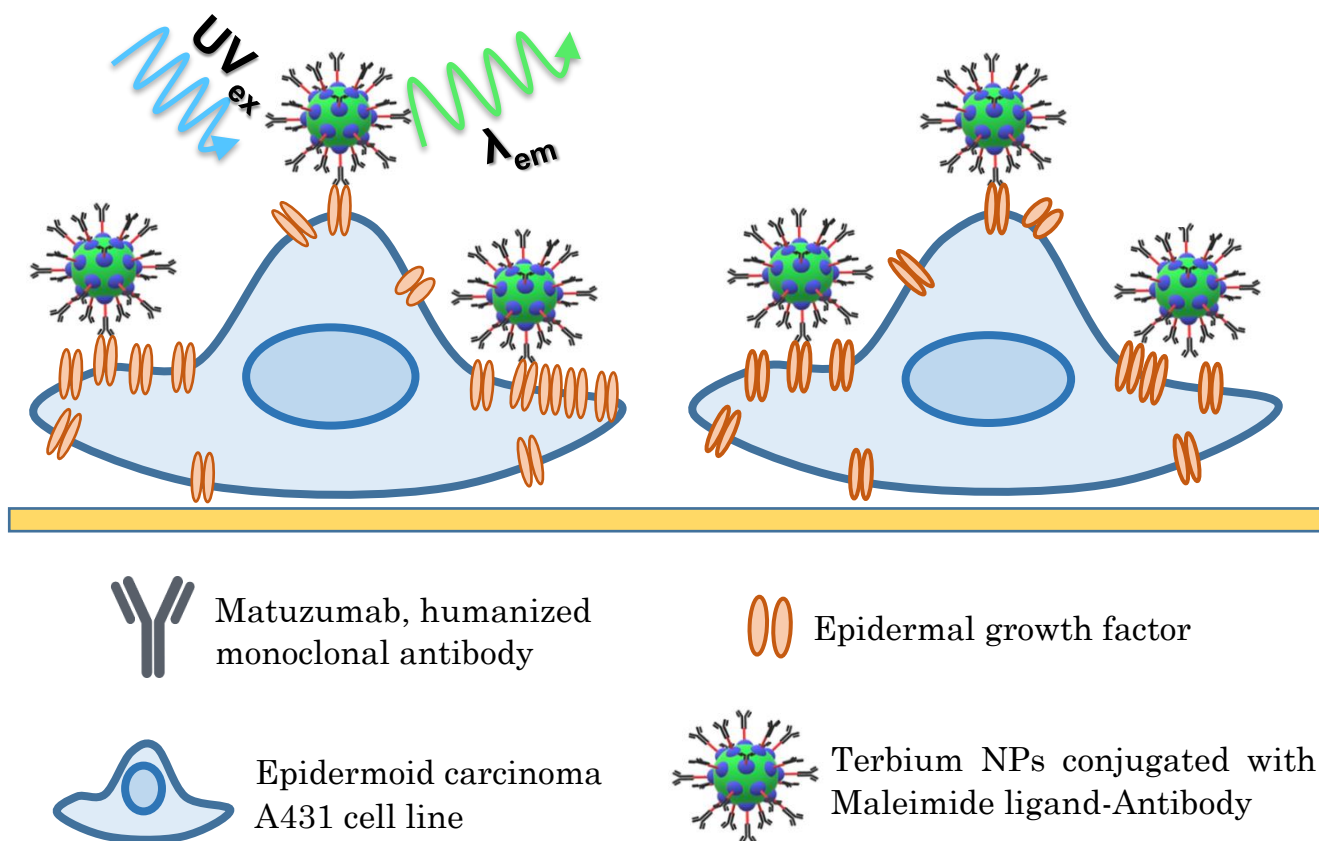


Figure 1.2: Schéma expérimental représentant l'immuno-marquage des épitopes de l'EGFR avec le ligand maléimide TbNPs-L2 fonctionnalisé avec l'anticorps matuzumab sur la membrane cellulaire de la lignée cellulaire A431 du carcinome épidermoïde.*

La détection est effectuée sur la base du signal de luminescence d'un fluorophore, en l'occurrence, des nanoparticules de terbium (TbNP). Le terbium appartient à la famille des lanthanides (Ln), et en raison des transitions f-f intraconfigurationnelles interdites des ions lanthanides centraux (forme commune de Ln^{3+}), les complexes de lanthanides présentent des propriétés photo-physiques distinctes, par rapport aux autres fluorophores, telles que les multiples bandes d'émission étroites caractéristiques, et des durées de vie à l'état excité extrêmement longues, pouvant aller jusqu'à plusieurs millisecondes [12]. Le principal inconvénient des sondes à base de Ln est leur luminosité limitée en raison des sections d'absorption extrêmement faibles des ions Ln. Cet inconvénient ne peut être surmonté qu'en partie par la conception de complexes Ln supramoléculaires avec des ligands d'antenne ou par le dopage de nombreux ions Ln dans les NPs [13].

Pour surmonter cet obstacle, nos collaborateurs à Strasbourg (équipe SynPA) ont synthétisé et caractérisé deux nouveaux ligands d'acide : les (hydroxyisophtalates) et des nanoparticules ultra-lumineuses à base d'ions lanthanides. Les ligands hydroxyisophtalates doivent avoir une fonction qui photosensibilise efficacement les NPs, et posséder un espaceur relié à une fonction active. La fonction active aura pour rôle de réagir avec un vecteur biologique (par exemple un anticorps), afin de rendre les NPs spécifiques. Le recouvrement des NPs par des ligands chromophores permet, grâce à l'effet d'antenne, d'atteindre des brillances de l'ordre de $10^6 \text{ M}^{-1}\text{cm}^{-1}$ pour les nanoparticules $\text{La}_{0,9}\text{Tb}_{0,1}\text{F}_3$.

Au **chapitre 3**, je présente les résultats obtenus lors des tests de caractérisation et de stabilité qui ont été réalisés pour la solution de TbNPs nus par diffusion dynamique de la lumière (DLS) et potentiel zêta (ZP). Nous avons observé l'influence du temps et des différents milieux, puis nous avons étudié l'influence du pH. Nous avons également voulu observer l'effet de la sonication en fonction du temps dans le tampon le plus performant.

Mon objectif principal est la bio-fonctionnalisation et la détection in-situ de la liaison ligand-récepteur sur les cellules réalisées par la préparation optimisée de conjugués TbNP-anticorps (Matuzumab) qui pourraient se lier spécifiquement à l'EGFR

transmembranaire. Une spécificité et une sensibilité élevées a été démontrées par l'imagerie d'une sélection temporelle (`time-gated (TG) Imaging`) sur des lignées cellulaires sur-exprimant EGFR (A431) et l'exprimant faiblement (HeLa et COS-7). Cette approche d'immuno-marquage sert de démonstrateur pour la reconnaissance des biomarqueurs de la membrane cellulaire. Pour démontrer leur spécificité, des expériences de contrôle ont été réalisées avec la saturation en anticorps (pré-incubation) de la membrane cellulaire dans la lignée cellulaire A431 et en utilisant une lignée cellulaire NIH/3T3 dépourvue d'EGFR (**Chapitre 4**).

Ces deux études ont été réalisées en parallèle.

Une caractérisation spectroscopique détaillée des conjugués ligand-Ab a été réalisée en utilisant une spectroscopie d'absorption UV/Vis pour estimer le nombre d'anticorps par ligand. L'imagerie TG par photoluminescence à grand champ (PL) a été réalisée en utilisant un microscope inversé couplé à un laser UV pulsé et une caméra CCD intensifiée pour la détection temporelle [8, 16]. Pour mieux localiser les conjugués TbNP-AB sur l'enveloppe cellulaire, la membrane plasmique a été colorée avec un colorant appelé MEM-Bright Cy5 (un don généreux du Dr Andrey Klymchenko) [15].

Après cette introduction, nous présenterons le contexte théorique des biomarqueurs, de la famille des EGFR, des lanthanides, de la microscopie de fluorescence et des principes de la DLS et du ZP. Les études expérimentales suivront avec une introduction, le matériel et méthodes, les résultats et la discussion, et une conclusion. Un résumé traitant des résultats obtenus à partir des études expérimentales sera discuté et une perspective sur les recherches futures sera présentée. Une bibliographie et une annexe suivront à la fin de la thèse.